

# **Exploring the extreme limits of thermal conduction in solids via steady-state thermoreflectance (SSTR)**

---

A Dissertation Presented to the  
Faculty of the School of Engineering and Applied Science  
University of Virginia

In Partial Fulfillment  
of the Requirements for the Degree of  
Doctor of Philosophy  
Mechanical and Aerospace Engineering

---

Md Shafkat Bin Hoque  
December 2023

## APPROVAL SHEET

The dissertation is submitted in partial fulfillment of the  
requirements for the degree of

Doctor of Philosophy in Mechanical and Aerospace Engineering

---

Md Shafkat Bin Hoque

This dissertation has been read and approved by the Examining Committee:

---

Patrick E. Hopkins, Advisor

---

Keivan Esfarjani, Chair

---

Mona Zebarjadi

---

Ashutosh Giri

---

Prasanna V. Balachandran

Accepted for the School of Engineering and Applied Science:

---

Jennifer L. West, Dean  
School of Engineering and Applied Science

December 2023

## Abstract

The primary objective of this dissertation is to study the extreme limits of thermal conduction in solids via the pump-probe technique steady-state thermoreflectance (SSTR). This recently-developed optical technique operates at a time and length scale previously inaccessible by conventional laser-based thermometry techniques, e.g., time-domain thermoreflectance (TDTR), frequency-domain thermoreflectance (FDTR), and laser flash analysis (LFA). These unique features enable SSTR to circumvent many limitations of the existing laser-based thermal measurement systems. For instance, the thermal penetration depth of SSTR can be significantly higher compared to TDTR and FDTR, while still remaining sensitive to nanoscale resistances and thermal transport in solids with length scales inaccessible by LFA. Additionally, using Fourier's law, SSTR can directly measure the thermal conductivity of any material without prior knowledge of its heat capacity. These capabilities make SSTR an ideal technique for investigating the fundamental transport mechanisms in different materials as well as measuring the thermal properties of challenging geometries. Inspired by this, I use SSTR to study the thermal properties of buried films and substrates, in-plane and cross-plane thermal conductivity of thin film materials, total thermal resistance of multilayered geometries, and high-temperature thermal conductivity of new-types of materials. The material candidates chosen for the projects include high-quality aluminum nitride films, organic-inorganic hybrid metalcone films, copper-tungsten nanomultilayers, high-entropy diborides, and perovskite chalcogenides. Each of the discussed projects fit a geometry consideration that is highly challenging to measure via the more traditionally used thermometry techniques. The measured thermal properties of these systems increase the fundamental understanding of electron and phonon transport mechanisms that is only enabled by the unique length scales and sensitivities of SSTR, which we analyze and discuss in detail in this dissertation.

## Acknowledgements

Writing the acknowledgement section is the toughest part of my dissertation. I am indebted to so many people for their guidance and help, properly acknowledging all of them will make this section longer than the rest of the dissertation. I certainly hope that through our in-person interactions and communications, each of them know how much I appreciate their contributions.

First and foremost, I would like to thank my advisor Dr. Patrick E. Hopkins for his continuous support throughout my PhD. I consider myself extremely lucky for getting the opportunity to work with him. Patrick's kindness, compassion, patience, and enthusiasm about research has made my time at the ExSiTE Lab truly enjoyable.

Next, I would like to express my gratitude to my committee members – Dr. Keivan Esfarjani, Dr. Mona Zebarjadi, Dr. Ashutosh Giri, and Dr. Prasanna V. Balachandran. Without their supervision and guidance, my research would not be where it is today.

Throughout my time at the ExSiTE Lab, I have had the opportunity to work with a passionate, energetic, kind, and fun group of people. I consider it an honor to call them my labmates. I will not try to name all of them out of the possibility that I might miss one of them. Even then, I must acknowledge the contribution of Dr. John T. Gaskins, Dr. John A. Tomko, Dr. Jeffrey L. Braun, Dr. David H. Olson, Dr. Yee Rui Koh, and Dr. Eric R. Hogle for teaching me everything I know. The various fun activities I participated in with former and current labmates at different conferences will always be in my mind: ranging from scuba diving in Hawaii with Kiumars to fishing in Daytona with William, Emma, and Hunter.

I am extremely fortunate to have collaborated with some of the biggest names in the field outside of ExSiTE Lab. In particular, I have to thank Dr. Asif Khan, Dr. Gregory Parsons, Dr. Claudia Cancellieri, Dr. Jian Luo, Dr. Jayakanth Ravichandran, Dr. Jon F. Ihlefeld, and Dr. W. Alan Doolittle for providing us the materials for thermal characterization.

Last but not least, I have to acknowledge the contribution of my parents and brother to my graduate study. They have been a constant source of inspiration throughout my life, I am incredibly lucky to have such a supporting family.

# Contents

<b>Abstract</b>	<b>i</b>
<b>Acknowledgements</b>	<b>i</b>
<b>1 Introduction</b>	<b>1</b>
<b>2 Theory</b>	<b>5</b>
2.1 Energy carriers in non-metallic crystals . . . . .	5
2.1.1 Phonons . . . . .	5
2.1.2 Phonon dispersion . . . . .	6
2.1.3 Phonon heat capacity . . . . .	8
2.1.4 Phonon thermal conductivity . . . . .	9
2.2 Energy carriers in metallic crystals . . . . .	11
2.2.1 Electrons . . . . .	11
2.2.2 Electronic heat capacity . . . . .	12
2.2.3 Electronic thermal conductivity . . . . .	12
2.3 Energy carriers in non-metallic amorphous solids . . . . .	14
2.3.1 Locons, diffusons, and propagons . . . . .	14
2.3.2 Thermal conductivity of non-metallic amorphous solids . . . . .	15
2.4 Theoretical lower limits of thermal conductivity . . . . .	16
<b>3 Experimental measurement techniques</b>	<b>17</b>
3.1 Steady-state thermoreflectance (SSTR) . . . . .	17
3.1.1 Experimental details and signal analysis . . . . .	17
3.1.2 Analytical expression of steady-state temperature rise . . . . .	19
3.1.3 Sensitivity analysis . . . . .	20
3.1.4 Uncertainty analysis . . . . .	22
3.2 Time-domain thermoreflectance (TDTR) . . . . .	23
<b>4 Measuring sub-surface buried substrates and films via SSTR</b>	<b>26</b>
4.1 Motivation . . . . .	26
4.2 Thermal penetration depth of SSTR technique . . . . .	27
4.2.1 Impact of metallic transducer on thermal penetration depth . . . . .	27
4.2.2 Impact of multilayered geometry on thermal penetration depth . . . . .	29
4.3 Measurements of buried substrates . . . . .	32

4.4	Measurements of buried films	35
4.5	Summary	36
<b>5</b>	<b>Investigating thermal transport in thermally conductive ultra-wide bandgap semiconductor films</b>	<b>38</b>
5.1	Motivation	38
5.2	Growth and characterization details	40
5.3	Results and discussion	41
5.4	Summary	51
<b>6</b>	<b>Investigating thermal transport in insulating polymer films</b>	<b>53</b>
6.1	Motivation	53
6.2	Growth details	54
6.3	Results and discussion	55
6.4	Summary	57
<b>7</b>	<b>Measuring thermal resistance of multilayered geometries</b>	<b>58</b>
7.1	Motivation	58
7.2	Growth and characterization details	59
7.3	Results and discussion	62
7.4	Summary	65
<b>8</b>	<b>Extending SSTR measurements to high temperatures</b>	<b>66</b>
8.1	Motivation	66
8.2	Growth and characterization details	67
8.3	Results and discussion	68
8.4	Summary	74
<b>9</b>	<b>Validating heat capacity assumptions of a perovskite chalcogenide</b>	<b>75</b>
9.1	Motivation	75
9.2	Growth and characterization details	76
9.3	Results and discussion	78
9.4	Summary	80
<b>10</b>	<b>Summary and future works</b>	<b>81</b>
<b>A</b>	<b>Published Work</b>	<b>107</b>

# List of Figures

1.1	Characteristic time and length scales associated with the optical thermometry techniques . . . . .	2
2.1	Phonon propagation through a crystal . . . . .	5
2.2	Phonon dispersion curves for (a) monoatomic and (b) diatomic chains . . . . .	7
2.3	Volumetric heat capacity of Si . . . . .	8
2.4	Representative crystal structures where the thermal conductivity is impacted by (a) phonon-phonon scattering, (b) phonon-defect scattering, and (c) phonon-boundary scattering . . . . .	10
2.5	Thermal conductivity of crystalline (a) Si and (b) $\text{Ba}_{1-x}\text{La}_x\text{F}_{2+x}$ as a function of temperature . . . . .	11
2.6	Diffusion of hot electrons in metals . . . . .	11
2.7	Volumetric heat capacity of Pt . . . . .	12
2.8	Thermal conductivity of Pt . . . . .	14
2.9	Thermal conductivity of amorphous $\text{SiO}_2$ . . . . .	15
3.1	A simplified schematic diagram of the SSTR setup. (b) Balanced photodetector response as a function of pump photodetector response for SSTR fitting of Al-coated bulk a- $\text{SiO}_2$ , z-cut quartz, and Si . . . . .	18
3.2	(a) Heat flow directions during SSTR measurements of a thin film on a substrate. (b) Sensitivity calculations for a $3.05 \mu\text{m}$ AlN thin film on sapphire substrate . . . . .	22
3.3	(a) A simplified schematic diagram of the two-color TDTR setup. (b) Ratio of in-phase to out-of-phase signal as a function of pump-probe delay time for TDTR fitting of Al-coated bulk a- $\text{SiO}_2$ , sapphire, and Si. (c) Picosecond acoustic response for a $\sim 80 \text{ nm}$ Al transducer on sapphire . . . . .	24
4.1	(a) Thermal penetration depth as a function of substrate thermal conductivity for a 2-layer system: metal transducer on a substrate. (b) Normalized temperature drop as a function of depth for a substrate thermal conductivity of $1000 \text{ W m}^{-1} \text{ K}^{-1}$ . . . . .	28
4.2	(a and b) Thermal penetration depth as a function of film thickness for a 3-layer system: metal transducer/thin film/substrate. (c and d) Normalized temperature drop as a function of depth for five different thin film thicknesses. (e and f) Temperature profiles of SSTR measurements for a $3 \mu\text{m}$ thin film on a substrate corresponding to an absorbed power of $5 \text{ mW}$ . . . . .	31

4.3	Schematics of the 3-layer samples measured by SSTR: (a) $\sim 130$ nm SiO <sub>2</sub> thin film on Si substrate, (b) $\sim 2.05$ $\mu$ m GaN thin film on n-GaN substrate, and (c) $\sim 2$ $\mu$ m AlN thin film on sapphire substrate . . . . .	33
4.4	(a) Schematic diagram and (b) sensitivity calculation as a function of effective radius for the 4-layer sample: 85 nm Al transducer/2.5 $\mu$ m Si film/1 $\mu$ m SiO <sub>2</sub> layer/Si substrate . . . . .	36
5.1	(a) Schematic of AlN thin film samples: Al transducer/AlN film/sapphire substrate. (b) Reflected probe laser intensity change as a function of pump photodetector voltage for SSTR fitting of bulk Si and 3.05 $\mu$ m AlN film thermal conductivities . . . . .	41
5.2	Calibration of SSTR technique via bulk Si wafer thermal conductivity measurements . . . . .	42
5.3	(a) In-plane thermal conductivity as a function of film thickness for different high thermal conductivity materials. (b) Normalized in-plane thermal conductivity of the films presented in panel a as a function of thickness. (c) The thermal conductivity of natural and isotope enriched adamantane crystals as a function of the Leibfried-Schomann scaling parameter . . . . .	43
5.4	(a) Temperature-dependent in-plane thermal conductivity of the 3.05 $\mu$ m AlN film. (b) Temperature-dependent in-plane and cross-plane thermal conductivities of several high thermal conductivity materials. (c) Temperature dependent in-plane thermal conductivities of the 3.05, 3.75, and 6 $\mu$ m AlN thin films. (d) Thickness-normalized in-plane thermal conductivity of micrometer-thick films of high thermal conductivity materials at $\sim 120$ K . . . . .	46
5.5	(a) Temperature-dependent in-plane and cross-plane thermal conductivities of the 3.05 $\mu$ m AlN thin film. (b) Phonon heat transport mechanisms along the in-plane and cross-plane directions of the 3.05 $\mu$ m film. (c) Thermal conductivity anisotropy ratios as a function of temperature for the 3.05 $\mu$ m AlN film, graphite, black phosphorus, 4.2 $\mu$ m Si on insulator, Si/Ge superlattice, and InN film . . . . .	49
6.1	Structures of the (a) alucone and (b) tincone films . . . . .	54
6.2	(a) Schematic diagram of the sample geometry. (b) Thermal resistance as a function of alucone and tincone film thickness. (c) Picosecond acoustic response of TDTR measurements for a 120 and 28.7 nm alucone and tincone film, respectively. (d) Thermal conductivity vs longitudinal sound speed for a wide range of polymers . . . . .	56
7.1	Cross-sectional STEM images of the tensile and compressive NMLs showing diffraction contrast and overlaid EDS elemental mapping of Cu and W . . . . .	60
7.2	SEM images of cross sections of as-deposited and annealed NMLs . . . . .	61
7.3	Schematic diagram of the sample geometry exhibiting the thermal resistances between the Al transducer and Si substrate . . . . .	62

7.4	Thermal conductivity of the tensile and compressive samples as a function of annealing temperature . . . . .	64
8.1	Schematic diagram of the crystal structure of $(\text{Hf}_{0.2}\text{Zr}_{0.2}\text{Ti}_{0.2}\text{Ta}_{0.2}\text{Nb}_{0.2})\text{B}_2$	68
8.2	(a) Temperature-dependent thermal conductivity of HEB measured via three different techniques: SSTR, TDTR, and LFA. (b) Temperature-dependent heat capacity of HEB along with that of $\text{ZrB}_2$ . . . . .	70
8.3	(a <sub>1</sub> , a <sub>2</sub> ) EBSD micrographs exhibiting the grain orientations in HEB and $\text{ZrB}_2$ . (b <sub>1</sub> , b <sub>2</sub> ) Pole figures exhibiting the distribution of 001 oriented grains along the Z-axis. (c <sub>1</sub> , c <sub>2</sub> ) Disorientation angle distributions extracted from the EBSD data. (d <sub>1</sub> , d <sub>2</sub> ) Thermal conductivity distributions extracted from TDTR mapping . . . . .	73
9.1	Structure of perovskite and Ruddlesden-Popper $\text{Ba}_{n+1}\text{Zr}_n\text{S}_{3n+1}$ . Ball-and-stick model of (a) <i>Pnma</i> perovskite $\text{BaZrS}_3$ and (b) <i>I4mmm</i> Ruddlesden-Popper $\text{Ba}_3\text{Zr}_2\text{S}_7$ showing grey $\text{TiS}_6$ octahedra and green BaS bonds. Red markers in (b) indicate the perovskite blocks of the RP phase separated by the rock-salt blocks. Ball-and-stick model of a (c) Zr octahedra and (d) undistorted Ba polyhedral. (e) Distorted Ba polyhedral resulting from octahedral tilts in $\text{BaZrS}_3$ and (f) rock-salt building block resulting from layering in $\text{Ba}_3\text{Zr}_2\text{S}_7$ . Integrated differential phase contrast images of the (g) $\text{BaZrS}_3$ , (h) $\text{Ba}_3\text{Zr}_2\text{S}_7$ , and (i) $\text{Ba}_4\text{Zr}_3\text{S}_{10}$ crystals. The (j) cross-plane projected Ba-Ba distance in (g-h) showing the periodic structure of the perovskite and rock-salt like sections of the RP phases. (k) atomic-number contrast image and (l) BaZr composite image from a STEM-EELS spectrum image. Intensity maps of (m) Ba-M <sub>45</sub> , (n) Zr-M <sub>23</sub> , and (o) S-K background-subtracted edges . . . . .	77
9.2	TDTR-measured cross-plane thermal conductivity of $\text{BaZrS}_3$ and its RP derivatives. (b) Elastic modulus/thermal conductivity ( $E/\kappa$ ) ratio for a wide range of crystalline materials at room temperature. (c) Thermal conductivity distribution of $\text{BaZrS}_3$ and RP phases as a function of ion-irradiation doses . . . . .	78

# List of Tables

4.1	SSTR- and TDTR-measured substrate thermal conductivity of the samples .	35
7.1	Thermal resistance between the Al transducer and the Si substrate for the as-deposited and annealed Cu/W NMLs, as derived by SSTR and TDTR . .	64
8.1	Thermal conductivity and volumetric heat capacity of the HEB specimen measured in this study . . . . .	69

# Chapter 1

## Introduction

Non-contact, optical, laser-based thermometry techniques, such as laser flash analysis (LFA), time-domain thermorefectance (TDTR), and frequency-domain thermorefectance (FDTR), have emerged as powerful tools for measuring the thermal properties of bulk and thin film materials [1, 2]. Each of these techniques works at a particular range of time and length scales based on their fundamental principles of operations. For example, LFA, while probably the most implemented method for measuring the thermal diffusivity of materials, works mostly on macroscopic samples with length scales usually greater than 100  $\mu\text{m}$  [3, 4]. Ultrafast thermorefectance techniques, such as TDTR and FDTR, on the other hand, operate at length scales ranging from nanometers to micrometers [5, 6]. The temporal resolution provided by these techniques are also approximately proportional to their length scales. While TDTR and FDTR can operate at picosecond to nanosecond resolution, LFA works at millisecond time scales or higher.

An overview of the characteristic time and length scales associated with these conventional optical thermometry techniques is exhibited in Figure 1.1. A gap exists between the temporal and spatial resolution provided by the ultrafast thermorefectance techniques and LFA. The recently-developed pump-probe technique, steady-state thermorefectance (SSTR) offers promise in bridging this gap. Based on the principles of Fourier's law, this technique operates at a novel regime of time and length scales previously inaccessible by

other thermometry techniques [7].

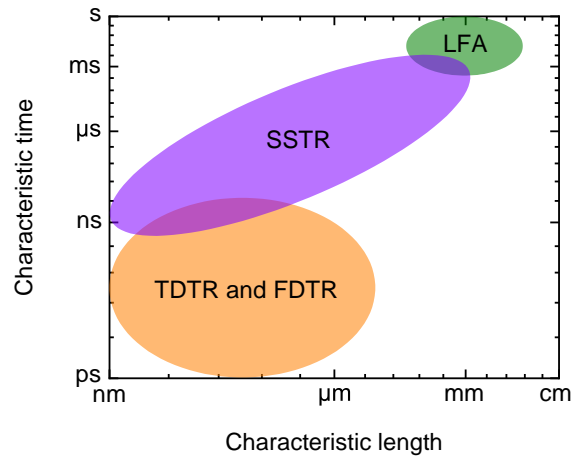


Figure 1.1: Characteristic time and length scales associated with the optical thermometry techniques.

Following its development in 2019, SSTR has emerged as a robust technique capable of circumventing the limitations of existing laser-based thermal measurement systems. In addition, it has the ability to probe nano-to-macro thermal transport mechanisms in new materials. For example, using its relatively larger length scale, SSTR can probe into sub-surface buried substrates and films that are typically inaccessible by TDTR and FDTR. Additionally, based on the sample geometry, SSTR has the capability to measure the in-plane thermal conductivity of non-metallic and metallic crystalline materials. Such measurements can provide insights into the transport mechanisms of highly conductive thin film materials and are relevant to solving the heat dissipation issue in electronic devices. SSTR measurements are also capable of shedding light into the thermal transport mechanisms of insulating hybrid polymers.

One of the biggest advantages of SSTR compared to other thermoreflectance techniques is its insensitivity to heat capacity. This allows SSTR to measure thermal conductivity of a material without prior knowledge of its heat capacity. This advantage also enables SSTR to measure the total thermal resistance of challenging multilayered geometries. These capabilities set SSTR apart from conventional thermometry techniques. However, due to the relatively new age of SSTR, these features have not been explored yet.

The overarching goal of this dissertation is to explore the new capabilities of SSTR to investigate the thermal transport mechanisms in thin film materials and expand SSTR's usage in challenging multilayered geometries. A brief overview of the dissertation is provided below:

- **Chapter 2: Theory** - In this chapter, I discuss the dominant energy carriers in non-metallic and metallic crystals as well as amorphous materials and describe their expected thermal conductivity trends.
- **Chapter 3: Experimental measurement techniques** - This chapter provides a brief overview of the thermoreflectance techniques I have used throughout the dissertation, namely, SSTR and TDTR.
- **Chapter 4: Measuring sub-surface buried substrates and films via SSTR** - In this chapter, I discuss the thermal penetration depth of SSTR technique and its ability to probe into sub-surface buried substrates and films.
- **Chapter 5: Investigating thermal transport in thermally conductive ultra-wide bandgap semiconductor films** - This chapter focuses on investigating in-plane thermal transport in highly conductive aluminum nitride (AlN) films with thicknesses ranging from 3.05 to 6  $\mu\text{m}$ .
- **Chapter 6: Investigating thermal transport in insulating polymers films** - In this chapter, I use SSTR to investigate the cross-plane thermal transport in organic-inorganic hybrid polymer films with thicknesses ranging from 1.4 to 120 nm.
- **Chapter 7: Measuring thermal resistance of multilayered geometries** - This chapter focuses on measuring thermal resistance of challenging multilayered geometries via SSTR.
- **Chapter 8: Extending SSTR measurements to high temperatures** - In this chapter, I extend thermal characterizations of a high-entropy ceramic beyond ambient conditions using SSTR.

- **Chapter 9: Validating heat capacity assumptions of a perovskite chalcogenide** - One of the biggest advantages of SSTR technique is its insensitivity to heat capacity. Here, I use this advantage of SSTR to validate heat capacity assumptions of a perovskite chalcogenide.
- **Chapter 10: Summary and future works** - In this chapter, I summarize the use of SSTR for each of the projects to signify its advantages compared to other laser-based thermometry techniques. I also provide future directions and next steps based on the works presented in this dissertation.

# Chapter 2

## Theory

In this chapter, I discuss the dominant energy carriers in non-metallic and metallic crystals as well as amorphous materials and describe their expected thermal conductivity trends.

### 2.1 Energy carriers in non-metallic crystals

#### 2.1.1 Phonons

Phonons are the primary energy carriers in a non-metallic crystal. The collective vibration of atoms around their equilibrium positions give rise to waves that propagate through the crystal. The normal modes of these atomic vibrations are quantized and defined as

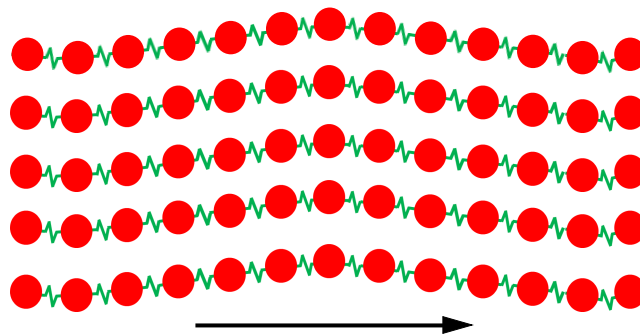


Figure 2.1: Phonon propagation through a crystal.

phonons. Phonons are quasi-particles that display both wave and particle-like behaviors. Figure 2.1 shows a schematic of phonon propagation through crystalline materials.

### 2.1.2 Phonon dispersion

The phonon dispersion curve provides the correlation between the phonon angular frequency and wavevector. The phonon group velocity (i.e., the speed of the wavepacket propagation) can be derived from the dispersion relation using the following equation:

$$v_j(k) = \frac{\partial \omega_j}{\partial k}, \quad (2.1)$$

where  $v$ ,  $\omega$ ,  $k$ , and  $j$  represent group velocity, angular frequency, wavevector, and phonon branch, respectively. The most simplistic way to derive the phonon dispersion relation for a system is the infinite one-dimensional atomic chain problem [8, 9]. In this problem, the atoms and interatomic bonds are represented by a spring-mass system. Assuming the crystal basis consists of one atom and each atom interacts with only the nearest neighbors, the following phonon dispersion relation can be obtained by solving the equations of motion:

$$\omega(k) = 2\sqrt{\frac{K}{m}} \left| \sin\left(\frac{ka}{2}\right) \right|, \quad (2.2)$$

where  $K$ ,  $m$ , and  $a$  represent the spring constant, atomic mass, and interatomic spacing, respectively. The phonon dispersion curve corresponding to equation 2.2 is depicted in Figure 2.2(a). It is adequate to plot the phonon dispersion curve for the first Brillouin zone due to the periodicity of the crystal.

The phonon branch shown in Figure 2.2(a) is referred to as the acoustic mode. In this mode, all atoms move in-phase with one another and angular frequency reaches zero at the zone center. Near the zone center, the angular frequency is linearly proportional to the wavevector and phonons have a constant group velocity. This is known as the Debye approximation which states that  $\omega(k) = v_s k$ , where  $v_s$  is the sound speed of the material. The Debye model is valid for low frequency acoustic phonons and overpredicts the group

velocity and frequency at the zone edge. The real group velocity approaches zero at the zone edge and creates a standing wave.

If the crystal basis consists of two atoms, the phonon dispersion relation can be expressed by the following equation:

$$\omega^2(k) = K \left( \frac{1}{m_1} + \frac{1}{m_2} \right) \pm K \left[ \left( \frac{1}{m_1} + \frac{1}{m_2} \right)^2 - \frac{4}{m_1 m_2} \sin^2 \left( \frac{ka}{2} \right) \right]^{1/2}. \quad (2.3)$$

The two solutions of the equation give rise to the acoustic and optical phonon branches as depicted in Figure 2.2(b). In the optical mode, atoms vibrate out-of-phase with one another and angular frequency never reaches zero. The two different masses of the diatomic chain give rise to the band gap at the zone edge. If both atoms of crystal basis possess the same mass, the band gap disappears.

Since Figure 2.2 depicts an one-dimensional atomic chain, all the phonon branches have one polarization, i.e., longitudinal. In a three-dimensional crystal, two additional transverse branches appear.

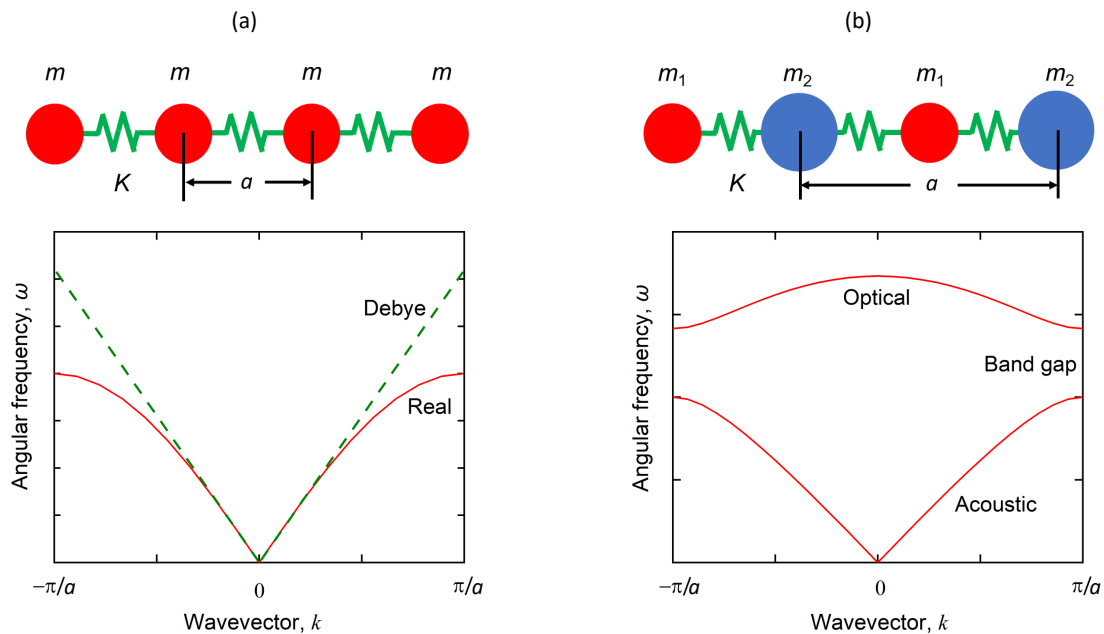


Figure 2.2: Phonon dispersion curves for (a) monoatomic and (b) diatomic chains. The models correspond to  $K = 1$ ,  $m = 1$ ,  $a = 1$ ,  $m_1 = 1$ , and  $m_2 = 2m_1$ .

### 2.1.3 Phonon heat capacity

Heat capacity defines the relationship between the absorbed energy and temperature rise in a system. The volumetric heat capacity of a non-metallic crystal can be expressed as the following:

$$C = \sum_j \int_0^{\omega_{\max,j}} \frac{\hbar^2 \omega^4 \exp\left[\frac{\hbar\omega}{k_B T}\right]}{2\pi^2 k_B T^2 v_j^3 \left(\exp\left[\frac{\hbar\omega}{k_B T}\right] - 1\right)^2} d\omega, \quad (2.4)$$

where  $C$ ,  $\hbar$ ,  $k_B$ ,  $T$ ,  $v$ , and  $j$  represent volumetric heat capacity, reduced Planck's constant, Boltzmann constant, temperature, sound speed, and phonon branch, respectively. The volumetric heat capacity of silicon (Si) is shown in Figure 2.3 as a function of temperature.

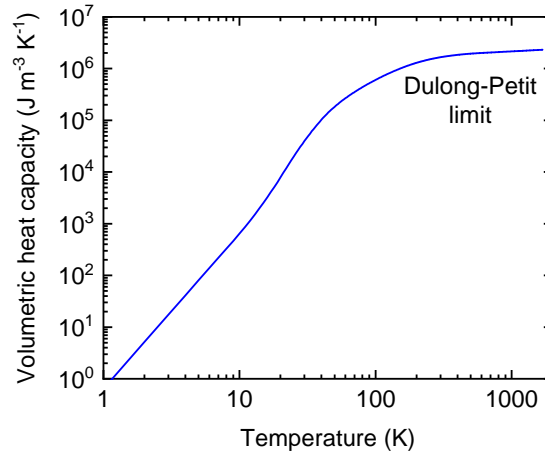


Figure 2.3: Volumetric heat capacity of Si taken from Ref [10].

At low temperatures, very few phonon modes are thermally excited. As a result, the volumetric heat capacity is quite small. As temperature increases, heat capacity continuously increases until all the phonon modes are thermally excited. At this point, the volumetric heat capacity becomes weakly dependent on temperature. This is known as the Dulong-Petit limit.

### 2.1.4 Phonon thermal conductivity

The phonon thermal conductivity of a crystalline material can be expressed as the following [11–13]:

$$\kappa = \frac{1}{3} \sum_j \int_0^{\omega_{\max,j}} \hbar \omega D_j(\omega) \frac{\partial f(\omega, T)}{\partial T} v_j^2(\omega) \tau_j(\omega) d\omega, \quad (2.5)$$

$$D_j(\omega) = \frac{\omega^2}{2\pi^2 v_j^3(\omega)}, \quad (2.6)$$

$$f(\omega, T) = \frac{1}{\exp\left[\frac{\hbar\omega}{k_B T}\right] - 1}, \quad (2.7)$$

$$\frac{1}{\tau_j} = \frac{1}{\tau_{pp,j}} + \frac{1}{\tau_{D,j}} + \frac{1}{\tau_{B,j}} = A T \omega^2 e^{-B/T} + C \omega^4 + v_j/d, \quad (2.8)$$

where  $\kappa$  is the thermal conductivity,  $D_j(\omega)$  is the density of states of branch  $j$ ,  $f(\omega, T)$  is the Bose-Einstein distribution function,  $\tau_j$  is total phonon scattering time of branch  $j$ ,  $A$ ,  $B$ , and  $C$  are material constants, and  $d$  is the characteristic length of the crystal. Using Matthiessen's rule, the total phonon scattering rate ( $1/\tau$ ) can be expressed as the summation of three major phonon scattering rates: phonon-phonon scattering rate ( $1/\tau_{pp}$ ), phonon-defect scattering rate ( $1/\tau_D$ ), and phonon-boundary scattering rate ( $1/\tau_B$ ). Figure 2.4 depicts the representative defects that drive different phonon scattering mechanisms. In the pure crystal of Figure 2.4(a), thermal conductivity is only influenced by phonon-phonon scattering. Due to presence of defects (e.g., vacancies and impurities) and boundaries in Figures 2.3(b) and 2.3(c), thermal conductivity is also influenced by phonon-defect and phonon-boundary scattering, respectively. Phonon-phonon scattering is known as the intrinsic scattering, whereas defect and boundary scattering are referred to as the extrinsic scattering.

The thermal conductivity of crystalline materials generally exhibits the same trend as a function of temperature. At low temperatures, thermal conductivity is proportional to heat

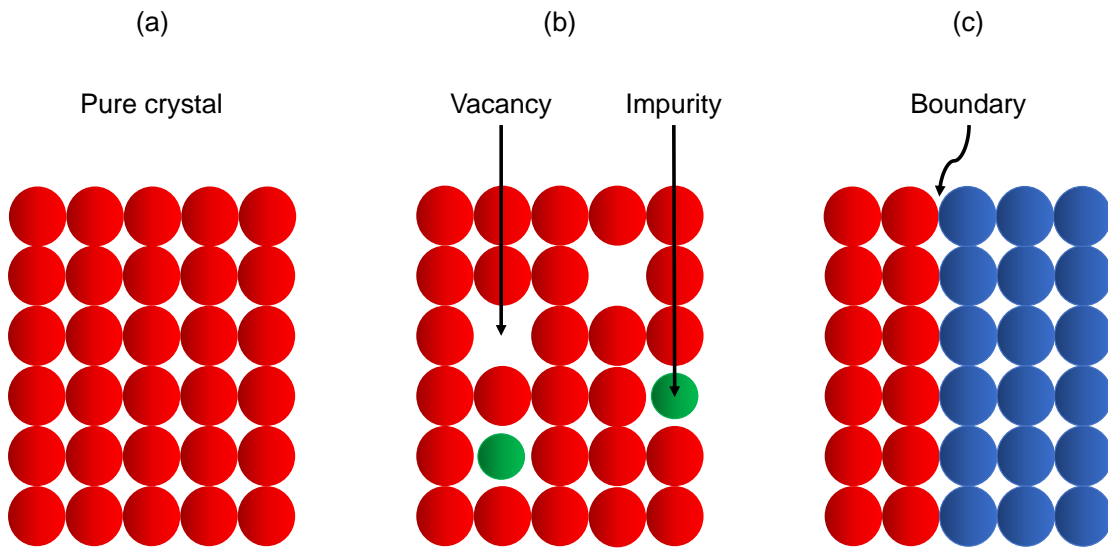


Figure 2.4: Representative crystal structures where the thermal conductivity is impacted by (a) phonon-phonon scattering, (b) phonon-defect scattering, and (c) phonon-boundary scattering.

capacity and increases with temperature. Defect and boundary scattering can dominate the thermal conductivity in this regime. As temperature increases, heat capacity reaches the Dulong–Petit limit and phonon-phonon scattering becomes increasingly important. As a result, thermal conductivity decreases with temperature often exhibiting a  $1/T^m$  ( $m = 1-1.5$ ) trend [14–16]. The resulting peak-shape temperature profile of thermal conductivity is shown in Figure 2.5(a) for crystalline Si.

A large concentration of extrinsic scattering sites can cause a deviation from the aforementioned trend. An example of this is shown in Figure 2.5(b) for  $\text{Ba}_{1-x}\text{La}_x\text{F}_{2+x}$  from Refs. [17, 18]. When  $x = 0$ , thermal conductivity exhibits the typical peak-shaped temperature profile. As  $x$  is increased to 0.045, thermal conductivity decreases significantly at all temperatures, but still exhibits the crystalline peak. When the  $\text{La}^{3+}$  concentration becomes 0.33, thermal conductivity first increases with heat capacity, then becomes weakly dependent on temperature, similar to amorphous materials. Some crystalline materials also exhibit the amorphous-like thermal conductivity trend due to intrinsic reasons, such as

complex crystal structures or the presence of rattling modes [19, 20].

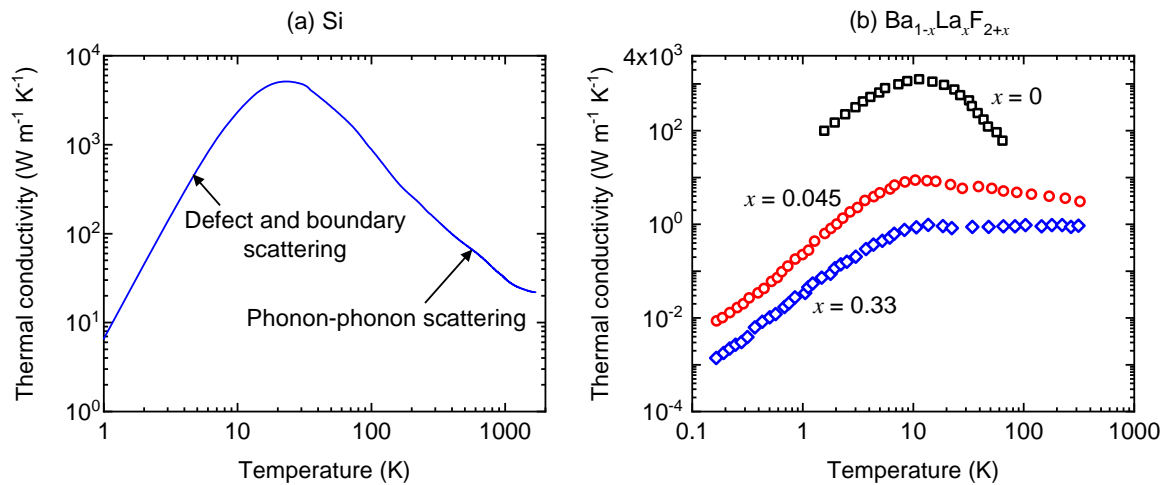


Figure 2.5: Thermal conductivity of crystalline (a) Si and (b)  $\text{Ba}_{1-x}\text{La}_x\text{F}_{2+x}$  as a function of temperature. Data is obtained from Ref. [21] for Si and Refs. [17, 18] for  $\text{Ba}_{1-x}\text{La}_x\text{F}_{2+x}$ .

## 2.2 Energy carriers in metallic crystals

### 2.2.1 Electrons

Electrons are the primary energy carriers in metallic crystals. Heat is transported through metals via diffusion of hot free electrons. Phonons also conduct heat in metals, but the contribution is usually much smaller compared to electrons. Figure 2.6 shows a schematic of electron diffusions in metals.

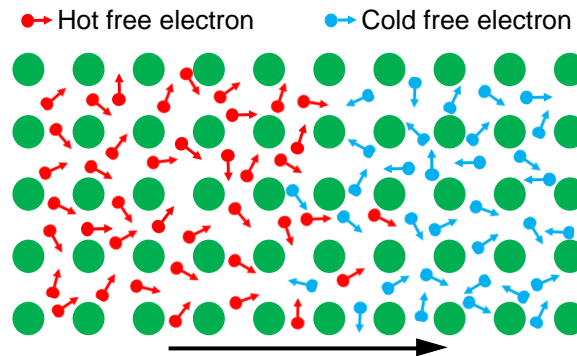


Figure 2.6: Diffusion of hot electrons in metals.

## 2.2.2 Electronic heat capacity

At low temperatures, the electronic heat capacity can be expressed as the following [13]:

$$C_e = \frac{\pi^2 k_B^2 N T_e}{2E_F} = \gamma T_e, \quad (2.9)$$

where  $C_e$ ,  $N$ ,  $T_e$ ,  $E_F$ , and  $\gamma$  represent electronic heat capacity, number of electrons, temperature of electrons, Fermi energy, and a material dependent constant, respectively. Figure 2.7 shows the volumetric heat capacity of platinum (Pt) as a function of temperature.

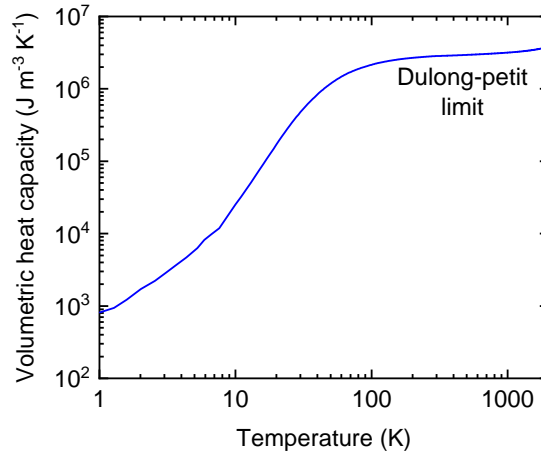


Figure 2.7: Volumetric heat capacity of Pt taken from Ref [22].

Both electrons and phonons contribute to the heat capacity of metals. At significantly low temperatures, the electronic heat capacity dominates. As temperature increases, the phonon contribution starts to dominate. Because of this reason, the volumetric heat capacity of metals reaches the classical Dulong-Petit limit at high temperatures.

## 2.2.3 Electronic thermal conductivity

The electronic thermal conductivity of a metal can be expressed as the following [23, 24]:

$$\kappa_e = \frac{\pi^2 k_B^2 N T_e \tau_{metal}}{3m}, \quad (2.10)$$

$$\frac{1}{\tau_{metal}} = \frac{1}{\tau_{ee}} + \frac{1}{\tau_{ep}} + \frac{1}{\tau_D} + \frac{1}{\tau_B}, \quad (2.11)$$

$$\frac{1}{\tau_{ee}} = AT_e^2, \quad (2.12)$$

$$\frac{1}{\tau_{ep}} = BT_p, \quad (2.13)$$

$$\frac{1}{\tau_D} \neq f(T_e, T_p), \quad (2.14)$$

$$\frac{1}{\tau_B} = v_F/d, \quad (2.15)$$

where  $\kappa_e$  is the electronic thermal conductivity,  $m$  is the mass of the conduction electrons,  $\tau_{metal}$  is the total carrier scattering time in metals, A and B are constants,  $T_p$  is the temperature of phonons, and  $v_F$  is the Fermi velocity. The total scattering rate ( $1/\tau$ ) in metals can be expressed as the summation of the electron-electron scattering rate ( $1/\tau_{ee}$ ), electron-phonon scattering rate ( $1/\tau_{ep}$ ), electron-defect scattering rate ( $1/\tau_D$ ), and electron-boundary scattering rate ( $1/\tau_B$ ). The electron-electron and electron-phonon scattering rates depend on electron and phonon temperatures, respectively, whereas, the electron-defect and electron-boundary scattering rates are temperature independent. In metals, electron-electron and electron-phonon scattering are known as intrinsic scattering and defect and boundary scattering are referred to as the extrinsic scattering. Electron-phonon scattering is the dominant intrinsic scattering mechanism and usually much stronger than electron-electron scattering.

Figure 2.8 shows the thermal conductivity of Pt as a function of temperature. Similar to semiconductors, the thermal conductivity of metals exhibit a peak-shaped profile. However, at high temperatures, the thermal conductivity of metals deviate from the trend observed in semiconductors due to electron-electron and electron-phonon scattering.

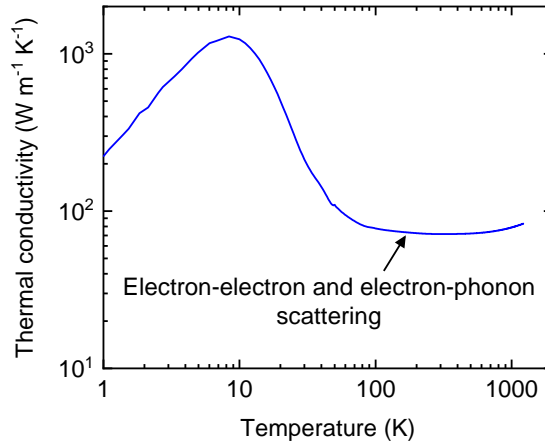


Figure 2.8: Thermal conductivity of Pt taken from Ref [25].

## 2.3 Energy carriers in non-metallic amorphous solids

### 2.3.1 Locons, diffusons, and propagons

Due to lack of any periodicity, energy carriers in amorphous solids are described using a different taxonomy. The vibrational modes of an amorphous material can be strictly classified into two categories: locons and extendons [26, 27]. Locons are localized vibrational modes that do not contribute to thermal conductivity. On the other hand, extendons are delocalized vibrational modes and primary energy carriers in an amorphous solid. The boundary between the two vibrational modes is known as the mobility edge. One effective way to distinguish between locons and extendons is the participation ratio ( $PR_n$ ) defined as the following [28]:

$$PR_n = \frac{\left(\sum_i e_{i,n}^2\right)^2}{N \sum_i e_{i,n}^4}, \quad (2.16)$$

where  $e_{i,n}$ ,  $N$ ,  $n$ , and  $i$  represent eigenvector, number of atoms, mode index, and individual atoms in the system, respectively. A vibrational mode is considered to be locon or extendon based on whether the  $PR_n$  is small or large, respectively. Locons usually have a  $PR_n$  less than 0.1 [29].

The extendons can be further classified into two categories: diffusons and propagons.

Diffusons are non-propagating vibrational modes without a defined wavevector or a mean free path. On the contrary, propagons are propagating vibrational modes with defined wavevectors and can travel at the sound speed over distances greater than the interatomic spacings before scattering. The boundary between diffusons and propagons is known as the Ioffe-Regel cross-over. Due to the delocalized nature of diffusons and propagons, differentiating between them can be challenging.

### 2.3.2 Thermal conductivity of non-metallic amorphous solids

Amorphous solids exhibit a completely different thermal conductivity trend compared to non-metallic and metallic crystals. Figure 2.9 shows the thermal conductivity of amorphous  $\text{SiO}_2$  (vitreous silica) as a function of temperature. The thermal conductivity first increases with temperature, reaches a plateau near 10 K, then becomes weakly dependent on temperature at high temperatures. The presence of a large concentration of extrinsic scattering sites can also cause a similar thermal conductivity trend in crystalline materials.

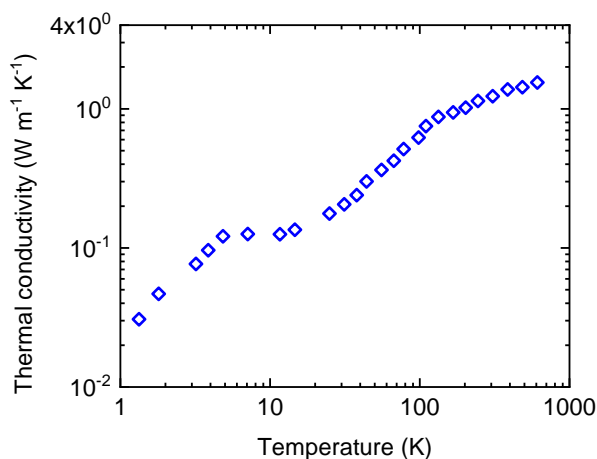


Figure 2.9: Thermal conductivity of amorphous  $\text{SiO}_2$  taken from Refs [19, 30–32].

## 2.4 Theoretical lower limits of thermal conductivity

To predict the lower limit of thermal conductivity in crystalline materials, multiple theoretical models have been proposed. The two most widely used among them are the glass limit and diffuson limit models. The glass limit model states that the lower bound of thermal conductivity can be achieved when the phonon mean free path reduces to half of its wavelength [19]. This model assumes that the heat is transported through a solid via random walks between localized oscillators. The glass limit model is also known as the minimum thermal conductivity or amorphous limit model and can be expressed as the following [17]:

$$\kappa_g = \left(\frac{\pi}{6}\right)^{1/3} k_B n^{2/3} \sum_j v_j \left(\frac{T}{\theta_j}\right)^2 \int_0^{\theta_j/T} \frac{x^3 e^x}{(e^x - 1)^2} dx, \quad (2.17)$$

$$\theta_j = v_j \left(\frac{h}{2\pi k_B}\right) (6\pi^2 n)^{1/3}, \quad (2.18)$$

where  $\kappa_g$ ,  $n$ ,  $h$ , and  $\theta$  represent thermal conductivity prediction, number density, Planck's constant, and Debye temperature, respectively.

The glass limit model has successfully predicted the thermal conductivity of many disordered solids and amorphous materials. However, several recent studies have showed that the thermal conductivity of a few materials can fall below this limit [33–36]. Therefore, to better estimate the theoretical lower bound of thermal conductivity, Agne *et al.* [37] predicted a model based on the diffuson-mediated thermal transport. The diffuson model assumes that the heat is transported through a material via diffusons. According to the diffuson model, the thermal conductivity ( $\kappa_d$ ) can be expressed as the following:

$$\kappa_d = \frac{n^{-2/3} k_B}{2\pi^3 v^3} \left(\frac{2\pi k_B T}{h}\right)^4 \int_0^{0.95 \frac{\theta}{T}} \frac{x^5 e^x}{(e^x - 1)^2} dx, \quad (2.19)$$

$$\theta = \frac{h}{2\pi k_B} (6\pi^2 n)^{1/3} v. \quad (2.20)$$

## Chapter 3

# Experimental measurement techniques

This chapter provides a brief overview of the thermorefectance techniques I have used throughout the dissertation, namely, steady-state thermorefectance and time-domain thermorefectance.

### 3.1 Steady-state thermorefectance (SSTR)

#### 3.1.1 Experimental details and signal analysis

The pump-probe technique steady-state thermorefectance (SSTR) is based on the principle that the change in reflectivity of a material is linearly proportional to its change in temperature [38]. A simplified schematic diagram of SSTR is shown in Figure 3.1(a). In this experimental setup, a 532 nm continuous-wave (CW) pump laser is modulated at a low frequency to generate a periodic heat flux at the sample surface for an extended period. The low modulation frequency from the chopper ensures that enough time has passed for the system to reach a quasi-steady-state condition. A 786 nm CW probe beam then measures the resultant steady-state temperature rise by detecting the change in surface reflectivity. By varying the pump power and monitoring the resulting change in reflectivity at each power, a linear relation between the heat flux and temperature rise is established. The thermal conductivity of the material can then be determined from this linear relationship using

Fourier's law. In our setup, the change in pump power is captured by a 90:10 beam splitter and a photodetector. Similarly, the surface reflectivity change is proportionally captured by a balanced photodetector and a lock-in amplifier.

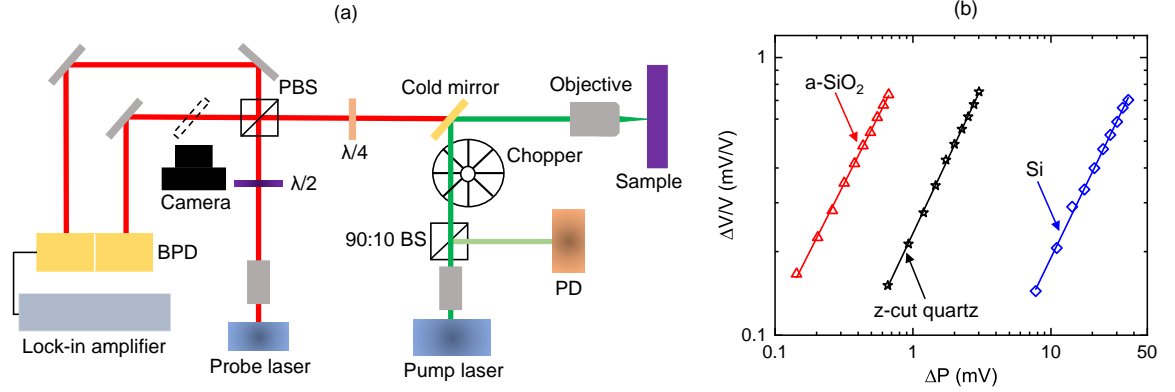


Figure 3.1: (a) A simplified schematic diagram of the SSTR setup. PD: photodetector, BPD: balanced photodetector, PBS: polarizing beam splitter, 90:10 BS: 90% transmission/10% reflection beam splitter, and  $\lambda/2$ ,  $\lambda/4$ : half- and quarter-wave plates, respectively. (b) Balanced photodetector response,  $\Delta V/V$  ( $\propto$  temperature rise) as a function of pump photodetector response,  $\Delta P$  ( $\propto$  pump power) for SSTR fitting of Al-coated bulk a-SiO<sub>2</sub>, z-cut quartz, and Si.

If we denote the pump photodetector response ( $\propto$  pump power) by  $\Delta P$ , heat flux change at the sample surface by  $\Delta Q$ , steady-state temperature rise by  $\Delta T$ , normalized reflectivity change by  $\Delta R/R$ , balanced photodetector response by  $\Delta V/V$ , and thermal conductivity by  $k$ , then the following equations can be obtained for SSTR measurements [7, 39]:

$$\Delta P \propto \Delta Q \propto \Delta T \propto \frac{\Delta R}{R} \propto \frac{\Delta V}{V}, \quad (3.1)$$

or,

$$\frac{\Delta V}{V \Delta P} = \gamma \frac{\Delta T (k)}{\Delta Q}, \quad (3.2)$$

here,  $\gamma$  is an experimental proportionality constant which is calculated from the comparison of experimentally measured  $\Delta V/(V \Delta P)$  of a reference sample with known thermal conductivity to the  $\Delta T$  predicted by a steady-state thermal model [7, 40, 41]. After  $\gamma$  is determined from the reference sample, the thermal conductivity of any other material can be

calculated from experimental measurements of corresponding  $\Delta V/(V\Delta P)$  and relating it to  $\Delta T(k)/\Delta Q$  predicted by the steady-state thermal model under the assumption that  $\gamma$  does not change between the reference and samples. To ensure the validity of this assumption, the reference and samples are kept in identical conditions during all SSTR measurements. Figure 3.1(b) shows the SSTR best-fit curves for determining the thermal conductivity of bulk a-SiO<sub>2</sub>, z-cut quartz, and Si. Prior to these measurements, a thin aluminum (Al) film is deposited atop the samples to convert the optical energy of the laser into thermal energy. Bulk sapphire is chosen as the reference sample for the measurements. SSTR measurements of sapphire are almost insensitive to the Al/sapphire thermal boundary conductance and Al thermal conductivity. This makes bulk sapphire an ideal reference sample. For this reason, sapphire has been successfully used in SSTR for measuring materials with thermal conductivities ranging from 0.05 to 2000 W m<sup>-1</sup> K<sup>-1</sup> [7, 42].

### 3.1.2 Analytical expression of steady-state temperature rise

In optical pump-probe measurements, the temperature rise at the sample surface is proportionally captured by the probe reflectivity change. Assuming radial symmetry in the cylindrical coordinate, the probe-averaged temperature rise ( $T_P$ ) for a bulk, single-layered material can be expressed as the following [40, 41, 43]:

$$T_P = \frac{4}{r_1^2} \int_0^\infty T(r) \exp\left(\frac{-2r^2}{r_1^2}\right) r dr, \quad (3.3)$$

here,  $r$  represents radial coordinate, and  $T(r)$  is the distribution of temperature oscillations at the sample surface due to the modulated heating event from the pump beam. Equation 3.3 assumes that both pump and probe beams have Gaussian profiles and negligible optical penetration depths. The  $1/e^2$  pump and probe radii are denoted by  $r_0$  and  $r_1$ , respectively.

In the extreme limits of low modulation frequency such as an unmodulated CW laser source, equation 3.3 can be analytically solved to become [41, 43]

$$T_P = \frac{P_0}{\sqrt{2\pi(r_0^2 + r_1^2)(k_{\parallel})(k_{\perp})}} = \frac{P_0}{r_{01}\sqrt{2\pi(k_{\parallel})(k_{\perp})}}, \quad (3.4)$$

here,  $r_{01} = \sqrt{r_0^2 + r_1^2}$  is the effective radius, and  $P_0$  is average power absorbed by the sample. For a bulk material, equation 3.4 provides an approximation of the steady-state temperature rise for conditions similar to SSTR measurement settings. As shown here, the probe-averaged steady-state temperature rise depends on the geometric mean of in-plane and cross-plane thermal conductivities. By rearranging the terms of equation 3.4, an expression for  $\sqrt{(k_{\parallel})(k_{\perp})}$  can be obtained. Additionally, there is no heat capacity ( $C$ ) term in equation 3.4 showing that the SSTR measurements are insensitive to heat capacity. Due to the low frequency characteristics of SSTR, its thermal penetration depth, i.e., the distance normal to the surface at which the temperature drops to the 1/e value of the maximum surface temperature, is dictated by the pump radius [1, 40].

For layered structures such as thin films on a substrate, analytically obtaining expressions similar to equation 3.4 becomes challenging. For such cases, the radially symmetric heat diffusion equation is numerically solved to determine the thermal conductivity tensor of SSTR measurements [7, 40].

### 3.1.3 Sensitivity analysis

The SSTR sensitivity expression can be obtained by following a methodology similar to that of Yang *et al* [6]. For FDTR measurements, Yang *et al.* [6] quantified the sensitivity,  $S_x$ , of the thermal model as the change in the phase ( $\phi$ ) signal caused by the variation of a parameter,  $x$ , within a tolerance limit of  $\pm 10\%$ . According to this definition,  $S_x = \phi_{1.1x}(\omega) - \phi_{0.9x}(\omega)$ , where  $\omega$  is the frequency.

We adopt a similar approach for defining the sensitivity of SSTR measurements. However, since SSTR measures the magnitude ( $\propto$  steady-state temperature rise) instead of phase, a division term is added to the definition to make the comparison of sensitivities among samples of different properties and geometries fair [7]. Therefore,

$$S_x = \frac{|\Delta T_{1.1x}(r_{01}) - \Delta T_{0.9x}(r_{01})|}{\Delta T_x(r_{01})}, \quad (3.5)$$

here,  $\Delta T_x$  is the temperature rise predicted by the steady-state thermal model [7] for an input parameter  $x$ . We define  $S_x$  in terms of effective radius,  $r_{01}$ , as SSTR offers a convenient way to change sensitivities to different parameters by using multiple pump and probe radii. However,  $S_x$  can also be expressed in terms of modulation frequency or any other parameters of interest.

For bulk materials, SSTR measures the geometric mean of  $k_{\parallel}$  and  $k_{\perp}$  and has nearly equal sensitivity to both  $k_{\parallel}$  and  $k_{\perp}$ . However, for thin film measurements, this changes based on thin film to substrate thermal conductivity ratios [7]:

(a) If the thin film thermal conductivity is much higher than that of the substrate, heat flows predominantly along the in-plane direction of the film. In this case, the in-plane thermal conductivity of the film dominates the sensitivity calculations allowing SSTR to directly measure  $k_{\text{thin film } \parallel}$ .

(b) When the thermal conductivity of the thin film and substrate are equal, heat flows almost equally along the in-plane and cross-plane directions. This results in near-identical temperature gradients in both directions. For such a case, sensitivity to the in-plane and cross-plane thermal conductivities of the film are nearly the same. Thus, SSTR measures  $\sqrt{(k_{\text{thin film } \parallel})(k_{\text{thin film } \perp})}$ .

(c) For the case where the thin film thermal conductivity is much lower than substrate, the majority of the heat flows towards the highly conductive substrate. Here, the temperature gradient in the cross-plane direction becomes very large. As a result, sensitivity to the cross-plane thermal conductivity of the thin film is much higher compared to that of in-plane. Therefore, SSTR measurements represent  $k_{\text{thin film } \perp}$ .

Figure 3.2(a) shows the heat flow directions for the three cases. The sensitivity calculations for a 3.05  $\mu\text{m}$  AlN thin film on sapphire substrate is exhibited in 3.2(b). As the thermal conductivity of AlN is nearly an order of magnitude higher than that of sapphire, SSTR measurements are overwhelmingly sensitive to the in-plane thermal conductivity of

the AlN films.

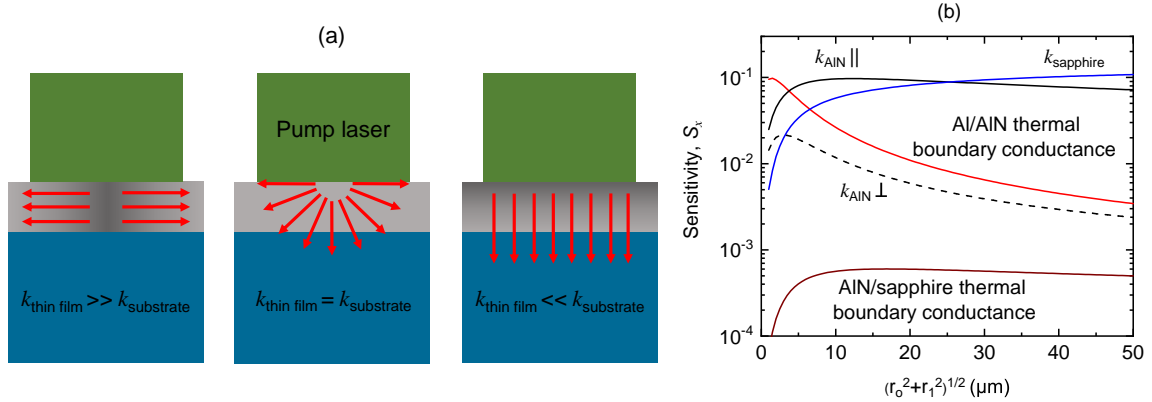


Figure 3.2: (a) Heat flow directions during SSTR measurements of a thin film on a substrate. The three cases considered here are:  $k_{\text{thin film}} \gg k_{\text{substrate}}$ ,  $k_{\text{thin film}} = k_{\text{substrate}}$ , and  $k_{\text{thin film}} \ll k_{\text{substrate}}$ . (b) Sensitivity calculations for a  $3.05 \mu\text{m}$  AlN thin film on sapphire substrate. The calculations correspond to a modulation frequency of 100 Hz, Al transducer thickness of 77 nm, Al transducer, AlN, and sapphire thermal conductivities of 130, 260, and  $35 \text{ W m}^{-1} \text{ K}^{-1}$ , respectively, and Al/AIN and AlN/sapphire thermal boundary conductances of 120 and  $200 \text{ MW m}^{-2} \text{ K}^{-1}$ , respectively.

### 3.1.4 Uncertainty analysis

The uncertainty of SSTR measurements is calculated according to the following equation [7]:

$$\Delta = \sqrt{(\sigma)^2 + \sum_i \Delta_i^2}, \quad (3.6)$$

where  $\Delta$  is the total uncertainty,  $\sigma$  is the standard deviation among multiple measurements across different spots, and  $\Delta_i$  is the uncertainty due to an individual parameter.

## 3.2 Time-domain thermorefectance (TDTR)

Along with SSTR, another thermal conductivity measurement technique I have extensively used throughout my PhD is time-domain thermorefectance (TDTR). Figure 3.3(a) shows a simplified schematic diagram of our two-color TDTR setup. In this setup, a Ti:sapphire laser with a central wavelength of  $\sim 800$  nm and a full width at half maximum of  $\sim 10$  nm emanates sub-picosecond laser pulses. The repetition rate and pulse width of the laser are 80 MHz and  $\sim 100$  fs, respectively. Using a polarizing beam splitter, the laser output is split into a pump and a probe path. The 800 nm pump beam is first modulated at a frequency of 1 to 10 MHz via an electro-optic modulator, then frequency doubled to 400 nm by using a Bismuth Borate crystal. The unmodulated 800 nm probe beam is directed to a mechanical translation stage to delay it up to  $\sim 5.5$  ns compared to the pump beam. The spatially overlapped pump and probe beams are then focused onto the sample surface using a microscopic objective. The probe beam detects the reflectivity change due to the surface temperature oscillations using a balanced photodetector and a lock-in amplifier. Similar to SSTR, TDTR technique requires a thin Al film atop the sample surface for optothermal transduction.

I have also used a two-tint version [44, 45] of TDTR setup where the central wavelength is  $\sim 808$  nm. In the two-tint setup, no Bismuth Borate crystal is used to frequency double the pump beam, instead sharp-edge optical filters are used to spectrally separate the pump and probe beams by just a few nanometers. Aside from this difference, the two versions are nearly identical.

In TDTR, the thermal properties of a sample are determined by fitting a radially symmetric, multilayer heat diffusion model to the ratio of the in-phase to out-of-phase signal ( $-V_{\text{in}}/V_{\text{out}}$ ) from the lock-in amplifier. Figure 3.3(b) shows the TDTR best-fit curves for determining the thermal conductivity of a-SiO<sub>2</sub>, sapphire, and Si. Details of TDTR data acquisition, signal analysis, sensitivity, and uncertainty calculations can be found in literature [43, 46–49].

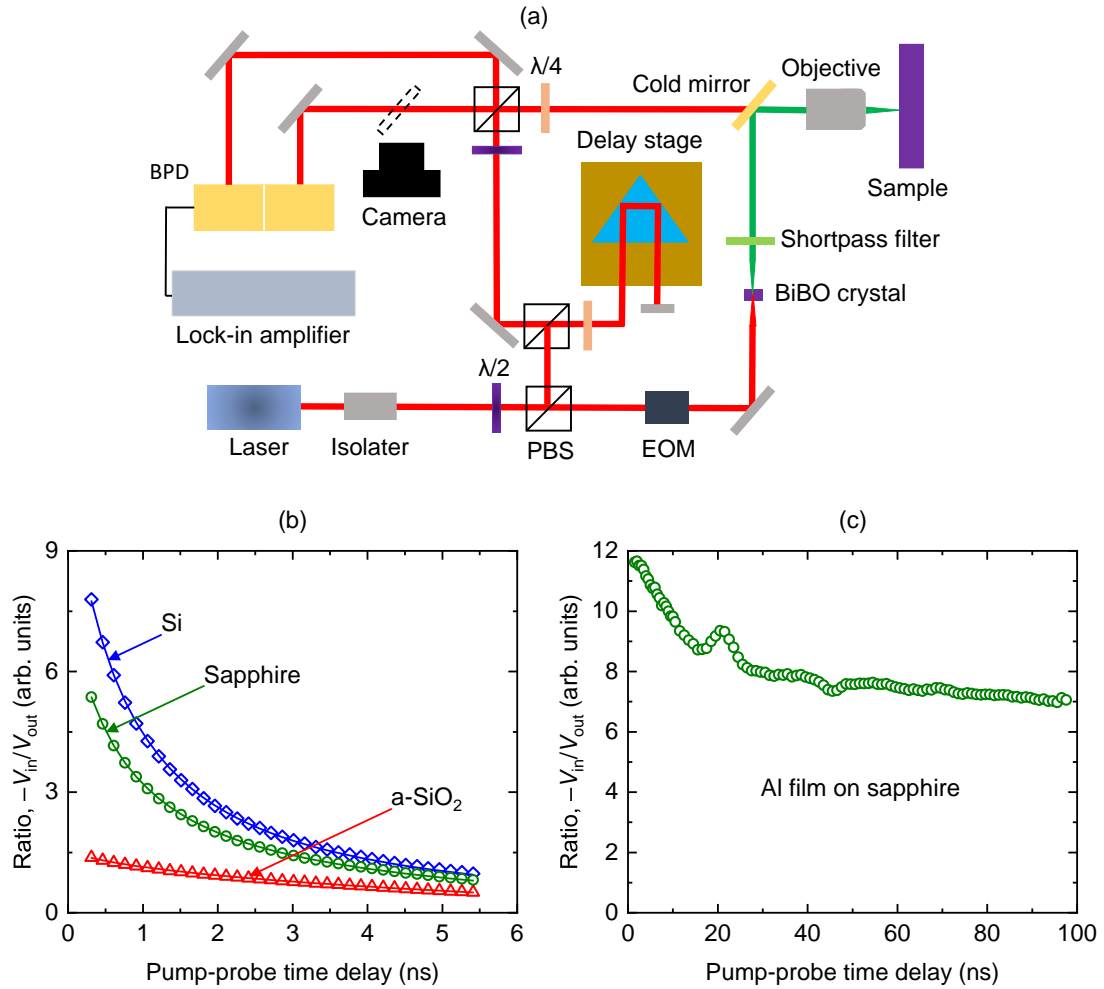


Figure 3.3: (a) A simplified schematic diagram of the two-color TDTR setup. EOM: electro-optic modulator and BiBO crystal: Bismuth Borate crystal. (b) Ratio of in-phase to out-of-phase signal ( $-V_{in}/V_{out}$ ) as a function of pump-probe delay time for TDTR fitting of Al-coated bulk a-SiO<sub>2</sub>, sapphire, and Si. (c) Picosecond acoustic response for a  $\sim 80$  nm Al transducer on sapphire.

In addition to thermal conductivity measurements, I have used TDTR for picosecond acoustics, which is a useful way to determine the longitudinal sound speed of a thin film material [50–54]. During picosecond acoustics, the heating event from the pump beam launches a strain wave that propagates through the sample structure. The interfaces partially reflect the strain wave, which is captured by the probe beam at earlier pump-probe delay times. A "hump" or "trough" is generated in the TDTR thermal decay curves based on whether the reflecting material possesses a higher or lower acoustic impedance, respectively. With the knowledge of the propagation time period and film thickness, the

longitudinal sound speed of a thin film material can be calculated. Figure 3.3(c) shows the picosecond acoustic response of TDTR measurements for a  $\sim 80$  nm Al film on sapphire substrate.

## Chapter 4

# Measuring sub-surface buried substrates and films via SSTR

In this chapter, I discuss the thermal penetration depth of SSTR technique and its ability to probe into sub-surface buried substrates and films. The findings of this chapter have been published in *Review of Scientific Instruments* [55].

### 4.1 Motivation

Thin films with thicknesses ranging from nanometer to micrometer length scales have become an integral part of transistors [56, 57], thermoelectric devices [58], optical coatings [59], solar cells [60], and memory devices [54, 61, 62]. As the device efficiency and reliability are often dictated by the thermal performance, it is of crucial importance to properly characterize the thermal properties of thin films and substrates [63]. Traditional optical pump-probe and electrothermal methods, such as TDTR [43, 47, 49, 64], FDTR [65], and  $3\omega$  method [66, 67] are widely used to measure the thermal conductivity of thin films [68]. However, both TDTR and FDTR have shallow thermal penetration depths ( $\sim 0.2\text{--}3\ \mu\text{m}$ ) under standard operating conditions [2, 7]. As a result, they often cannot measure thermal conductivity of buried substrates located beyond these length scales. The disadvantages of

the  $3\omega$  method, on the other hand, include its requirement of large and flat sample surface [69], complex microfabrication [70], and challenging sample preparation, particularly for electrically conducting and semiconducting materials [2]. These requirements can often limit the applicability of  $3\omega$  method for buried substrate measurements. SSTR technique offers a solution to these issues as its thermal penetration depth can be much larger than those produced during TDTR and FDTR measurements [7, 71]. In addition, SSTR is well suited for electrically conducting or semiconducting materials and can operate on an optically smooth surface of  $100 \times 100 \mu\text{m}^2$  area or less [7, 72]. Therefore, in this chapter, I provide an overview of the thermal penetration depth of SSTR technique and its ability to measure the thermal conductivity of sub-surface buried substrates and films.

## 4.2 Thermal penetration depth of SSTR technique

The thermal penetration depth (TPD) of SSTR technique is defined as the distance normal to the surface at which the temperature drops to the  $1/e$  value of the maximum surface temperature ( $T_{\text{max}}$ ) [1, 40, 41, 73]. According to this definition, the  $1/e^2$  heater (pump) radius represents the upper limit of the TPD [1]. However, such a description of the TPD fails for multilayer material systems (e.g., a thin film on a substrate). In such systems, the TPD can change widely based on the ratio of thin film to substrate thermal conductivity and the thermal boundary conductance between the thin film and substrate. This is further complicated by the presence of thin metal film transducers at the sample surface, which are often a requirement in optical pump-probe techniques for optothermal transduction [5, 74–77]. In subsequent sections, we discuss about the impact of metallic transducer and multilayered geometry on the SSTR TPD.

### 4.2.1 Impact of metallic transducer on thermal penetration depth

We first review the TPD of a 2-layer system: metal transducer on a substrate. The substrate here represents a bulk isotropic material. The TPD is calculated by solving the

cylindrical heat diffusion equation, detailed descriptions of which are provided elsewhere [40]. For these calculations,  $1/e^2$  pump and probe radii of  $10\ \mu\text{m}$  are used. The modulation frequency ( $f$ ) is chosen to be  $100\ \text{Hz}$  as it represents a realistic value usable in an experiment. We further assume that all the energy is absorbed in an infinitesimal thin layer on the surface (i.e., surface boundary condition).

In Figure 4.1(a), the TPD corresponding to the  $1/e$  temperature drop distance from the surface is presented for two scenarios, with and without the inclusion of a transducer. When no transducer is present, the change in the TPD is very small with respect to the substrate thermal conductivity. The small decrease in the TPD with substrate thermal conductivity reduction can be attributed to the choice of modulation frequency. For a given pump and probe radii, the lower the substrate thermal conductivity, the longer it takes for the system to reach steady-state [7]. Thus, as the substrate thermal conductivity decreases, the system slightly deviates from the ideal steady-state condition ( $f = 0$ ). To keep the TPD constant, the modulation frequency needs to be lowered in accordance with the substrate thermal conductivity reduction. However, for the chosen modulation frequency of  $100\ \text{Hz}$ , the

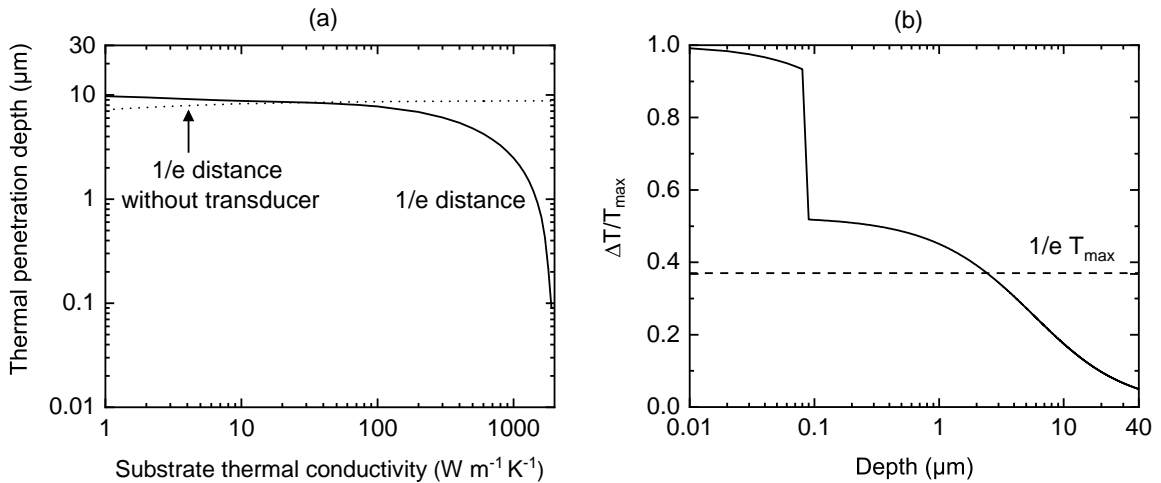


Figure 4.1: (a) Thermal penetration depth as a function of substrate thermal conductivity for a 2-layer system: metal transducer on a substrate. (b) Normalized temperature drop ( $\Delta T/T_{\text{max}}$ ) as a function of depth for a substrate thermal conductivity of  $1000\ \text{W m}^{-1} \text{K}^{-1}$ . The calculations correspond to  $f = 100\ \text{Hz}$ ,  $d_1 = 80\ \text{nm}$ ,  $r_0 = r_1 = 10\ \mu\text{m}$ ,  $k_1 = 100\ \text{W m}^{-1} \text{K}^{-1}$ ,  $C_1 = C_2 = 2\ \text{MJ m}^{-3} \text{K}^{-1}$ , and  $G_1 = 200\ \text{MW m}^{-2} \text{K}^{-1}$ . Here,  $d$  and  $G$  represent thickness and thermal boundary conductance, respectively.

deviation from the ideal steady-state condition is quite small for the substrate thermal conductivities considered here and therefore, the system can still be reasonably approximated to be in steady-state [7].

The presence of a high thermal conductivity ( $100 \text{ W m}^{-1} \text{ K}^{-1}$ ) metallic transducer drastically changes the TPD. For instance, when the substrate thermal conductivity is low ( $< 10 \text{ W m}^{-1} \text{ K}^{-1}$ ), the TPD with the transducer is higher than the TPD without the transducer. This stems from the radial heat spreading in the transducer and a corresponding increase in the overall heater radius [1]. On the other hand, when the substrate thermal conductivity is high ( $> 100 \text{ W m}^{-1} \text{ K}^{-1}$ ), the TPD with the transducer sharply decreases. With the increase of substrate thermal conductivity, the thermal resistance offered by the probed region gradually decreases. This leads to an increasingly important role of the interfacial thermal resistance. As a result, for high thermal conductivity substrates, the temperature drop at the transducer/substrate interface can become comparable to or even greater than that in the substrate [1]. This is exemplified in Figure 4.1(b), where we present the normalized temperature drop as a function of depth for a substrate thermal conductivity of  $1000 \text{ W m}^{-1} \text{ K}^{-1}$ . In this example, the temperature decreases by nearly 41% at the transducer/substrate interface, leading to a TPD of  $2.48 \text{ }\mu\text{m}$ .

#### 4.2.2 Impact of multilayered geometry on thermal penetration depth

We now extend the TPD discussion to a 3-layer system with the following geometry: metal transducer/thin film/substrate. When the thin film and substrate thermal conductivities are nearly equal, the TPD will closely follow those shown in Figure 4.1(a) with a minor influence from the thermal boundary conductance between the thin film and substrate. Thus, we consider two extreme cases of this hypothetical geometry: an insulating film on a conductive substrate ( $k_2 = 10 \text{ W m}^{-1} \text{ K}^{-1}$  and  $k_3 = 100 \text{ W m}^{-1} \text{ K}^{-1}$ ), and a conductive film on an insulating substrate ( $k_2 = 100 \text{ W m}^{-1} \text{ K}^{-1}$  and  $k_3 = 10 \text{ W m}^{-1} \text{ K}^{-1}$ ).

In Figures 4.2(a) and 4.2(b), we present the TPD corresponding to the  $1/e$  temperature drop distance as a function of thin film thickness for the first and second case, respectively.

It is evident that the TPD with and without the presence of a transducer are nearly identical. This is due to the fact that the thin film thermal conductivities are 10 and 100  $\text{W m}^{-1} \text{K}^{-1}$  for the two cases considered here. For this range of thermal conductivities, the transducer does not have a significant impact on the TPD. From Figures 4.2(a) and 4.2(b), it is also clear that the TPD changes greatly with the film thickness when there is a significant difference between thin film and substrate thermal conductivities. Interestingly, the influence of the thin film on the TPD does not subside until the film thickness is approximately four times the heater radius. To understand the rationale behind this, it is necessary to review how the ratio of thin film to substrate thermal conductivity influences the heat flow direction.

In Figures 4.2(c) and 4.2(d), we study the normalized temperature drop as a function of depth for the first and second case, respectively. When the thin film is insulating and the substrate is conductive, the bulk of the heat flows along the cross-plane direction of the thin film. Due to this, a large temperature gradient exists in the thin film along the cross-plane direction as shown in Figure 4.2(c). Therefore, in this case, the TPD is much lower than the heater radius unless the thin film thickness is too high or too low. On the other hand, when the thin film is conductive and the substrate is insulating, the majority of the heat flows along the in-plane direction of the thin film. Thus, the temperature gradient along the cross-plane direction of the thin film is quite small. As a result, the TPD can be much higher than the heater radius as evident in Figure 4.2(d).

To provide a more visual representation of this, the temperature profiles [40] of SSTR measurements are shown for a 3  $\mu\text{m}$  thin film corresponding to the first and second case in Figures 4.2(e) and 4.2(f), respectively. For the insulating thin film case, temperature decreases greatly along the cross-plane direction of the film, whereas for the conductive film case, such temperature decrease is much smaller. However, for the conductive thin film case, temperature decrease is significant along the in-plane direction. This is in alignment with our discussion.

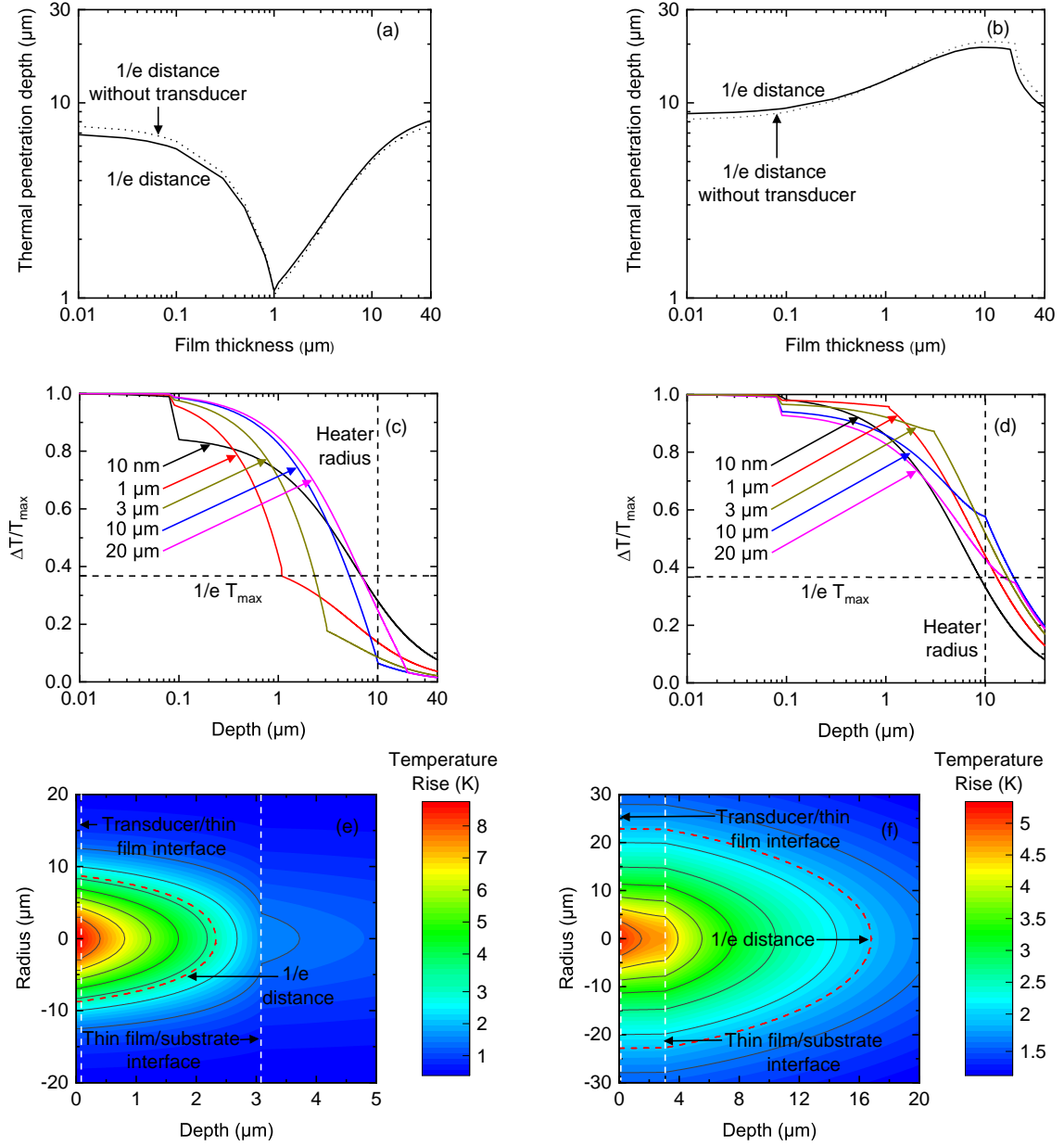


Figure 4.2: [(a) and (b)] Thermal penetration depth as a function of film thickness for a 3-layer system: metal transducer/thin film/substrate. [(c) and (d)] Normalized temperature drop as a function of depth for five different thin film thicknesses. [(e) and (f)] Temperature profiles of SSTR measurements for a 3  $\mu\text{m}$  thin film on a substrate corresponding to an absorbed power of 5 mW. Panels (a), (c), and (e) represent the case of an insulating film on a conductive substrate ( $k_2 = 10 \text{ W m}^{-1} \text{ K}^{-1}$  and  $k_3 = 100 \text{ W m}^{-1} \text{ K}^{-1}$ ), whereas panels (b), (d), and (f) represent the case of a conductive film on an insulating substrate ( $k_2 = 100 \text{ W m}^{-1} \text{ K}^{-1}$  and  $k_3 = 10 \text{ W m}^{-1} \text{ K}^{-1}$ ). The calculations correspond to  $f = 100 \text{ Hz}$ ,  $d_1 = 80 \text{ nm}$ ,  $r_0 = r_1 = 10 \mu\text{m}$ ,  $k_1 = 100 \text{ W m}^{-1} \text{ K}^{-1}$ ,  $C_1 = C_2 = C_3 = 2 \text{ MJ m}^{-3} \text{ K}^{-1}$ , and  $G_1 = G_2 = 200 \text{ MW m}^{-2} \text{ K}^{-1}$ .

### 4.3 Measurements of buried substrates

To demonstrate the ability of SSTR to measure the thermal conductivity of buried substrates, we choose three samples with the following 3-layer geometry: Al transducer/thin film/substrate. The schematics of the three samples are shown in Figures 4.3(a–c). The first sample is a  $\sim 130$  nm a-SiO<sub>2</sub> thin film on Si substrate. This sample represents an insulating film on a conductive substrate. The second sample is a  $\sim 2.05$   $\mu\text{m}$  unintentional doped (UID) GaN thin film on hydride vapor phase epitaxy (HVPE) n-GaN substrate. This sample represents the case where the thin film and substrate thermal conductivities are nearly equal. The third sample is a  $\sim 2$   $\mu\text{m}$  molecular beam epitaxy (MBE) grown AlN thin film on sapphire substrate. This sample represents a conductive film on an insulating substrate. Under standard operating conditions, it is often challenging to measure the thermal conductivity of such buried substrates by TDTR and FDTR due to their limited thermal penetration depths.

In the  $\sim 130$  nm a-SiO<sub>2</sub> thin film on Si sample, we use co-axially focused  $1/e^2$  pump and probe radii of  $\sim 10$   $\mu\text{m}$  to measure the thermal conductivity of buried Si substrate. The sensitivity calculation for this sample is shown in Figure 4.3(d). As shown here, SSTR measurements of the Si substrate are sensitive to the cross-plane thermal conductivity of the SiO<sub>2</sub> thin film. TDTR is used to measure the cross-plane thermal conductivity of the SiO<sub>2</sub> thin film. Using this SiO<sub>2</sub> value as an input, the SSTR-measured thermal conductivity of the Si substrate is  $141 \pm 27$  W m<sup>-1</sup> K<sup>-1</sup>. Figure 4.3(d) indicates that the sensitivity to SiO<sub>2</sub> cross-plane thermal conductivity is very high when the pump and probe radii are 10  $\mu\text{m}$ . As a result, the uncertainty associated with the Si thermal conductivity is also high,  $\sim 19\%$ . The sensitivity calculation also shows that using larger spot sizes, the sensitivity to SiO<sub>2</sub> and corresponding uncertainty of Si measurement can be reduced. To demonstrate this, we repeat the measurement with  $1/e^2$  pump and probe radii of  $\sim 20$   $\mu\text{m}$ . The resultant Si thermal conductivity is  $140 \pm 18$  W m<sup>-1</sup> K<sup>-1</sup>. As predicted, the measurement with the 20  $\mu\text{m}$  spot sizes has a reduced uncertainty of  $\sim 13\%$ .

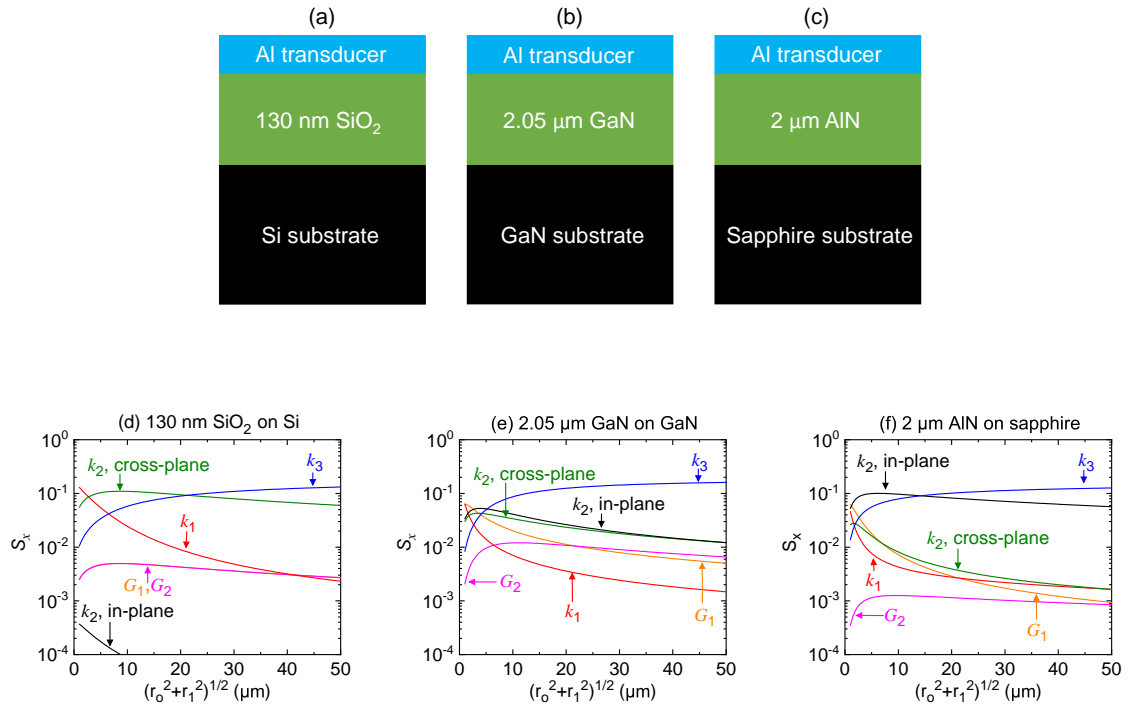


Figure 4.3: Schematics of the 3-layer samples measured by SSTR: (a)  $\sim 130$  nm SiO<sub>2</sub> thin film on Si substrate, (b)  $\sim 2.05$  μm GaN thin film on n-GaN substrate, and (c)  $\sim 2$  μm AlN thin film on sapphire substrate. Panels (d), (e), and (f) represent the sensitivity calculations as a function of effective radius for the three samples shown in panels (a), (b), and (c) respectively.

In the  $\sim 2.05$  μm GaN thin film on n-GaN substrate sample, we measure the thermal conductivity of the n-GaN substrate by SSTR using  $\sim 10$  and  $20$  μm spot sizes. GaN samples of similar geometries have received significant attention in recent years for thermal management applications of high-power and high-frequency electronic devices [16, 78–81]. The sensitivity calculation for our sample is presented in Figure 4.3(e). The sensitivity to the in-plane and cross-plane thermal conductivities of the GaN thin film are considerably lower when the spot sizes are  $20$  μm compared to the  $10$  μm spot sizes. The cross-plane thermal conductivity of the GaN thin film is measured by TDTR. At room temperature, the in-plane and cross-plane thermal conductivity of the GaN thin film can be considered to be the same [82]. The SSTR-measured thermal conductivity of the GaN substrate is  $194 \pm 27$  W m<sup>-1</sup> K<sup>-1</sup> when the spot sizes are  $10$  μm. Using spot sizes of  $20$  μm, the thermal

conductivity of the GaN substrate is measured with a lower uncertainty to be  $185 \pm 16 \text{ W m}^{-1} \text{ K}^{-1}$ .

The thermal conductivity of the sapphire substrate is measured by SSTR in the  $\sim 2 \mu\text{m}$  AlN thin film on sapphire sample. The sensitivity calculation for this sample is shown in Figure 4.3(f). SSTR measurement of the sapphire substrate thermal conductivity is most sensitive to the in-plane thermal conductivity of the AlN thin film. The cross-plane thermal conductivity of this AlN thin film is measured by TDTR. As the anisotropy in the AlN thermal conductivity is very small at room temperature [83], the in-plane and cross-plane thermal conductivities of the  $2 \mu\text{m}$  AlN thin film can be assumed to be the same. Using SSTR, the thermal conductivity of the sapphire substrate is measured to be  $35.1 \pm 5.9 \text{ W m}^{-1} \text{ K}^{-1}$  with  $1/e^2$  pump and probe radii of  $10 \mu\text{m}$ . Similar to the other two samples, with  $20 \mu\text{m}$  spot sizes, the sapphire thermal conductivity can be determined with a lower uncertainty,  $34.5 \pm 4.2 \text{ W m}^{-1} \text{ K}^{-1}$ .

In Table 4.1, we present the SSTR-measured substrate thermal conductivities for the two spot sizes. The uncertainty of the measured values incorporate the uncertainty associated with the  $\gamma$  value (sapphire reference), Al transducer and thin film thermal conductivity, thin film thickness, and the thermal boundary conductances. The values of these parameters are tabulated in Table 4.1. As shown in Table 4.1, the measured substrate thermal conductivities are in excellent agreement with literature.

For comparison, we also measure the substrate thermal conductivities with TDTR. These substrates are inaccessible with the typical modulation frequency ( $\sim 8\text{--}10 \text{ MHz}$ ) used in TDTR setups [45, 84–87]. Therefore, to enable these measurements, we use a low modulation frequency of  $1 \text{ MHz}$ . Even with this low modulation frequency, the TDTR TPD [40, 71, 73] is much lower than that of SSTR. As a result, the uncertainty associated with the TDTR measurements are significantly higher compared to SSTR as evident in Table 4.1. This proves the superiority of SSTR for accurately measuring the thermal conductivity of sub-surface buried substrates.

Table 4.1: SSTR- and TDTR-measured substrate thermal conductivity of the samples shown in Figure 4.3.

Substrates	Thermal conductivity ( $\text{W m}^{-1} \text{K}^{-1}$ )			
	SSTR		TDTR	Literature
	Spot size $10 \mu\text{m}$	Spot size $20 \mu\text{m}$		
Si	$141 \pm 27$	$140 \pm 18$	$132 \pm 32$	140 [88]
GaN	$194 \pm 27$	$185 \pm 16$	$213 \pm 60$	195 [89]
Sapphire	$35.1 \pm 5.9$	$34.5 \pm 4.2$	$36.4 \pm 13.5$	35 [90]

## 4.4 Measurements of buried films

We now discuss the required criteria for SSTR to measure the thermal conductivity of a buried film in a 4-layer system: metal transducer/thin film/buried film/substrate. Measurement of such a buried film is possible when the thermal resistance of this layer is much greater than those of the top thin film and substrate. This stems from the fact that for SSTR to measure the thermal conductivity of any layer in a multilayered material system, a significant steady-state temperature gradient must exist in that layer, either in cross-plane or in-plane direction. As the top thin film is in contact with the metal transducer, the temperature gradient of this layer is often large unless the film thickness is very low. On the other hand, since the substrate is a semi-infinite medium, a measurable temperature gradient exists in the substrate when large pump and probe radii are used. For a buried film, however, unless the thermal resistance is large, the resulting temperature gradient is relatively small compared to those of the thin film and substrate. Therefore, although SSTR probes through the buried film and is influenced by the thermal properties of this layer, the degree of such influence is relatively small. As a result, SSTR can not isolate the thermal conductivity of a buried film with low thermal resistance.

In addition, large pump and probe radii ( $> 10 \mu\text{m}$ ) are needed for buried film measurements. When the thermal resistance of the buried layer is much higher than those of thin film and substrate, bulk of the heat flows along the in-plane direction of the top thin film. For a sufficient thermal gradient to exist in the buried film, large spot sizes are required.

To experimentally show this, we have selected a sample that fits this criteria: 85 nm Al transducer/2.5  $\mu\text{m}$  Si film/1  $\mu\text{m}$  SiO<sub>2</sub> layer/Si substrate. The schematic and sensitivity calculation for this sample is shown in Figure 4.4. As exhibited here, SSTR can measure the thermal conductivity of buried SiO<sub>2</sub> layer when large spot sizes are used. However, such measurements are also sensitive to the in-plane thermal conductivity of the top Si film. TDTR is used to measure the cross-plane thermal conductivity of top Si film. The in-plane and cross-plane thermal conductivity of the 2.5  $\mu\text{m}$  Si film can be considered to the same [91]. Using  $1/e^2$  pump and probe radii of  $\sim 20$   $\mu\text{m}$ , we measure the buried SiO<sub>2</sub> film thermal conductivity to be  $1.34 \pm 0.26$  W m<sup>-1</sup> K<sup>-1</sup>. This value is in agreement with literature [86, 92], showing the capability of SSTR to measure the thermal conductivity of sub-surface buried layers.

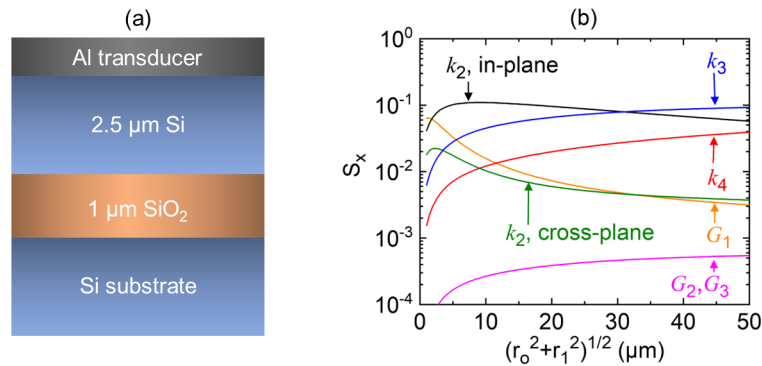


Figure 4.4: (a) Schematic diagram and (b) sensitivity calculation as a function of effective radius for the 4-layer sample: 85 nm Al transducer/2.5  $\mu\text{m}$  Si film/1  $\mu\text{m}$  SiO<sub>2</sub> layer/Si substrate.

## 4.5 Summary

We investigate the influences of multilayer material systems, thin metal film transducers, and thermal boundary conductances on the TPD of SSTR technique. The low modulation frequency of SSTR enables it to measure the thermal conductivity of buried substrates

that are traditionally challenging by TDTR and FDTR, demonstrated by presenting experimental data on three control samples. In addition, SSTR has the capability to isolate the thermal properties of a buried film as long as the thermal resistance of this layer is much higher than those of the top thin film and substrate. The works presented in this chapter marks an advancement in experimental metrology by establishing SSTR as a robust technique for thermal characterizations of sub-surface buried substrates and films.

## Chapter 5

# Investigating thermal transport in thermally conductive ultra-wide bandgap semiconductor films

This chapter focuses on investigating in-plane thermal transport in highly conductive AlN films with thicknesses ranging from 3.05 to 6  $\mu\text{m}$ . The works presented in this chapter have been published in *ACS Nano* [39].

### 5.1 Motivation

Thermal dissipation from hot-spots presents a bottleneck to the efficient and reliable operation of electronic devices, ranging from low-power logic devices to high-power RF high electron mobility transistors [93–99]. Different techniques, such as power management [100], improved packaging technology [98, 101], thermoelectric cooling [102], heat sink design [103, 104], and lateral heat spreaders [96, 97, 101] have been implemented to circumvent this problem. However, these solutions often require departure from the most efficient electronic device geometry to allow for gains in thermal dissipation. An ideal solution to this problem would be the development of high in-plane thermal conductivity

non-metallic materials that are able to easily remove heat from hot spots. These materials would also need to remain in thin film form to continue to allow current device architectures and form factors. To this end, high thermal conductivity crystals (e.g., diamond, cubic boron nitride, boron arsenide, aluminum nitride, and gallium nitride) and two-dimensional layered materials (e.g., graphene, and hexagonal boron nitride) have received significant attention in recent years [96, 105]. Thin films of these non-metallic materials can be implemented as heat spreaders when their thicknesses are larger than the hot-spot length scales [95, 96, 106, 107] in devices. This implementation also requires that the thin films have adequate length scales and crystal qualities to ensure bulk or near-bulk thermal conductivities. However, this is paradoxical, since defects and boundaries arising from thin film growth commonly result in much reduced thermal conductivities as compared to the respective bulk values. Among bulk solids, diamond has the highest thermal conductivity, above  $2000 \text{ W m}^{-1} \text{ K}^{-1}$  at room temperature [96, 108]. However, implementation of diamond thin films as heat spreaders have several limitations. For example, the thermal conductivities of diamond thin films are much lower than the bulk value due to microstructural features and defects during growth [109, 110]. Additionally, heterogeneous integration of materials onto diamond can lead to poor crystal quality due to lattice constant mismatch. Cubic boron arsenide, isotopically enriched cubic boron nitride and boron phosphide also have high thermal conductivity in bulk form [108, 111, 112]. Shrinking the length scales of these materials may lead to similar thermal conductivity reduction issues as diamond. Two-dimensional (2D) materials, on the other hand, have a small cross-sectional area in the in-plane direction by design. Therefore, in order to increase the thermal conductance and use them as efficient heat spreaders, the thickness of the 2D materials may need to be increased [96, 113]. Moreover, the thermal boundary conductance between 2D layers and substrates can be an additional crucial parameter that controls the heat spreading efficiency as it can reduce the effective thermal conductivity due to mode scattering and suppression [96].

Compared to the other III-V compound semiconductors, bulk, high-purity AlN crystals

have advantageous electronic properties, requisite transparency and higher thermal conductivity, making them suitable for use in optoelectronics, light-emitting diodes and high-power RF devices [14, 78, 83, 96, 114–119]. However, the use of AlN as heat spreaders in high-power electronic devices comes with the challenge of achieving high thermal conductivities in thin film forms. Recently, Koh *et al.* [71] reported bulk-like cross-plane thermal conductivities in high-quality AlN films with thicknesses ranging from 3 – 22  $\mu\text{m}$ . These promising results suggest that high-quality micrometer-thick films of AlN could act as heat spreaders in high-power devices depending on their in-plane transport properties.

While extensive literature exists on the cross-plane thermal conductivity of AlN [14, 120–128], reports on the in-plane thermal conductivity are almost non-existent. It is well known that in thin films, in-plane thermal transport is much less impacted by boundary scattering compared to cross-plane transport [129–131]. The intrinsic phonon thermal conductivity [14, 83, 114, 128, 132] of AlN suggests it may exhibit exceptional heat spreading characteristics and high in-plane thermal conductivity in its thin film form. Thus, measurement of the in-plane thermal conductivity of high-quality AlN thin films is paramount to realizing its potential as a radial heat sink. The SSTR technique provides an ideal platform to measure the in-plane thermal conductivity of such high-quality thin films.

## 5.2 Growth and characterization details

We study three AlN films with thicknesses of 3.05, 3.75, and 6  $\mu\text{m}$ . The films are grown on sapphire substrates via metal-organic chemical vapor deposition (MOCVD) [133, 134]. Scanning transmission electron microscopy reveals the existence of a nucleation layer near the AlN/sapphire interface in all samples. The thickness of the nucleation layer is less than 22% of the total film thickness [71]. The region above the nucleation layer is a single crystal AlN layer. This single crystal layer has low concentrations of silicon (Si), carbon (C), and oxygen (O) impurities, whereas the nucleation layer has relatively higher concentrations of these point-defects [71, 128]. The Al vacancy concentrations in the films are negligible

[128]. The dislocation density is on the order of  $10^8 \text{ cm}^{-2}$  in the single crystal layer and one to two orders of magnitude higher in the nucleation layer. The AlN films are grown by Dr. Asif Khan's group at the University of South Carolina. The characterizations are performed by Dr. Mark S. Goorsky's group at the University of California, Los Angeles.

### 5.3 Results and discussion

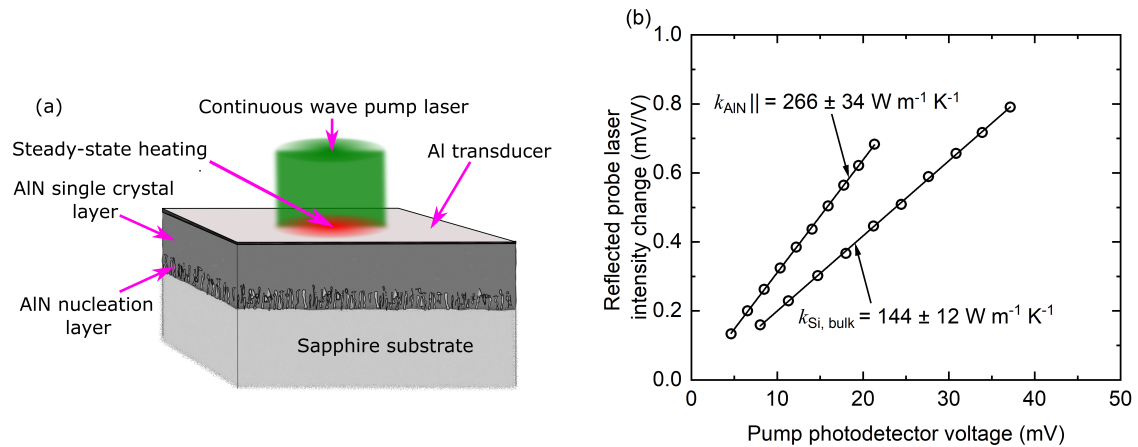


Figure 5.1: (a) Schematic of the AlN thin film samples: Al transducer/AlN film/sapphire substrate. (b) Reflected probe laser intensity change as a function of pump photodetector voltage for SSTR fitting of bulk Si and  $3.05 \mu\text{m}$  AlN film thermal conductivities.

A schematic of the AlN thin film samples is presented in Figure 5.1(a). Each sample consists of an Al transducer, an AlN thin film, and a sapphire substrate. The SSTR best fit curves for the thermal conductivity of bulk Si calibration sample and  $3.05 \mu\text{m}$  AlN thin film sample are shown in Figure 5.1(b). For bulk Si, SSTR measures the geometric mean of in-plane ( $k \parallel$ ) and cross-plane ( $k \perp$ ) thermal conductivity [7]. However, due to the radial heat spreading in the AlN thin films, SSTR measurements are much more strongly influenced by the in-plane thermal conductivity of the AlN films compared to the cross-plane.

Bulk Si is used as a calibration sample and its thermal conductivity is measured by both SSTR and TDTR from 120 – 400 K, as shown in Figure 5.2. At low temperatures, our TDTR-measured Si thermal conductivities are lower than the values reported in literature

for bulk Si [135]. A lower thermal conductivity of Si measured via TDTR has also been reported by Wilson and Cahill [136]. As discussed extensively in recent literature [136–138], TDTR and FDTR have failed to measure the thermal conductivity of Si at low temperatures due to obfuscations from thermal boundary resistances, nonequilibrium processes, and limiting heater length scales. Similar phenomena have also been reported for several other high thermal conductivity crystals and thick alloys [73, 84, 136–141]. We note that though TDTR fails for Si and several other crystals, the thermal conductivity of sapphire and AlN can be accurately measured by TDTR at low temperatures [71, 128, 142]. The nature of such material specific failure of TDTR is an active area of research [84, 136] and beyond the scope of this work. However, due to the measurement time and length scales, SSTR measurements are less sensitive to the above-mentioned limitations. As a result, SSTR can accurately measure the intrinsic, bulk thermal conductivity of Si as evident in Figure 5.2. Within uncertainty, the Si thermal conductivities measured by SSTR are in

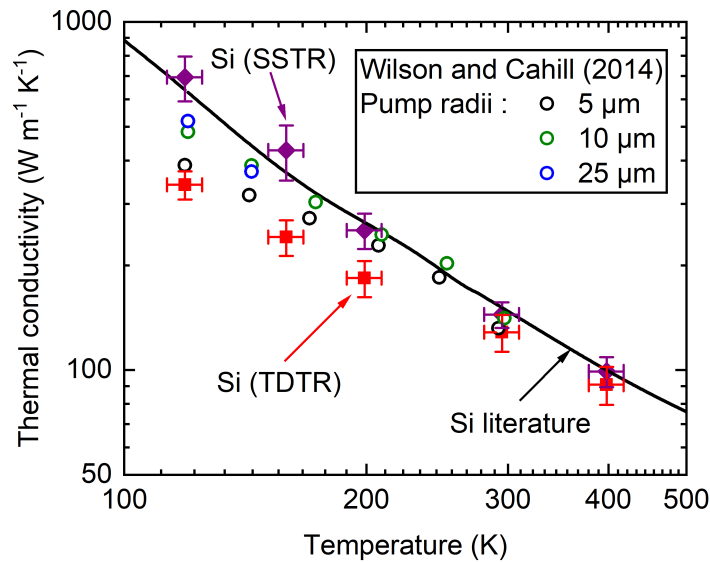


Figure 5.2: Calibration of SSTR technique via bulk Si wafer thermal conductivity measurements. Within uncertainty, the SSTR measurements of Si (filled diamonds) are in agreement with literature Si values [135] (solid line) and higher than our TDTR measurements of Si (filled squares). TDTR-measured Si thermal conductivities being lower than literature have also been reported by Wilson and Cahill [136] (open circles) when using  $1/e^2$  pump radii of 5, 10, and 25  $\mu\text{m}$ . For comparison, the  $1/e^2$  pump radii of our TDTR and SSTR measurements are  $\sim 8.5$  and 10  $\mu\text{m}$ , respectively.

good agreement with previous literature [135]. The small deviations observed in SSTR measurements from the values reported in literature can be attributed to the uncertainty associated with temperature and other experimental variables.

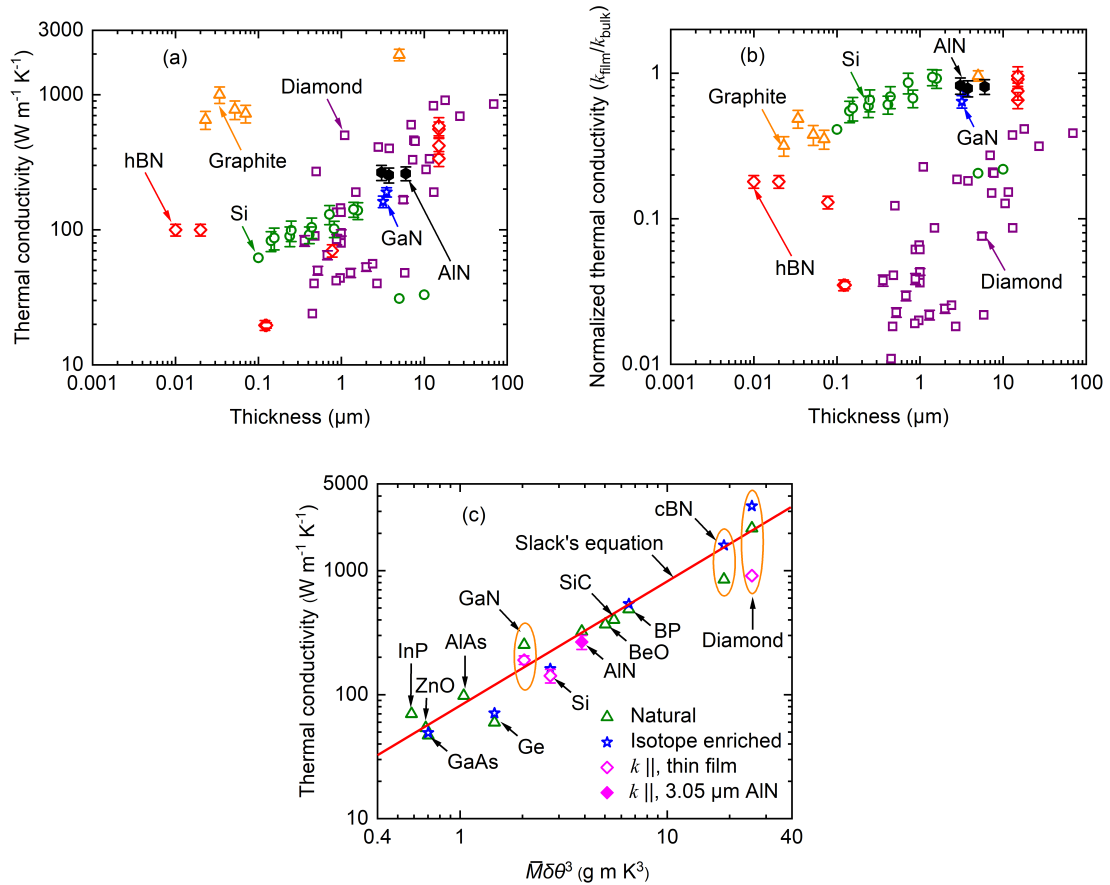


Figure 5.3: (a) In-plane thermal conductivity as a function of film thickness for different high thermal conductivity materials. The hollow symbols are taken from literature [81, 109, 143–159]. (b) Normalized in-plane thermal conductivity ( $k_{\text{film}}/k_{\text{bulk}}$ ) of the films presented in panel a as a function of thickness. (c) The thermal conductivity of natural and isotope enriched adamantine crystals as a function of the Leibfried-Schomann scaling parameter. The solid line indicates Slack's equation for adamantine crystals [14, 105, 114, 160]. The values of the Leibfried-Schomann scaling parameter and thermal conductivity of the crystals are taken from literature [14, 16, 71, 105, 108, 108, 112, 114, 161–168]. For comparison, the highest reported in-plane thermal conductivities [81, 109, 152] of thin films of the adamantine crystals are also included.

The room temperature in-plane thermal conductivity as a function of film thickness for different high thermal conductivity materials are presented in Figure 5.3(a). As shown here, the in-plane thermal conductivities of the three AIN thin films are nearly the same,

$\sim 260 \pm 40 \text{ W m}^{-1} \text{ K}^{-1}$ . For reference, the intrinsic thermal conductivity of bulk, defect-free, single crystal AlN predicted by Slack *et al.* [14] and Lindsay *et al.* [83] are  $\sim 319$  and  $322 \text{ W m}^{-1} \text{ K}^{-1}$ , respectively. As the defect concentrations are very low in the top single crystal layer of the AlN thin films, the thermal conductivity of this layer is in close agreement with the theoretical predictions [14, 71, 83]. The nucleation layer, on the other hand, possesses a low thermal conductivity due to the presence of relatively higher point- and line-defect concentrations [71]. With the spot sizes used here ( $1/e^2$  radii  $\sim 10 \text{ }\mu\text{m}$ ), SSTR probes through both layers of the AlN thin films. Thus, SSTR measurements represent a thermal conductivity that is influenced by both single crystal and nucleation layers. As a result, the SSTR-measured in-plane thermal conductivities of the AlN thin films are slightly lower than the predictions of Slack *et al.* [14] and Lindsay *et al.* [83]. From Figure 5.3(a), it is evident that compared to their thicknesses ( $6 \text{ }\mu\text{m}$  or less), these AlN films have one of the highest in-plane thermal conductivities of any thin film material, surpassed only by graphite and diamond. The deposition technique, microstructure, grain size, and defect concentrations highly influence the thermal conductivity values of thin film materials [81, 110, 149, 151, 155, 157, 158]. Due to this, bulk of the prior reports on the in-plane thermal conductivity of diamond, GaN, and hexagonal boron nitride (hBN) thin films with thicknesses on the order of  $6 \text{ }\mu\text{m}$  or less are lower than  $200 \text{ W m}^{-1} \text{ K}^{-1}$ .

In Figure 5.3(b), we have plotted the normalized in-plane thermal conductivity of various thin film materials with respect to their bulk in-plane values. This figure reveals that the AlN films have one of the highest normalized in-plane thermal conductivities, higher than nearly all graphite and diamond thin films. This indicates that the thermal conductivity reduction due to defect and boundary scattering is much less severe in our AlN thin films compared to the vast majority of the graphite and diamond films reported in literature.

In Figure 5.3(c), we present predictions of Slack's equation for the thermal conductivity of adamantane crystals as a function of the Liebfried-Schlomann scaling parameter,  $\overline{M}\delta\theta^3$  (where  $\overline{M}$  is the average atomic mass,  $\delta^3$  is the average atomic volume, and  $\theta$  is the Debye temperature) [14, 105, 114, 160]. For comparison, the highest reported room temperature

in-plane thermal conductivities of thin films of the adamantine crystals are also included. Slack's equation has been very successful in predicting the highest achievable thermal conductivity of nearly all the adamantine crystals at room temperature [105]. The in-plane thermal conductivity of the 3.05  $\mu\text{m}$  AlN thin film is very close to the prediction of Slack's equation. This indicates that the thermal conductivities of the AlN thin films are very close to the maximum achievable value for AlN. Figure 5.3(c) provides a testament to the high quality of the AlN thin films.

Figure 5.4(a) shows the SSTR-measured in-plane thermal conductivity of the 3.05  $\mu\text{m}$  AlN thin film from 120 – 400 K. For comparison, the cross-plane thermal conductivities of a commercial  $\sim 500$   $\mu\text{m}$  AlN wafer [128], and bulk, high-purity, single crystal AlN [14] are also shown. We also include the first-principles calculations of the in-plane phonon thermal conductivity of isotopically pure AlN from Lindsay *et al.* [83] Due to the presence of the nucleation layer, the thermal conductivity of the 3.05  $\mu\text{m}$  thin film is lower than bulk AlN, and predictions of Lindsay *et al.* [83] at nearly all temperatures. As temperature decreases, the in-plane thermal conductivity of the 3.05  $\mu\text{m}$  film increases. This indicates that the thermal conductivity of the 3.05  $\mu\text{m}$  AlN film is mostly driven by intrinsic phonon-phonon scattering, with a lesser influence from phonon-defect scattering.

At low temperatures, the in-plane thermal conductivity of the 3.05  $\mu\text{m}$  AlN thin film is higher than the cross-plane thermal conductivity of the commercial  $\sim 500$   $\mu\text{m}$  AlN wafer. This can be attributed to the presence of large concentrations of Al vacancy in the commercial wafer [128]. Among different types of phonon-defect scattering, Al vacancy-phonon scattering plays the dominant role in AlN thermal conductivity reduction [127]. The Al vacancy concentrations in the films used in this work are negligible [128]. On the other hand, the Al vacancy concentration in the commercial AlN wafer is  $\sim 3 \times 10^{19} \text{ cm}^{-3}$  [128]. Near room temperature, as phonon-phonon scattering is the dominant scattering mechanism, the thermal conductivities of the 3.05  $\mu\text{m}$  film and 500  $\mu\text{m}$  commercial wafer are in agreement. However, at low temperatures, the thermal conductivity of the wafer is lower compared to that of the 3.05  $\mu\text{m}$  film due to the dominance of phonon-vacancy scattering over phonon-

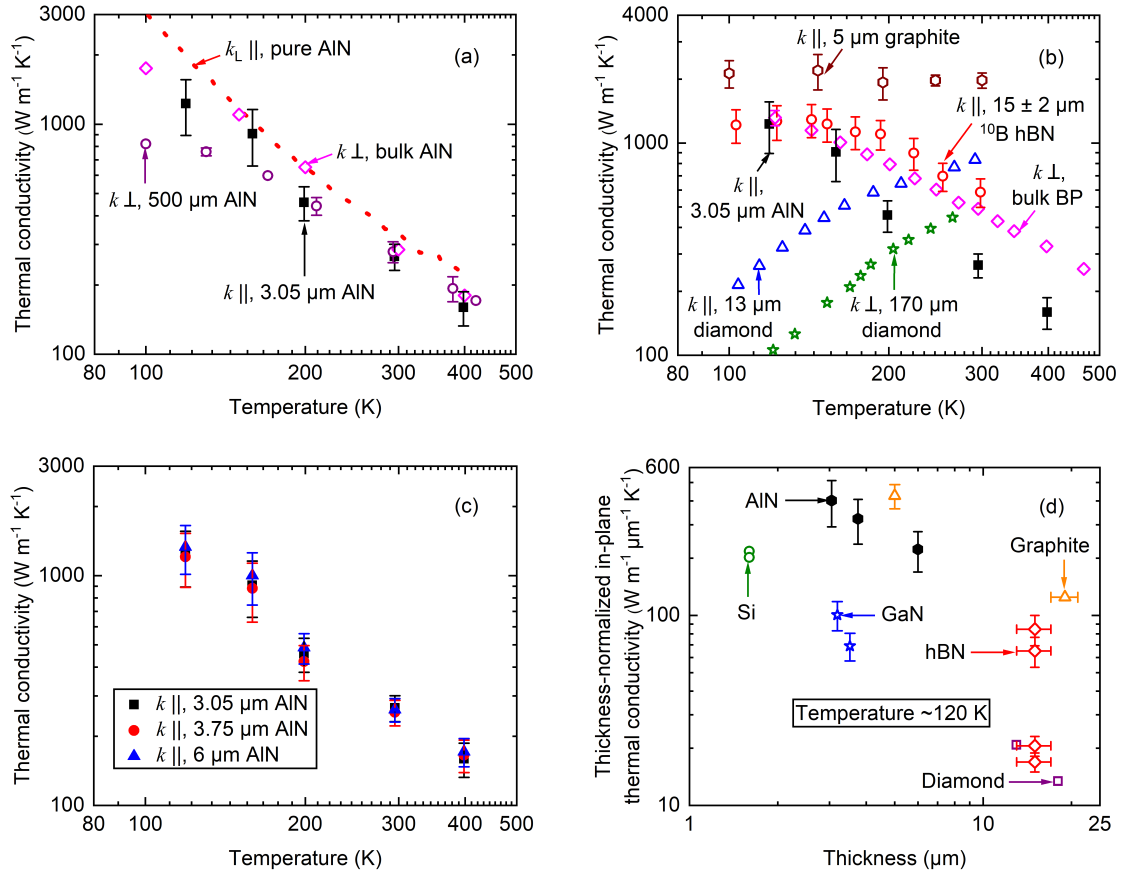


Figure 5.4: (a) Temperature-dependent in-plane thermal conductivity of the 3.05  $\mu\text{m}$  AlN film. For comparison, cross-plane thermal conductivities of a commercial  $\sim 500$   $\mu\text{m}$  AlN wafer [128], and bulk, high-purity, single crystal AlN [14] are also included. The dotted line represents the first-principles calculations of in-plane lattice thermal conductivity of isotopically pure bulk AlN [83]. (b) Temperature-dependent in-plane and cross-plane thermal conductivities of several high thermal conductivity materials: 3.05  $\mu\text{m}$  AlN film, 13  $\mu\text{m}$  diamond film [109], 170  $\mu\text{m}$  isotopically enriched diamond film [110], 5  $\mu\text{m}$  highly oriented pyrolytic graphite film [156],  $15 \pm 2$   $\mu\text{m}$  thick isotopically enriched  $^{10}\text{B}$  hBN film [159], and bulk boron phosphide (BP) [108]. (c) Temperature-dependent in-plane thermal conductivities of the 3.05, 3.75, and 6  $\mu\text{m}$  AlN thin films. (d) Thickness-normalized in-plane thermal conductivity of micrometer-thick films of high thermal conductivity materials at  $\sim 120$  K. The materials include AlN, diamond [109], Si [152], graphite [156, 169], GaN [81], and hBN [159]. In Figures a-d, filled symbols represent measurements taken in this work, and open symbols represent literature values.

phonon scattering.

In Figure 5.4(b), the temperature-dependent in-plane thermal conductivities of the 3.05  $\mu\text{m}$  AlN thin film, a 13  $\mu\text{m}$  diamond film [109], a 5  $\mu\text{m}$  graphite film [156], and a  $15 \pm$

2  $\mu\text{m}$  99% isotopically enriched  $^{10}\text{B}$  hBN film [159] are presented. The cross-plane thermal conductivities of a 170  $\mu\text{m}$  isotopically enriched diamond film [110], and bulk boron phosphide (BP) [108] are also shown here. The graphite, diamond, and  $^{10}\text{B}$  hBN films as well as bulk BP have much higher thermal conductivities than the 3.05  $\mu\text{m}$  AlN thin film at room temperature. However, the thermal conductivity of the graphite film remains nearly constant with decreasing temperature because of phonon scattering at the grain boundaries [156]. Similarly, due to phonon-boundary and phonon-defect scattering, the thermal conductivities of the polycrystalline diamond films decrease with a reduction in temperature [109, 110]. Contrary to these films, the thermal transport mechanisms in our AlN thin films are primarily driven by phonon-phonon scattering. As a result, at low temperatures, the in-plane thermal conductivity of the AlN film surpasses those of the diamond films and becomes much closer to that of the graphite film. As the temperature decreases, the thermal conductivities of the 3.05  $\mu\text{m}$  AlN thin film,  $^{10}\text{B}$  hBN, and BP start to converge. This convergence can be attributed to the influence of extrinsic scattering on the thermal conductivities of  $^{10}\text{B}$  hBN film, and bulk BP. At low temperatures, phonon scattering by the sub-grain boundaries, dislocations, and point-defects influence the thermal conductivity of the  $^{10}\text{B}$  hBN film [159]. Similarly, the thermal conductivity of bulk BP is also impacted by point-defect and isotope scattering as well as other experimental variables [108]. Thus, at 120 K, the in-plane thermal conductivity of the 3.05  $\mu\text{m}$  AlN film becomes comparable to  $^{10}\text{B}$  hBN and BP thermal conductivities.

In Figure 5.4(c), we have plotted the temperature-dependent in-plane thermal conductivities of the 3.05, 3.75, and 6  $\mu\text{m}$  AlN thin films. The thermal conductivities of the three films are in excellent agreement with each other. This indicates that boundary scattering is not significantly impacting the in-plane thermal conductivities of these AlN thin films at any temperature. This further supports that the in-plane thermal conductivities of our AlN films are driven by intrinsic phonon-phonon scattering events, leading to an increase in thermal conductivity as temperature decreases. This is contrary to the behavior commonly observed in traditional thin film materials.

In Figure 5.4(d), the thickness-normalized in-plane thermal conductivity of micrometer-thick diamond [109], Si [152], graphite [156, 169], GaN [81], hBN [159], and AlN films at  $\sim 120$  K are presented. These results show that along with graphite, the AlN films examined in this study possess the highest thickness-normalized in-plane thermal conductivity reported to date. Figure 5.4(d) provides evidence that at 120 K, only graphite possesses higher thermal conductivity than the AlN films among all thin film materials of micrometer length scale. These exceptionally high in-plane thermal conductivities of the AlN films at low temperatures are consequences of in-plane heat transport mechanism being driven by phonon-phonon scattering, and not being significantly restricted by boundary and defect scattering.

In Figure 5.5(a), we have plotted the in-plane and cross-plane thermal conductivities of the  $3.05 \mu\text{m}$  thin film as a function of temperature. The in-plane and cross-plane thermal conductivities are measured by SSTR and TDTR, respectively. Above 160 K, the in-plane and cross-plane thermal conductivities are nearly the same. Below this temperature, however, the cross-plane thermal conductivity decreases compared to that of in-plane, leading to a pronounced anisotropy. To conclusively show this anisotropy, we extend the temperature-dependent measurements to 105 K. The observed anisotropy can not be explained from the AlN crystal structure as that would lead to the in-plane thermal conductivity being  $\sim 10 - 14\%$  higher than the cross-plane thermal conductivity at low temperatures [83]. This anisotropy is also not due to the failure of TDTR technique as TDTR has been shown to measure AlN thermal conductivity accurately down to 80 K [71]. To explain this anisotropy, we review the thermal transport mechanisms along the in-plane and cross-plane directions of the  $3.05 \mu\text{m}$  AlN film. For simplicity, we have considered an interface to exist between the single crystal and nucleation layer. The resistance at this interface represents the equivalent resistance from point- and line-defect scattering at the nucleation layer starting region.

As conceptually illustrated in Figure 5.5(b), in the single crystal layer, the phonons carrying heat in the in-plane direction travel relatively uninterrupted, whereas the phonons car-

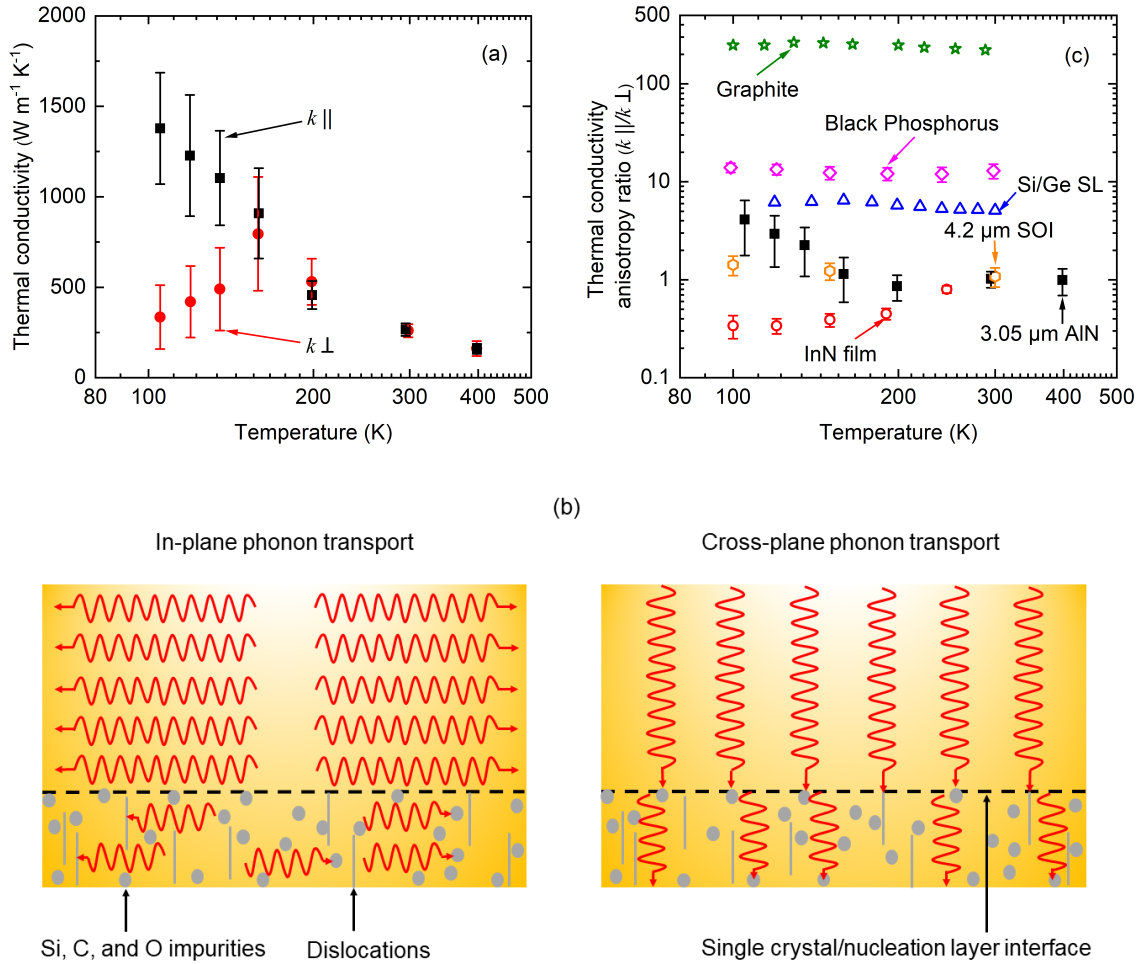


Figure 5.5: (a) Temperature-dependent in-plane and cross-plane thermal conductivities of the 3.05 μm AlN thin film. (b) Phonon heat transport mechanisms along the in-plane and cross-plane directions of the 3.05 μm film. The top layer is single crystal AlN and the bottom layer is nucleation region with high Si, C, and O impurities, and dislocation density. (c) Thermal conductivity anisotropy ratios ( $k_{||}/k_{\perp}$ ) as a function of temperature for the 3.05 μm AlN film, graphite [170], black phosphorus (in-plane thermal conductivity is taken along the zigzag direction) [171], 4.2 μm Si on insulator (SOI) [172, 173], Si/Ge superlattice [174], and InN film (dislocation density  $1.1 \times 10^{10} \text{ cm}^{-2}$ ) [175]. In panels a and c, filled symbols represent measurements taken in this study, and open symbols represent literature values.

rying heat in cross-plane direction scatter at single crystal/nucleation layer interface. This is supported by the fact that interface scattering is more dominant in cross-plane transport compared to in-plane [129, 171, 174–177]. At low temperatures, phonon-phonon scatter-

ing rates decrease and the thermal transport shifts to lower frequency phonons relative to that of room temperature. While carrying heat in the cross-plane direction, the majority of these low frequency, long wavelength phonons scatter at the single crystal/nucleation layer interface. This leads to a significant decrease in the cross-plane thermal conductivity of the single crystal layer. For the phonons carrying heat in the in-plane direction, the scattering at the single crystal/nucleation layer interface, and subsequent thermal conductivity reduction is much smaller. As a result, in the single crystal AlN layer, there is a large anisotropy in thermal conductivity at low temperatures. With increasing temperature, thermal transport shifts to high frequency phonons and phonon-phonon scattering becomes stronger. As a result, the anisotropy in the single crystal layer reduces.

The nucleation layer has a lower thermal conductivity than the single crystal layer as it contains higher concentrations of point-defects and dislocations. The point-defects scatter cross-plane and in-plane travelling phonons homogeneously [178–180]. The small thickness of the nucleation layer ( $\sim 0.6 \mu\text{m}$ ) has a more pronounced impact on the cross-plane travelling phonons compared to the in-plane [127, 129, 130]. On the contrary, the vertically oriented dislocation line-defects have a stronger influence on the in-plane phonon transport [128, 179] although this effect is likely not very large [81]. Due to a combination of these scattering, the thermal conductivity of the nucleation layer can be expected to remain near isotropic across all temperatures of interest in this study. TDTR and SSTR probe through both layers of the  $3.05 \mu\text{m}$  AlN thin film [7, 40, 41, 73, 138]. Because of the previously discussed pronounced anisotropy in the single crystal layer, the cross-plane thermal conductivity of the  $3.05 \mu\text{m}$  thin film is much lower compared to the in-plane below 160 K.

In Figure 5.5(c), we have plotted the thermal conductivity anisotropy ratios (the ratio of in-plane to cross-plane thermal conductivity) of graphite [170], black phosphorus [171],  $4.2 \mu\text{m}$  silicon on insulator (SOI) [172, 173], a Si/Ge superlattice [174], an InN film [175], and our  $3.05 \mu\text{m}$  AlN film as a function of temperature. For materials with anisotropic crystal structures such as graphite and black phosphorus, the in-plane and cross-plane thermal conductivities are dictated by the same phonon scattering mechanisms across the tempera-

ture range, thus, the anisotropy ratios are nearly temperature independent [171, 175]. For the Si/Ge superlattice and 4.2  $\mu\text{m}$  SOI, the anisotropy ratios decrease with increasing temperature as phonon-phonon scattering becomes stronger and phonon-interface scattering becomes less dominant [174, 175, 181]. A similar trend is observed in the 3.05  $\mu\text{m}$  AlN film. It is to be noted that in the Si/Ge superlattice and 4.2  $\mu\text{m}$  SOI, phonon-interface scattering originates at a physical interface. However, in the 3.05  $\mu\text{m}$  AlN film, the single crystal/nucleation layer interface is a representation of phonon scattering by point- and line-defects at the nucleation layer starting region. Similar to the 3.05  $\mu\text{m}$  AlN film, highly temperature-dependent anisotropy ratios induced by crystalline defects have been observed in InN films [175]. In our work, anisotropy is observed only at low temperatures. However, we posit that this anisotropy will become more pronounced and be observed even at room temperature if the AlN film thickness is reduced to sub-micrometer levels [81, 127]. In sub-micrometer thick AlN films, the nucleation layer can be expected to occupy a greater percentage ( $> 22\%$ ) of the total film thickness [71], thereby significantly limiting the ability of phonons to carry heat in the cross-plane direction. Such crystalline defect-induced anisotropy without any modification in crystal structure can provide guidelines for directed heat dissipation [175] and therefore, has important implications in usage of AlN films for thermal management of high-power devices.

## 5.4 Summary

We report on the high in-plane thermal conductivities of AlN thin films on sapphire substrates. Using SSTR, we measure the in-plane thermal conductivities of the AlN films to range from  $\sim 260 \pm 40 \text{ W m}^{-1} \text{ K}^{-1}$  to  $\sim 1200 \pm 300 \text{ W m}^{-1} \text{ K}^{-1}$  as temperature decreases from 295 K to 120 K, respectively. At room temperature, the in-plane thermal conductivities of the AlN films are significantly less impacted by defect and boundary scattering as compared to the majority of the graphite and diamond thin films reported in literature. At low temperatures, the in-plane thermal conductivities of the AlN films are equivalent

to boron phosphide and isotopically enriched hexagonal boron nitride, and much higher than diamond thin films. These exceptionally high in-plane thermal conductivities of our AlN films are consequences of in-plane thermal transport being driven by phonon-phonon scattering. This leads to an increase in thermal conductivity with a reduction in temperature. This trend is opposite of what is observed in other traditionally studied high thermal conductivity thin films, where boundaries and defects arising from film growth lead to a thermal conductivity reduction with decreasing temperature. As a result, at 120 K, the in-plane thermal conductivities of our AlN films are second-highest only to graphite among all thin film materials of equivalent thicknesses measured to date, quantified via the thickness normalized in-plane thermal conductivity. Moreover, defect scattering causes a large temperature-dependent anisotropy ratio in the 3.05  $\mu\text{m}$  AlN film. These AlN films with high in-plane thermal conductivities offer a viable solution to the thermal management issue of electronic devices.

## Chapter 6

# Investigating thermal transport in insulating polymer films

In this chapter, I use SSTR to investigate the cross-plane thermal transport in organic-inorganic hybrid polymer films with thicknesses ranging from 1.4 to 120 nm. The works presented in this chapter are currently under preparation for a journal submission.

### 6.1 Motivation

When a thin film thickness is on the order of 50 nm or less, directly measuring the intrinsic thermal conductivity is challenging via thermoreflectance techniques [182]. In such cases, the parameter of interest is usually the thermal resistance [183], which incorporates the interfacial resistances across the transducer/thin film and thin film/substrate as well as the resistance of the film itself. SSTR's large TPD and insensitivity to heat capacity makes it an ideal technique for such measurements. To experimentally show this, I make a series of measurements on organic-inorganic hybrid metalcone (alucone and tincone) films in this chapter. The hybrid polymer films are grown on Si substrates via molecular layer deposition (MLD) [184]. MLD-grown metalcone films have received significant attention in recent years as a suitable coating material for organic light emitting diodes [185], lithium

and sodium ion batteries [186, 187]. Use of metalcone in these devices has resulted in improved lifetimes and stability. However, the thermal properties of metalcone films have not been previously studied. Therefore, to optimize the device efficiency, proper characterizations of thermal properties are of vital interest.

## 6.2 Growth details

The metalcone films are deposited using various organic precursor combinations. Tincone is deposited from tetrakis tin and ethylene glycol. Alucone is deposited from trimethylaluminum and ethylene glycol. Each precursor is handled only in nitrogen-ambient before being installed on the MLD reactor. Precursors are heated as follows to achieve sufficient vapor pressure for deposition: tetrakis tin to 65 °C, trimethylaluminum to room temperature, ethylene glycol to 70 °C for tincone and 80 °C for alucone. The Si substrates are cleaned in a piranha solution of 1:1 volume ratio  $\text{H}_2\text{O}_2:\text{H}_2\text{SO}_2$  for 15 minutes before use. The structures of alucone and tincone films are shown in Figure 6.1. The thicknesses of the films range from 1.4 to 120 nm. The metalcone films are grown by Dr. Gregory Parsons' group at North Carolina State University.

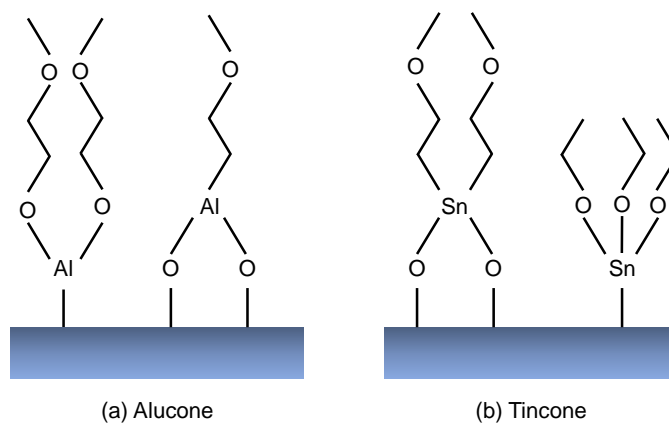


Figure 6.1: Structures of the (a) alucone and (b) tincone films.

### 6.3 Results and discussion

Figure 6.2(a) shows a schematic diagram of the metalcone sample geometry. As the film thickness ( $L$ ) is on the order of 50 nm or less, we measure the thermal resistance ( $R$ ) across the geometry via SSTR. This thermal resistance can be expressed using the following series resistor model [188]:

$$R = \left(\frac{1}{G}\right)_{Al/film} + \left(\frac{L}{\kappa}\right)_{film} + \left(\frac{1}{G}\right)_{film/Si}. \quad (6.1)$$

Figure 6.2(b) shows the measured thermal resistances as a function of metalcone film thickness. As exhibited here, the thermal resistance increases with film thickness. This is an indicator of diffusive thermal transport in the films. For such cases, the intrinsic thermal conductivity can be extracted from a linear fit to the thermal resistance as a function of film thickness. Here, the inverse of the slope  $(\Delta R/\Delta L)^{-1}$  provides the intrinsic thermal conductivity of the films. Using this methodology, we determine the intrinsic thermal conductivity of alucone and tincone to be  $1.14 \pm 0.18$  and  $0.43 \pm 0.07 \text{ W m}^{-1} \text{ K}^{-1}$ , respectively. The thermal conductivity difference between the two polymers likely stems from the different atomic masses of the metals [112].

We further measure the longitudinal sound speed of an alucone and tincone film via picosecond acoustics as shown in Figure 6.2(c). The longitudinal sound speed of the two polymers are  $6288 \pm 324$  and  $4080 \pm 297 \text{ m s}^{-1}$ , respectively. As sound speed is an indicator of bond strength [53], our measurements show that the bond strength is different between the two polymers.

In 6.2(d), we plot the thermal conductivity as a function of longitudinal sound speed for a wide range of polymers. As shown here, by changing the metal, the thermal and acoustic properties of the metalcone films can be tuned to cover a large span.

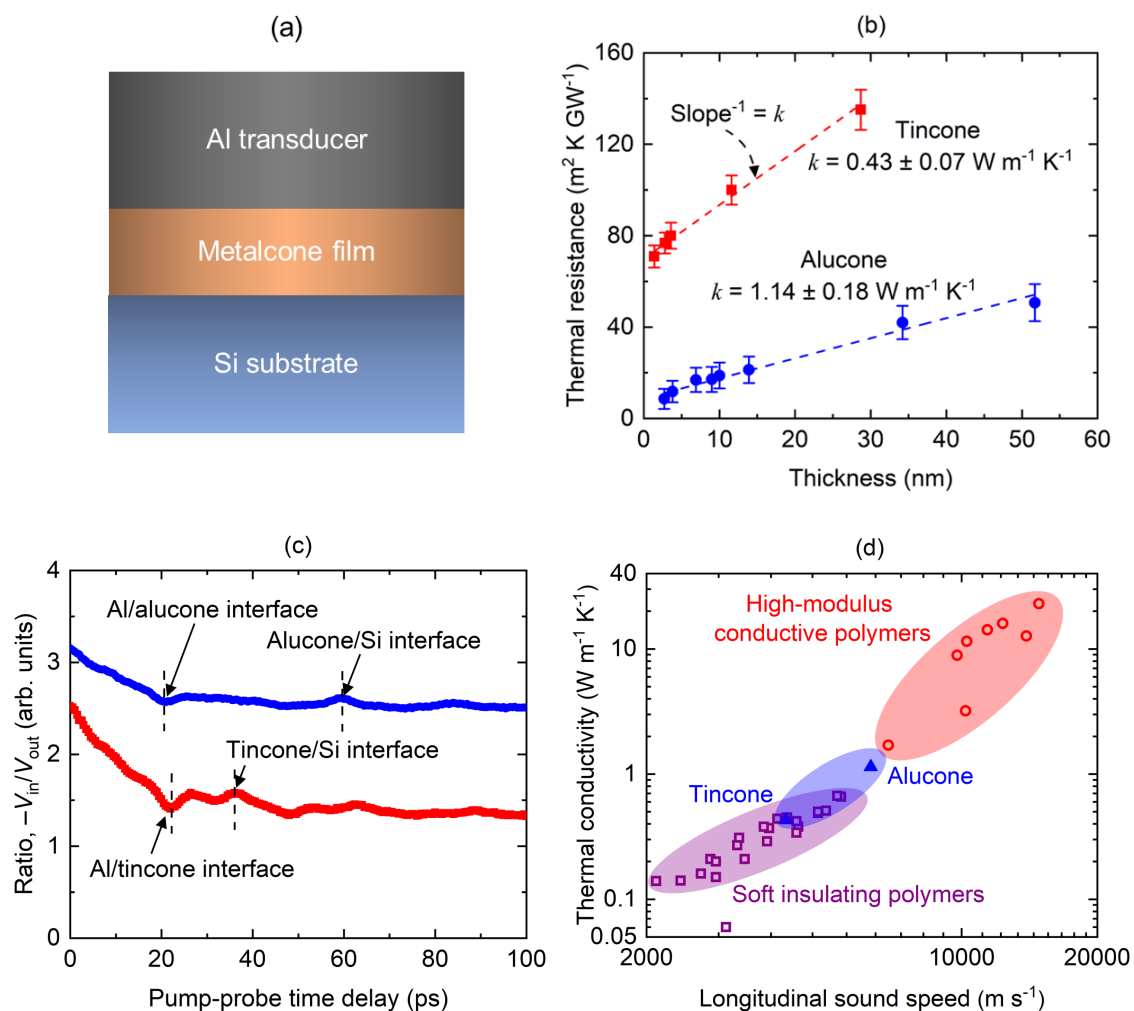


Figure 6.2: (a) Schematic diagram of the sample geometry. (b) Thermal resistance as a function of alucone and tincone film thickness. (c) Picosecond acoustic response of TDTR measurements for a 120 and 28.7 nm alucone and tincone film, respectively. (d) Thermal conductivity vs longitudinal sound speed for a wide range of polymers. The data for the soft insulating polymers and high-modulus conductive polymers (hollow symbols) are taken from Refs [189–191].

## 6.4 Summary

We study the thermal and acoustic properties of two hybrid metalcone (alucone and tincone) films grown via MLD technique. The higher atomic mass of tin compared to aluminum gives rise to a thermal conductivity difference between the two polymers. The longitudinal sound speed, hence the bond strength is also different between the two polymers. The works presented in this chapter opens up pathways for tuning the thermal and acoustic properties of a hybrid metalcone polymer by changing the metal.

## Chapter 7

# Measuring thermal resistance of multilayered geometries

In this chapter, I use SSTR to measure the thermal resistance of challenging multilayered geometries and validate TDTR measurements. The works presented in this chapter have been published in *Acta Materialia* [192].

### 7.1 Motivation

The industrial devices used in electronic applications often consist of four to five layers [96]. Measuring the thermal conductivity of a single layer in such geometry requires proper knowledge of the other layers and interfaces. TDTR and FDTR usually fulfill this requirement by assuming the thermal properties of the other layers and interfaces from literature [78, 80]. However, as the thermal properties of a layer or interface highly depends on deposition technique and microstructure [81, 157, 158], assuming accurate values from the literature can be challenging. Using large spot sizes, SSTR can measure the thermal resistance of the entire multilayered geometries without specific knowledge of the layers and interfaces and therefore, provides a pathway to validate any measurements made by TDTR or FDTR.

To demonstrate this capability of SSTR, I use a series of samples of the following geometry:  $\sim 80$  nm Al transducer/200 nm copper-tungsten (Cu/W) nanomultilayer/25 nm tungsten (W)/90 nm of silicon nitride ( $\text{Si}_3\text{N}_4$ )/Si substrate. Such nanomultilayers (NMLs) are widely used in interconnect systems due to their scalability, longstanding fabrication infrastructures, and low-cost [193]. While TDTR can measure the thermal conductivity of the Cu/W NMLs assuming the thermal properties of other layers and interfaces, SSTR provides a mean to validate these assumptions.

## 7.2 Growth and characterization details

The Cu/W NMLs are grown by DC magnetron sputtering in an ultra-high vacuum (UHV) chamber with a base pressure of  $< 5 \times 10^{-9}$  mbar. The multilayers are grown on Si substrates that have 90 nm of a- $\text{Si}_3\text{N}_4$  on top. This a- $\text{Si}_3\text{N}_4$  layer prevents interdiffusion between the Si substrate and Cu/W NML during the high-temperature annealing, which can result in the unwanted formation of Si-Cu intermetallics. Prior to the deposition, an RF bias of 100 V at  $1.6 \times 10^{-2}$  mbar is applied for 2 min to remove residual surface contaminants after ultrasonic cleaning in acetone, ethanol, and isopropanol. 10 nm of Cu and 10 nm of W repeated 10 times are grown on a 25 nm W layer working as a buffer. The Ar pressure and gun power are optimized to tune the NML stress to compressive and tensile values. After the deposition, selected samples undergo an isothermal annealing process for 100 min at 300 °C, 600 °C, 800 °C, or 850 °C in high vacuum (pressure  $< 10^{-5}$  mbar) with a heating ramp of 20 K/min in a CVE (Cambridge Vacuum Engineering) HL 1218 oven.

The microstructure of the Cu/W NMLs are characterized via scanning transmission electron microscopy (STEM), energy dispersive X-ray spectroscopy (EDS), X-ray diffraction analysis (XRD), and scanning electron microscopy (SEM). Figure 7.1 shows cross-sectional STEM images of the tensile and compressive NML overlaid with the corresponding EDS maps. The Cu and W nanolayers are straight and planar in the bottom of the NML stacks, but roughen towards the NML surface. The individual W layer thicknesses

are rather constant and very similar for the compressive and tensile NML stacks. On the contrary, the thicknesses of the individual Cu layers appear less homogeneous and less constant throughout the stack for the tensile NML. The contrast in the MAADF-STEM images indicates that the tensile NML has a smaller grain size as compared to the compressive NML.

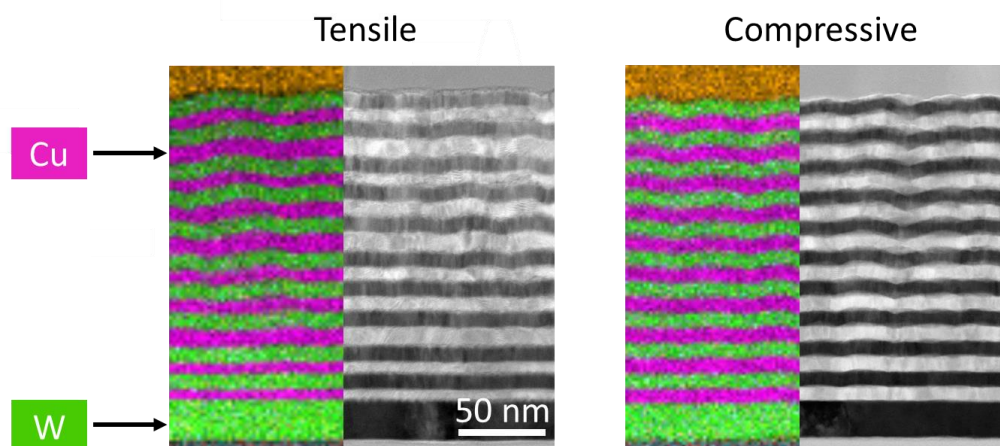


Figure 7.1: Cross-sectional MAADF-STEM images of the tensile and compressive NMLs (greyscale) showing diffraction contrast and overlaid EDS elemental mapping of Cu and W (colors).

XRD characterization reveals that the interfacial roughness is more than 3 times higher in the tensile NML compared to the compressive one. Additionally, the disorder within the W layers is 3 times higher in the tensile NML, whereas the Cu layer disorder is comparable for the two cases.

The cross-sectional SEM analyses of the as-deposited and annealed NMLs are shown in Figure 7.2. The atomic disorder of the tensile NML appears to be reduced after annealing in the range from 300 °C to 600 °C, whereas such an effect is not discernible by SEM for the compressive NML. At 800 °C, a striking difference in thermal stability between the tensile and compressive NML becomes evident: while the tensile NML has completely transformed into a nanocomposite (NC), the compressive NML is still in the first stage of NML degradation. A compressive NML sample is also annealed at an even higher temper-

ature of 850 °C, revealing that the NML-to-NC transformation process is still ongoing and has only partially completed.

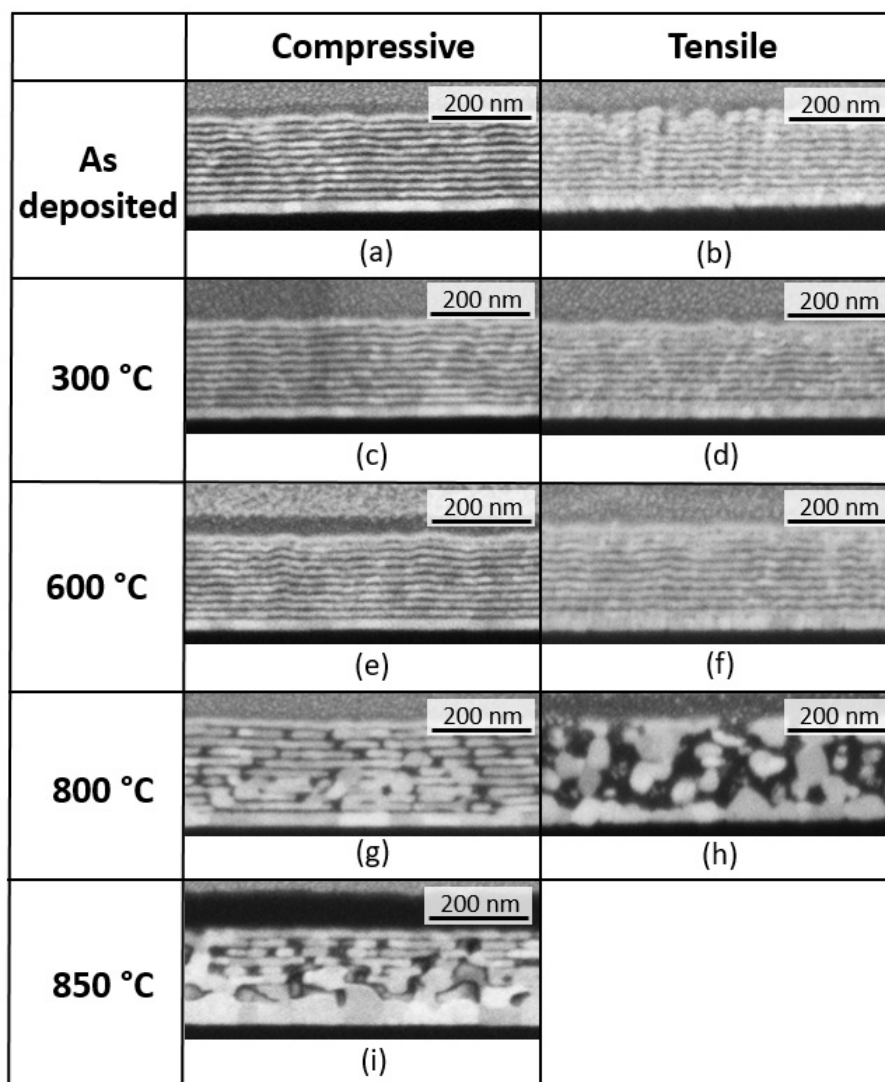


Figure 7.2: SEM images of cross sections of as-deposited and annealed NMLs. Bright regions in the NML/NC are associated to W; dark regions to Cu.

The growth and characterizations of the Cu/W NMLs are done by Dr. Claudia Cancellieri's group at Swiss Federal Laboratories for Materials Science and Technology. Dr. Eric R. Hoglund from the University of Virginia also contributed to the characterizations.

### 7.3 Results and discussion

TDTR is applied to investigate the effects of the intrinsic stress state and annealing temperature on the cross-plane thermal conductivity of Cu/W NMLs. A schematic diagram of the entire sample geometry is presented in Figure 7.3. A total of seven resistances between the Al transducer and Si substrate are implemented for the TDTR data analysis. TDTR can measure the top two resistances as long as the other five are known. To determine the thermal resistance of the  $\text{Si}_3\text{N}_4$  layer, we measure the thermal conductivity of a  $\sim 90$  nm  $\text{Si}_3\text{N}_4$  film via TDTR. The thermal resistance of the 25 nm W layer is adopted from literature [193–195]. Furthermore, we assume that the intrinsic thermal resistances of the Cu/W NML, W, and  $\text{Si}_3\text{N}_4$  layers are significantly higher than the associated interfacial resistances [193, 196]. Consequently, the interfacial resistances are disregarded. Additional details regarding the parameters used in TDTR analyses can be found in previous publications [193].

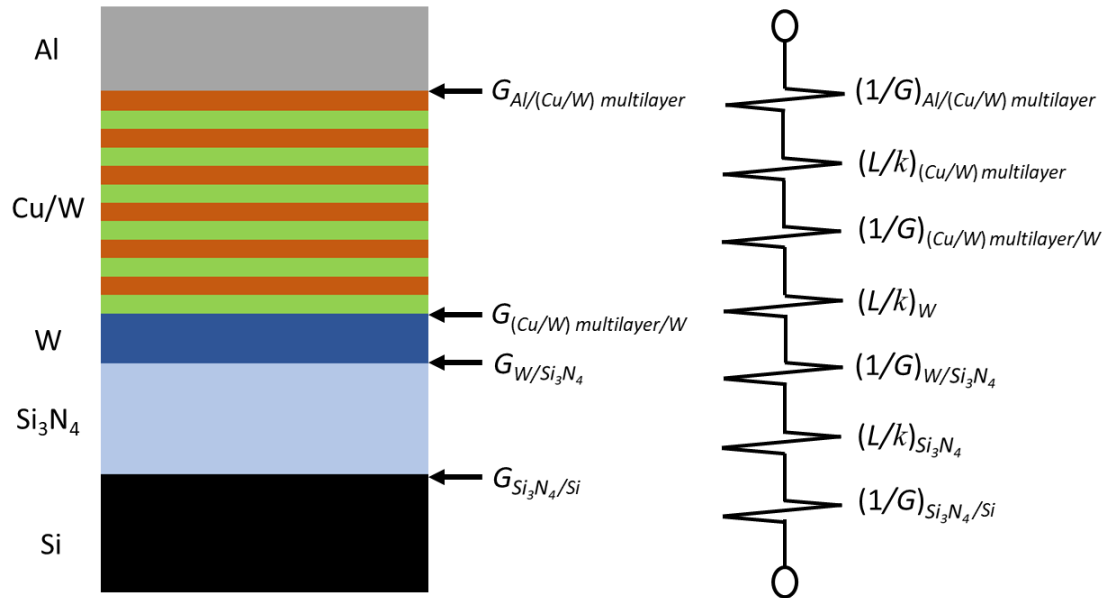


Figure 7.3: Schematic diagram of the sample geometry exhibiting the thermal resistances between the Al transducer and Si substrate.

To validate the assumptions used for the TDTR measurements and analysis, we employ

the SSTR technique. Using large  $1/e^2$  pump and probe radii ( $\sim 20 \mu\text{m}$ ), we fit the seven resistances between the Al transducer and Si substrate as a single thermal resistance ( $R$ ) in SSTR. This thermal resistance can be expressed by the following equation:

$$R = \left(\frac{1}{G}\right)_{Al/(Cu/W)multilayer} + \left(\frac{L}{\kappa}\right)_{(Cu/W)multilayer} + \left(\frac{1}{G}\right)_{(Cu/W)multilayer/W} + \left(\frac{L}{\kappa}\right)_W + \left(\frac{1}{G}\right)_{W/Si_3N_4} + \left(\frac{L}{\kappa}\right)_{Si_3N_4} + \left(\frac{1}{G}\right)_{Si_3N_4/Si}. \quad (7.1)$$

The TDTR-measured thermal conductivity of the as-deposited tensile NML is  $9.1 \pm 0.98 \text{ W m}^{-1} \text{ K}^{-1}$ . The thermal conductivity of the as-deposited compressive NML is  $22.9 \pm 4.6 \text{ W m}^{-1} \text{ K}^{-1}$ , nearly 2.5 times higher compared to the tensile NML. The difference in cross-plane thermal conductivity between the tensile and compressive specimens in the as-deposited state can be directly correlated to microstructure. The W layers of the tensile NML are much more disordered compared to the W layers of the compressive NML. The interfacial roughness of the tensile NML is also much higher than that of the compressive NML. Moreover, the tensile NML has a smaller grain size. The structural disorder and smaller grain size result in a significantly lower thermal conductivity of the as-deposited tensile NML [39, 193, 197–199].

The thermal conductivity of the tensile and compressive specimens after annealing at different temperatures is also measured (after cooling down to RT) as shown in Figure 7.4. Within the uncertainty of the measurement, the thermal conductivity of the compressive NML remains approximately constant up to  $800 \text{ }^\circ\text{C}$ , followed by a sharp decrease at  $850 \text{ }^\circ\text{C}$ . Indeed, the compressive NML remains stable up to  $800 \text{ }^\circ\text{C}$ . The NML-to-NC transformation sets in at  $T > 800 \text{ }^\circ\text{C}$  and is partially completed after the annealing at  $850 \text{ }^\circ\text{C}$ . The nanocomposite structure introduces additional electron and phonon scattering mechanisms, resulting in a substantial decrease of the thermal conductivity [200–202]. A completely different trend is observed for the tensile NML. The thermal conductivity of the tensile

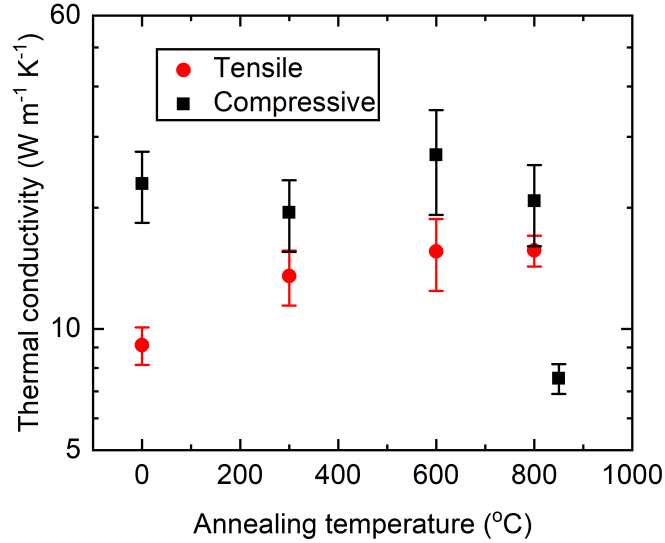


Figure 7.4: Thermal conductivity of the tensile and compressive samples as a function of annealing temperature.

NML gradually increases with annealing temperature, which is attributed to the reduction of atomic disorder.

The thermal resistance between the Al transducer and the Si substrate (i.e., the  $R$  value) is measured by SSTR for the as-deposited and NMLs annealed at 600 °C. The results are presented in Table 7.1. The  $R$  values derived independently by SSTR and TDTR are in excellent agreement (within the uncertainty of both measurement methods) and nearly the same for the selected samples, despite the vastly different microstructure and thermal conductivity of the different Cu/W NML variants. This indicates that the contribution of the Cu/W NMLs to the thermal resistance,  $R$ , is relatively small. This suggests that the ther-

Table 7.1: Thermal resistance between the Al transducer and the Si substrate,  $R$ , for the as-deposited and annealed (at 600 °C) Cu/W NMLs, as derived by SSTR and TDTR.

Specimen	$R$ value ( $\text{m}^2 \text{K GW}^{-1}$ )	
	SSTR	TDTR
Tensile as-deposited	$71 \pm 14.9$	$79 \pm 9$
Compressive as-deposited	$64.5 \pm 12.7$	$70 \pm 9.1$
Tensile annealed at 600 °C	$78.1 \pm 14.8$	$75.7 \pm 8.9$
Compressive annealed at 600 °C	$67.1 \pm 14.8$	$73.5 \pm 9.2$

mal performance of a NML device or functional component with a similar geometry will not be significantly impacted by the stresses and microstructure generated during fabrication. However, such intrinsic stresses and microstructure will adversely impact the thermal stability and, thereby, the device lifetime.

## 7.4 Summary

The stress state and microstructure of Cu/W NMLs affect their thermal stability and thermal conductivity. The compressive system has manifested overall better performance: its thermal conductivity is 2.5 times higher than that of the tensile system in the as-deposited state. This number directly scales with the internal atomic disorder which is also 3 times higher in the tensile samples. Additionally, the compressive sample is thermally more stable and it requires much higher annealing temperatures to turn into a nanocomposite. Although the thermal conductivity of the tensile sample improves with annealing, it underperforms the compressive sample until 800 °C. The works presented in this chapter shed light into the interplay between internal stress, microstructure, thermal stability, and thermal conductivity of Cu/W NMLs.

## Chapter 8

# Extending SSTR measurements to high temperatures

In this chapter, I extend thermal characterizations of a high-entropy ceramic beyond ambient conditions using SSTR. The works presented in this chapter have been published in *Journal of European Ceramic Society* [203].

### 8.1 Motivation

High-entropy ceramics have garnered a lot of attention in recent years due to their unique mechanical, physical, and thermal characteristics [53, 204, 205]. Typically in a high-entropy ceramic, five or more components are mixed in equimolar or near-equimolar concentrations to maximize the configuration entropy and minimize the Gibbs free energy [206–210]. The minimization of Gibbs free energy leads to higher thermodynamic stability, making high-entropy ceramics promising for a wide array of applications. To date, different types of high-entropy ceramics, such as metal diborides [211, 212], metal carbides [213–218], nitrides [208, 219], sulfides [220], silicides [221, 222], fluorites [223, 224], and oxides [225–231] have been successfully fabricated.

Among different classes of high-entropy ceramics, metal diborides and carbides fall

into the category of ultra-high temperature ceramics (UHTCs), i.e., materials suitable for extreme environment applications such as next generation gas turbines, rocket nozzles, and scramjet propulsion [232]. Prior to the successful fabrication of high-entropy metal diborides and carbides, the pool of UHTCs were mostly limited to monolithic binary borides and carbides. Several of them, such as  $\text{ZrB}_2$ ,  $\text{ZrC}$ ,  $\text{HfB}_2$ , and  $\text{HfC}$ , have been studied for decades for advanced aerospace applications [233, 234]. However, the diverse demands of the aerospace, energy, and nuclear industries have made it a necessity to expand the pool of UHTCs and characterize their properties [235].

Thus far, the vast majority of the characterizations performed on high-entropy metal diborides and carbides have focused on room-temperature thermal and mechanical properties [236, 237]. To properly assess the suitability of high-entropy metal diborides and carbides for extreme environment applications, it is necessary to extend the characterizations beyond ambient conditions. Towards this goal, we use SSTR to perform a series of thermal conductivity measurements on a single-phase high-entropy diboride (HEB) in this chapter. The composition of the studied HEB is  $(\text{Hf}_{0.2}\text{Zr}_{0.2}\text{Ti}_{0.2}\text{Ta}_{0.2}\text{Nb}_{0.2})\text{B}_2$ .

## 8.2 Growth and characterization details

The HEB possesses a single-phase, hexagonal crystal structure ( $\text{AlB}_2$ ) [238] with high symmetry [211, 221]. Figure 8.1 shows the highly anisotropic layered crystal structure of the HEB consisting of alternating rigid two-dimensional (2D) boron nets and 2D layers of five metal cations (Hf, Zr, Ti, Ta, and Nb) [211]. The polycrystalline HEB sample is fabricated by reactive spark plasma sintering of ball milled elemental powders [239]. During spark plasma sintering, the powders are first held at temperatures of 1400 and 1600 °C for 80 minutes each to allow for sufficient outgassing and native oxide reduction. The temperature is then raised at 30 °C/min to the final sintering temperature of 2200 °C and held for 30 minutes, prior to cooling to room temperature in 15 - 20 minutes. A pressure of 80 MPa is applied at the maximum temperature to enable full densification. The prepared

specimen is highly dense (> 98% of theoretical density) and contains negligible amount of native oxide contaminants. The composition of the sample is measured by EDS to be 98%  $(\text{Hf}_{0.19}\text{Zr}_{0.19}\text{Ti}_{0.22}\text{Ta}_{0.19}\text{Nb}_{0.18}\text{W}_{0.03})\text{B}_2$  with residual amount of carbide phase [239]. The average grain size of the HEB specimen is  $15 \pm 9.5 \mu\text{m}$ , as measured by electron backscatter diffraction (EBSD). A detailed description of the HEB sample fabrication and characterization can be found in Qin *et al.* [239]. The HEB specimen is prepared and characterized by Dr. Jian Luo's group at the University of California, San Diego. Dr. Eric R. Hoglund from the University of Virginia also contributed to the characterizations.

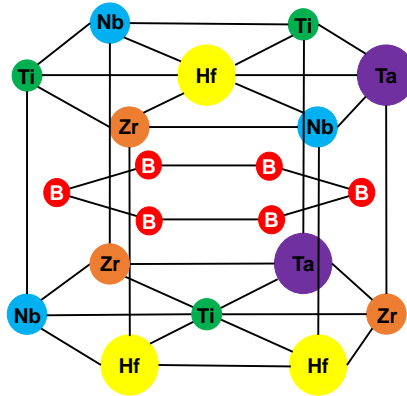


Figure 8.1: Schematic diagram of the crystal structure of  $(\text{Hf}_{0.2}\text{Zr}_{0.2}\text{Ti}_{0.2}\text{Ta}_{0.2}\text{Nb}_{0.2})\text{B}_2$  (taken and modified from Gild *et al.* [211]).

### 8.3 Results and discussion

To measure the thermal conductivity of HEB, we employ three different thermal characterization techniques: SSTR, TDTR, and LFA [240]. SSTR and TDTR are used to measure the thermal conductivity up to 290 and 600 °C, respectively. LFA is used to measure thermal diffusivity up to 1267 °C from which we extract the thermal conductivity. Although SSTR can measure the thermal conductivity independent of heat capacity, TDTR and LFA measurements require knowledge of HEB heat capacity [39, 55, 241]. To this end, we assume that the heat capacity of the HEB and  $\text{ZrB}_2$  is the same. This assumption is later

verified in subsequent sections.

Table 8.1: Thermal conductivity and volumetric heat capacity of the HEB specimen measured in this study. For comparison, we also include the relevant properties of the constituent metal diborides from the literature. The thermal conductivity of high-quality TaB<sub>2</sub> has not been previously reported in the literature.

Materials	Thermal conductivity (W m <sup>-1</sup> K <sup>-1</sup> )	Volumetric heat capacity (MJ m <sup>-3</sup> K <sup>-1</sup> )
(Hf <sub>0.2</sub> Zr <sub>0.2</sub> Ti <sub>0.2</sub> Ta <sub>0.2</sub> Nb <sub>0.2</sub> )B <sub>2</sub>	27.8 ± 2.9	2.84 ± 0.34
HfB <sub>2</sub>	107 [242]	2.81 [10, 243]
ZrB <sub>2</sub>	127 [244]	2.95 [244]
TiB <sub>2</sub>	96 [245]	2.84 [10]
TaB <sub>2</sub>	-	3.05 [10]
NbB <sub>2</sub>	102 [246]	2.91 [10, 247]

The room-temperature thermal conductivity of the HEB sample is  $27.8 \pm 2.9$  W m<sup>-1</sup> K<sup>-1</sup>. This is in agreement with literature [212, 239]. As exhibited in Table 8.1, the thermal conductivity of the HEB is significantly lower compared to the monolithic diborides. Both electrons and phonons contribute to the thermal conductivity of these diborides [238, 248–250]. A small amount of impurities can reduce the thermal conductivity of the monolithic diborides significantly [251, 252]. However, we attribute the thermal conductivity reduction in HEB to the significant electron and phonon scattering caused by the lattice distortions and compositional disorder [53, 253]. The localized mass and interatomic bond strength differences among the five metal cations in the HEB cause lattice distortions as evident by the changes in lattice parameters compared to the single diboride counterparts [53, 211, 213, 221]. In addition, the 2D rigid boron nets highly strain the metal-metal bonding within the 2D cation layers leading to further electron and phonon scattering [211]. Due to such extensive nature of electron and phonon scattering, the presence of small impurities (i.e., tungsten or the carbide phase) is not expected to cause a significant reduction in HEB thermal conductivity [19, 239].

To approximate the electron contribution ( $\kappa_e$ ) to the thermal conductivity of the HEB, we use the Wiedemann–Franz law:  $\kappa_e = \sigma_e L T$ , where  $\sigma_e$ ,  $L$ , and  $T$  represent electrical conductivity, Lorentz number, and temperature, respectively [250]. For this purpose, we

measure the electrical conductivity via the four-point probe method and use a Lorentz number of  $2.45 \times 10^{-8} \text{ W } \Omega \text{ K}^{-2}$ . This ideal Lorentz number has been previously used to estimate the  $\kappa_e$  values of  $\text{ZrB}_2$  [254],  $\text{HfB}_2$  [255],  $\text{ZrB}_2\text{-TiB}_2$  [254], and  $\text{ZrB}_2\text{-SiC}$  [250] ceramics. The measured electrical conductivity of the HEB specimen is  $(2.42 \pm 0.12) \times 10^6 \text{ S/m}$ . This value corresponds to an electron contribution of  $18.1 \pm 0.9 \text{ W m}^{-1} \text{ K}^{-1}$ , nearly 65% of the total thermal conductivity of HEB. Thus, our measurement provides the first empirical evidence that the thermal conductivity of HEB is electron dominated.

The temperature-dependent thermal conductivity of the HEB specimen is presented in Figure 8.2(a). For comparison, we also include the thermal conductivity of several traditional UHTCs such as  $\text{ZrB}_2$  [244],  $\text{ZrB}_2\text{-30 vol% SiC}$  [250], and  $\text{HfB}_2\text{-20 vol% SiC}$  [242]. As evident here, at room temperature, the thermal conductivity of these ceramics is significantly higher than that of the HEB. However, as temperature increases, the thermal conductivity of HEB,  $\text{ZrB}_2$ ,  $\text{ZrB}_2\text{-30 vol% SiC}$ , and  $\text{HfB}_2\text{-20 vol% SiC}$  ceramics starts to converge. The increase in thermal conductivity of the HEB with temperature can be attributed to its electron dominated thermal transport [254]. This trend provides optimism that at elevated

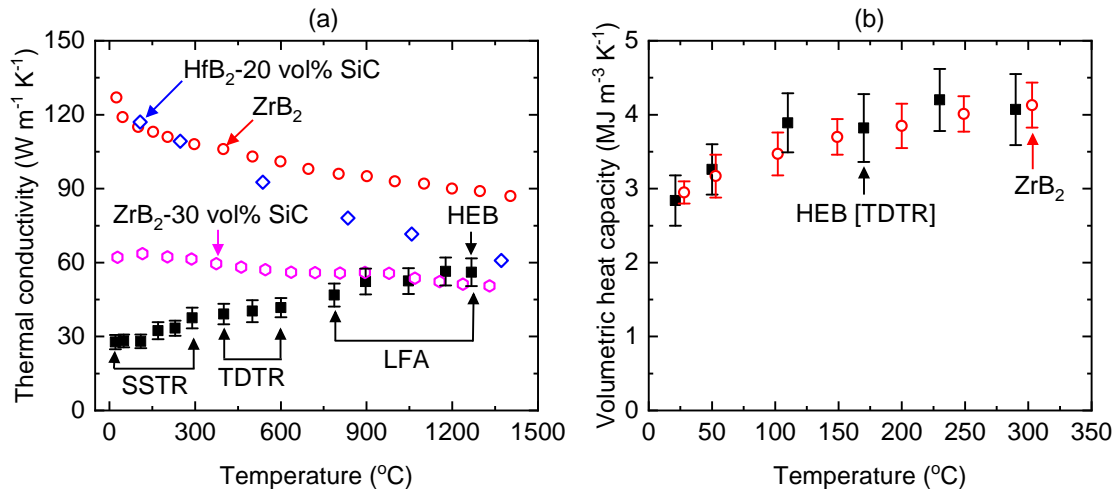


Figure 8.2: (a) Temperature-dependent thermal conductivity of HEB measured via three different techniques: SSTR (21 - 290  $^{\circ}\text{C}$ ), TDTR (400 - 600  $^{\circ}\text{C}$ ), and LFA (787 - 1267  $^{\circ}\text{C}$ ). For comparison, we also include the thermal conductivity of  $\text{ZrB}_2$  [244],  $\text{ZrB}_2\text{-30 vol% SiC}$  [250], and  $\text{HfB}_2\text{-20 vol% SiC}$  [242] from literature. (b) Temperature-dependent heat capacity of HEB along with that of  $\text{ZrB}_2$  [244].

temperatures (i.e., > 2000 °C), the thermal conductivity of HEB can become comparable to or even higher than that of other UHTCs. At such temperatures, high thermal conductivity is desired of UHTCs to avoid failure due to thermal shock [232, 242, 252]. Therefore, the thermal conductivity measurements show that the HEB is a promising material for extreme environment applications such as hypersonic aerospace vehicles.

Using the SSTR-measured thermal conductivity as an input parameter, we extract the volumetric heat capacity of HEB from TDTR measurements up to 290 °C. The room-temperature heat capacity of the HEB specimen is presented in Table 8.1. As exhibited here, the heat capacity of HEB is nearly the same as that of the constituent diborides. Furthermore, this value is in agreement with the rule of mixture [256] prediction (2.91 MJ m<sup>-3</sup> K<sup>-1</sup>). The temperature-dependent heat capacity of the HEB specimen is presented in Figure 8.2(b). The excellent agreement shown between HEB and ZrB<sub>2</sub> supports our earlier assumption that the volumetric heat capacities of the two materials are nearly identical.

To investigate the presence of any anisotropy in the thermal conductivity of HEB, we spatially map the HEB specimen using TDTR. For comparison, we also spatially map the thermal conductivity of a reference ZrB<sub>2</sub> system provided to us by Dr. W. G. Fahrenholtz from Missouri University of Science and Technology. The ZrB<sub>2</sub> specimen is prepared by reactive hot pressing and has a relative density > 96% [244, 252]. EDS technique reveals the presence of 92-93 wt% zirconium in the ZrB<sub>2</sub> specimen. The sample also contains oxygen, magnesium, titanium, and strontium impurities, and has an average grain size of 7.3 ± 4.2 μm. Therefore, we use a probe spot size (1/e<sup>2</sup> diameter) of 6 μm or less and a modulation frequency of 8.4 MHz for TDTR mapping to ensure that the thermal penetration depth (< 1.5 μm) remains lower than the HEB and ZrB<sub>2</sub> grain sizes [55]. At such low thermal penetration depth, TDTR mapping is a good indicator of the cross-plane thermal conductivity of individual grains. To correlate TDTR mapping with grain orientations, we perform EBSD characterization of the samples.

Figures 8.3(a<sub>1</sub>) and 8.3(a<sub>2</sub>) show the EBSD micrographs of the HEB and ZrB<sub>2</sub> specimens, respectively. The HEB grains are randomly oriented without any significant tex-

turing. In contrast, the  $\text{ZrB}_2$  grains are preferentially oriented along the 001 direction. The difference in texturing between the HEB and  $\text{ZrB}_2$  can be attributed to the different fabrication techniques of the two specimens [257, 258].

As TDTR measures the thermal conductivity along the cross-plane direction, we use the pole figures to confirm the distribution of 001 oriented grains along the Z-axis. Figure 8.3(b<sub>1</sub>) indicates that the 001 oriented grains are randomly distributed along the Z-axis in the HEB. In contrast, Figure 8.3(b<sub>2</sub>) shows that the intensity of 001 oriented grains is highest along the Z-axis in  $\text{ZrB}_2$ .

Figures 8.3(c<sub>1</sub>) and 8.3(c<sub>2</sub>) show the disorientation angle distributions of HEB and  $\text{ZrB}_2$ , respectively. For comparison, we also show the corresponding Mackenzie distribution, i.e., the theoretical distribution of a randomly oriented polycrystalline material of hexagonal crystal structure. The disorientation angle distribution for HEB largely follows the ideal Mackenzie distribution, confirming that the grains are randomly oriented. For  $\text{ZrB}_2$ , there is an increased proportion of smaller disorientation angles compared to that of a random distribution, indicating the presence of texturing.

The cross-plane thermal conductivity distributions of HEB and  $\text{ZrB}_2$  are presented in Figures 8.3(d<sub>1</sub>) and 8.3(d<sub>2</sub>), respectively. The thermal conductivity maps used to extract the distributions are provided in the Supporting Information. As exhibited in Figure 8.3(d<sub>1</sub>), the thermal conductivity of HEB is relatively symmetric around the mean value. Nearly 89% of the pixel counts can be found within just  $\sim 15\%$  of the mean value. The results are confirmed in multiple thermal conductivity maps on different regions of the HEB specimen. The lower thermal conductivity pixel counts of Figure 8.3(d<sub>1</sub>) likely stem from impurities such as the carbide phase. Due to the presence of such impurities, the HEB thermal conductivity distribution has a skewness value less than -1. For comparison, the thermal conductivity distribution of  $\text{ZrB}_2$  is nearly 24 times more skewed. This can be attributed to the higher impurity concentrations of the  $\text{ZrB}_2$  specimen. The 001 oriented grains of  $\text{ZrB}_2$  can possess thermal conductivities ranging from 95 to 102  $\text{W m}^{-1} \text{K}^{-1}$ , whereas grains oriented along other crystallographic directions can have a thermal conductivity above 120

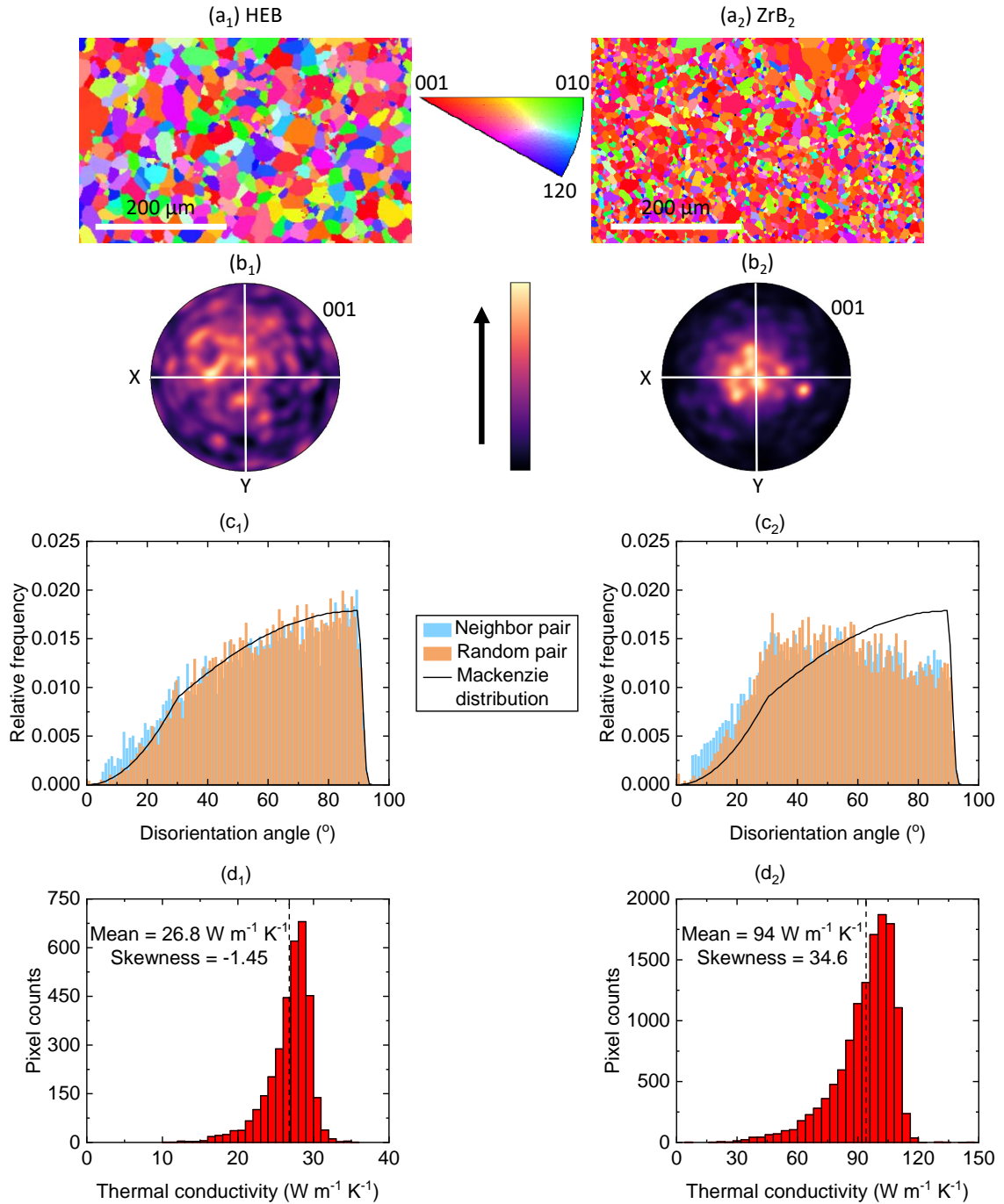


Figure 8.3: [a<sub>1</sub>, a<sub>2</sub>] EBSD micrographs exhibiting the grain orientations in HEB and ZrB<sub>2</sub>. [b<sub>1</sub>, b<sub>2</sub>] Pole figures exhibiting the distribution of 001 oriented grains along the Z-axis. [c<sub>1</sub>, c<sub>2</sub>] Disorientation angle distributions extracted from the EBSD data. [d<sub>1</sub>, d<sub>2</sub>] Thermal conductivity distributions extracted from TDTR mapping. Subscript 1 and 2 denote HEB and ZrB<sub>2</sub>, respectively.

$\text{W m}^{-1} \text{K}^{-1}$  [244, 259]. The absence of pixel counts with thermal conductivities above  $120 \text{ W m}^{-1} \text{K}^{-1}$  shows that the mean thermal conductivity of Figure 8.3(d<sub>2</sub>) is representative of  $\text{ZrB}_2$  textured along the 001 crystallographic direction.

The relatively symmetric distribution and similar thermal conductivity maps on multiple regions of the HEB specimen reveal that the thermal conductivity of HEB is nearly isotropic across different crystallographic orientations. Therefore, the temperature dependent thermal conductivity values exhibited in Figure 8.2(a) is representative of HEB textured in any orientation. However, we note that even for materials with anisotropic thermal conductivity, such as  $\text{ZrB}_2$ , the effect of anisotropy is likely to be very small at high temperatures [244, 252].

## 8.4 Summary

The thermal properties of a HEB are presented in this chapter. Our work reveals that the electrons contribute to nearly 65% of the total thermal conductivity of HEB. We use multiple thermal characterization techniques to measure the HEB thermal conductivity up to  $1267 \text{ }^\circ\text{C}$ . The comparable thermal conductivity of HEB with that of other UHTCs at such temperatures provides evidence that the HEB can be a promising material for use in hypersonic aerospace vehicles and advanced rocket nozzles. The HEB also possesses a nearly isotropic thermal conductivity along all crystallographic directions, contrary to that of other binary diborides, such as  $\text{ZrB}_2$ . The volumetric heat capacities of HEB and  $\text{ZrB}_2$  remain nearly the same as a function of temperature. The characterizations performed in this chapter mark a significant advancement towards employing of HEB for ultra-high temperature applications.

## Chapter 9

# Validating heat capacity assumptions of a perovskite chalcogenide

One of the biggest advantages of SSTR technique is its insensitivity to heat capacity. Here, I use this advantage of SSTR to validate heat capacity assumptions of a perovskite chalcogenide. The works presented in this chapter are currently under preparation for a journal submission.

### 9.1 Motivation

Perovskite chalcogenide  $\text{BaZrS}_3$  and its Ruddlesden-popper derivatives (i.e.,  $\text{Ba}_3\text{Zr}_2\text{S}_7$  and  $\text{Ba}_4\text{Zr}_3\text{S}_{10}$ ) are suitable material candidates for optoelectronic, thermoelectric [260], and photovoltaic applications [261]. To properly use them in such applications, thermal characterizations are of vital interest. TDTR is able to measure the thermal conductivity of crystalline and amorphous  $\text{BaZrS}_3$  as well as its Ruddlesden-popper (RP) derivatives. However, such measurements require assumptions of heat capacity. As SSTR is insensitive to heat capacity, it can directly measure the thermal conductivity of these materials and can validate any heat capacity assumptions used in TDTR or FDTR.

## 9.2 Growth and characterization details

The  $\text{BaZrS}_3$  and  $\text{Ba}_3\text{Zr}_2\text{S}_7$  crystals are synthesized using the flux method [262]. 1 g of  $\text{BaCl}_2$  powder (Alfa Aesar, 99.998%) is grounded and mixed with 0.5 g of stoichiometric mixtures of precursor powders (BaS, Zr, and S), and loaded into a quartz tube. For  $\text{BaZrS}_3$ , the tube is heated to 1050 °C at a rate of 1.6 °C/min, held at 1050 °C for 100 h, cooled to 800 °C at a rate of 0.1 °C/min, and then to room temperature in an uncontrolled manner by shutting off the furnace. For  $\text{Ba}_4\text{Zr}_3\text{S}_{10}$ , the tube is heated to 1050 °C at a rate of 0.3 °C/min, held at 1050 °C for 40 h, cooled to 400 °C at a rate of 1 °C/min, and then to room temperature in an uncontrolled manner.  $\text{Ba}_4\text{Zr}_3\text{S}_{10}$  is formed as a secondary phase twined with some large  $\text{Ba}_3\text{Zr}_2\text{S}_7$  crystals. X-ray diffraction along 001 orientation [263] is used to characterize their existence, so  $\text{Ba}_4\text{Zr}_3\text{S}_{10}$  layers are exfoliated to access them. The obtained samples are washed repeatedly with deionized water and isopropyl alcohol to remove excess flux before drying in airflow. The crystal dimensions are on the order of  $\sim 100 \mu\text{m}$ .

Figure 9.1 shows the structure and TEM characterizations of  $\text{BaZrS}_3$  and  $\text{Ba}_3\text{Zr}_2\text{S}_7$ . The perovskite shown in Figure 9.1(a) consists of tilted  $\text{ZrS}_6$  octahedra (Figure 9.1(c)) and  $\text{BaS}_{12}$  polyhedral that are distorted from the octahedral rotation (Figures 9.1(d) and 9.1(e)). The  $\text{Ba}_3\text{Zr}_2\text{S}_7$  RP phases shown in Figure 9.1(b) contains two perovskite sections (red brackets) that are separated by rock-salt packed layers. Figure 9.1(g) shows an iDPC image of  $\text{BaZrS}_3$  viewed along the in-phase tilt axis. The Ba-Ba distance projected along the  $c$ -axis is plotted in Figure 9.1(j). Figures 9.1(h) and 9.1(i) show the layered periodic stacking of perovskite layers in the two RP phases with the enlarged regions of interest emphasizing one of two rock-salt layers that are present in a single unit cell. The electron energy-loss elemental maps and corresponding atomic number contrast image shown in Figures 9.1(k) – 9.1(o) show the high degree of chemical ordering in each sublattice and the change in local symmetry at the rock-salt layers. The out-of-plane projected Ba-Ba distances in the Ruddlesden-Popper show that the distance across the rock-salt layers is

not an integer multiple of the perovskite as a result of the redistributed bonds when the rock-salt layers are introduced.

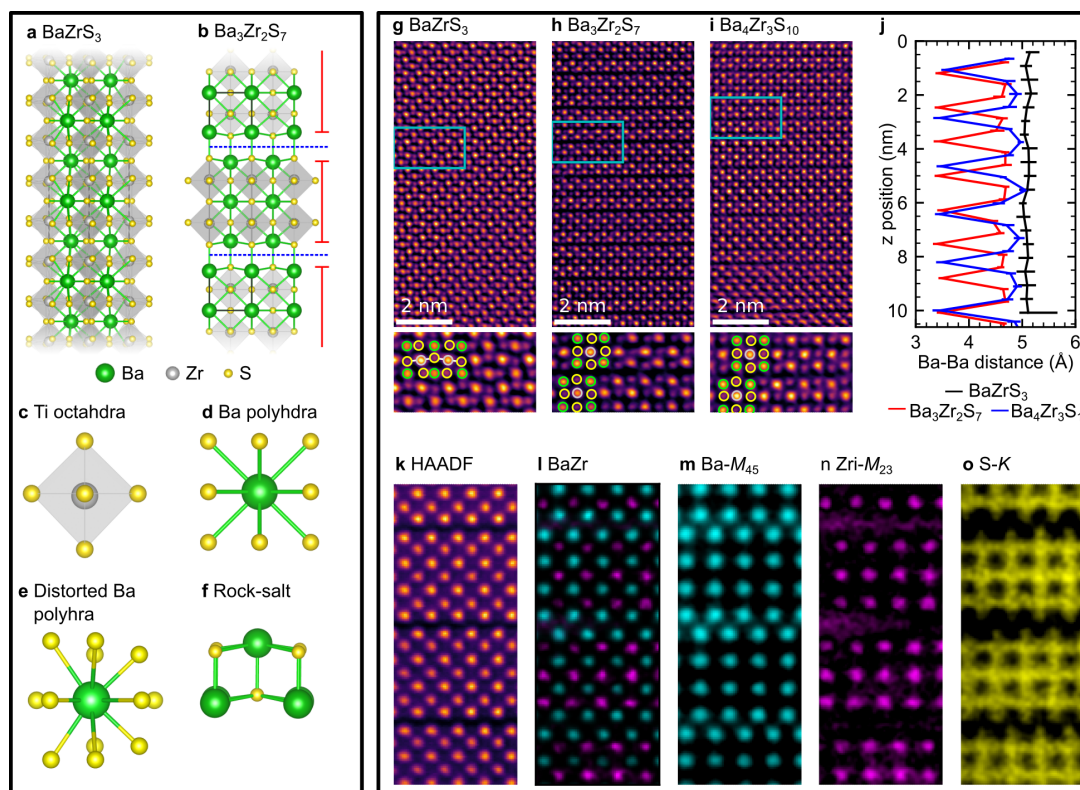


Figure 9.1: Structure of perovskite and Ruddlesden-Popper  $Ba_{n+1}Zr_nS_{3n+1}$ . Ball-and-stick model of (a)  $Pnma$  perovskite  $BaZrS_3$  and (b)  $I4mmm$  Ruddlesden-Popper  $Ba_3Zr_2S_7$  showing grey  $TiS_6$  octahedra and green  $BaS$  bonds. Red markers in (b) indicate the perovskite blocks of the RP phase separated by the rock-salt blocks. Blue dotted lines between  $BaS$  atomic planes indicate the intra-unit cell interface-like planes. Ball-and-stick model of a (c) Zr octahedra and (d) undistorted Ba polyhedral. (e) Distorted Ba polyhedral resulting from octahedral tilts in  $BaZrS_3$  and (f) rock-salt building block resulting from layering in  $Ba_3Zr_2S_7$ . Integrated differential phase contrast images of the (g)  $BaZrS_3$ , (h)  $Ba_3Zr_2S_7$ , and (i)  $Ba_4Zr_3S_{10}$  crystals. Enlarged regions from the cyan annotations are shown below each image. In the enlargements, two perovskites unit cells are annotated with Ba (green), Ti (grey), and S (yellow) circles. The (j) cross-plane projected Ba-Ba distance in (g-h) showing the periodic structure of the perovskite and rock-salt like sections of the RP phases. (k) atomic-number contrast image and (l) BaZr composite image from a STEM-EELS spectrum image. Intensity maps of (m) Ba- $M_{45}$ , (n) Zr- $M_{23}$ , and (o) S-K background-subtracted edges.

The samples discussed in this chapter are grown by Dr. Jayakanth Ravichandran's group at the University of Southern California. Dr. Eric R. Hoglund from the University of Virginia performed the characterizations.

### 9.3 Results and discussion

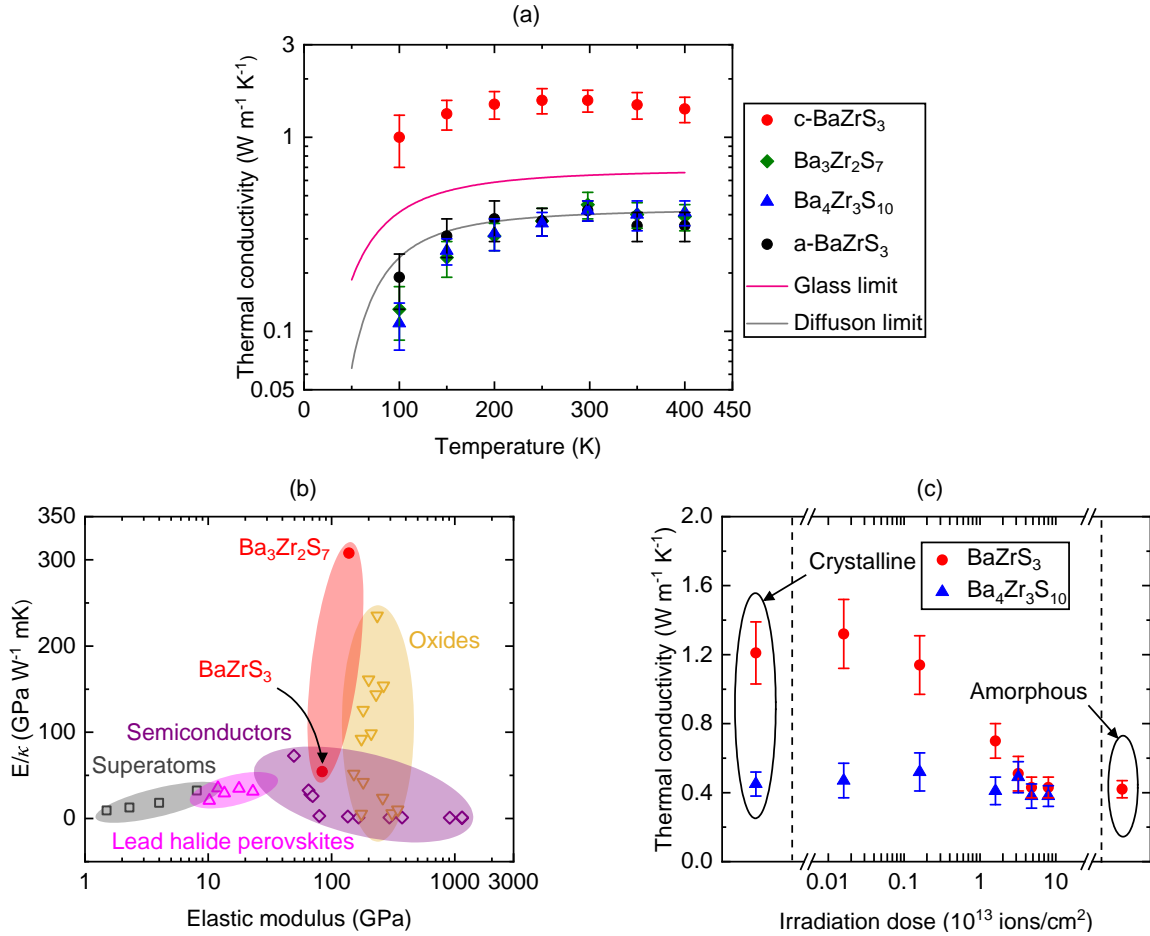


Figure 9.2: TDTR-measured cross-plane thermal conductivity of BaZrS<sub>3</sub> and its RP derivatives. c-BaZrS<sub>3</sub> and a-BaZrS<sub>3</sub> denote crystalline and amorphous BaZrS<sub>3</sub>, respectively. (b) Elastic modulus/thermal conductivity ( $E/\kappa$ ) ratio for a wide range of crystalline materials at room temperature. The crystals are grouped into superatoms, lead halide perovskites, semiconductors, oxides, and BaZrS<sub>3</sub> and its RP derivatives. The thermal conductivity and elastic modulus data are taken from Refs [25, 53, 112, 128, 166, 264–287]. (c) Thermal conductivity distribution of BaZrS<sub>3</sub> and RP phases as a function of ion-irradiation doses. The thermal conductivity of the crystalline BaZrS<sub>3</sub> is lower compared to panel (a) due to the presence of nano-domains in some of the crystals.

We measure the cross-plane (along  $c$ -axis) thermal conductivity of the materials using TDTR from 100 to 400 K, as shown in Figure 9.2(a). For this purpose, we calculate the volumetric heat capacity of crystalline BaZrS<sub>3</sub> and Ba<sub>3</sub>Zr<sub>2</sub>S<sub>7</sub> using density functional theory. Additionally, we assume that the crystalline and amorphous BaZrS<sub>3</sub> possess the

same volumetric heat capacity. To ensure the validity of this assumption, we measure the room-temperature thermal conductivity of a  $\sim 107$  nm amorphous  $\text{BaZrS}_3$  film grown on silicon substrate via both TDTR and SSTR techniques. The measured thermal conductivity is in excellent agreement between the two techniques, thus proving the accuracy of the volumetric heat capacity assumed for amorphous  $\text{BaZrS}_3$  in TDTR.

The thermal conductivities exhibit two unusual features. First, the thermal conductivity of the crystals increases from 100 to 200 K, then remains relatively temperature independent, which is rare for crystalline materials. Second, the RP phases possess ultra-low thermal conductivities in agreement with the diffuson limit and much lower than the glass limit. Additionally, the thermal conductivities are comparable to that of amorphous  $\text{BaZrS}_3$ . Such ultra-low thermal conductivity has also been observed in van der Waals layered 2D-materials such as  $\text{WSe}_2$  [33]. However, the bonds in the rock-salt layers of RP phase are comparable to the strong bonds in the perovskite sections.

To compare the bond strength of  $\text{BaZrS}_3$  and its RP derivatives with other materials, we plot the elastic modulus/thermal conductivity ( $E/\kappa$ ) ratio of a wide range of crystals in Figure 9.2(b). The elastic modulus of  $\text{BaZrS}_3$  and RP phases is higher than supertatoms, lead halide perovskites, and even some semiconductors. Despite such strong bonding, the RP phases possess an ultra-low thermal conductivity. As a result, the  $E/\kappa$  ratio of the  $\text{Ba}_3\text{Zr}_2\text{S}_7$  crystal is the highest reported to date, much higher than the closest oxide competitor. It is also unprecedented that different phases of the same material can span across such a wide range of  $E/\kappa$  ratios.

To further show the strong bonding across the rock-salt layers, we irradiate  $\text{BaZrS}_3$  and  $\text{Ba}_4\text{Zr}_3\text{S}_{10}$  crystals with energized gold ions. The measured cross-plane thermal conductivity of the irradiated crystals as a function of ion doses is shown in Figure 9.2(c). The thermal conductivity of  $\text{BaZrS}_3$  exhibits a sigmoidal reduction, typically characteristic of irradiated crystalline materials [288]. At low doses, irradiation introduces lower amount of point defects and vacancies, and the crystal structure remains relatively unchanged, therefore the thermal conductivity is nearly constant. At high doses, point defects and vacancies

increase, which gradually decreases the thermal conductivity to that of an amorphous solid, as observed in  $\text{BaZrS}_3$ .

Compared to  $\text{BaZrS}_3$ , a completely different trend is observed in the RP phases. The thermal conductivity of the  $\text{Ba}_4\text{Zr}_3\text{S}_{10}$  crystals remains nearly constant as a function of ion doses. TEM characterizations show that the layering of  $\text{Ba}_4\text{Zr}_3\text{S}_{10}$  crystals remain uninterrupted throughout the range of doses, although high doses can introduce amorphous pockets. In weakly bonded van der Waals layered materials, ion irradiation can lead to disruptions in crystalline order and increased thermal conductivity [33]. However, due to strong bonding of the RP phases, no such trend is observed in our work. The thermal conductivity also does not decrease with ion doses despite irradiation increasing point defects and disorders within an intra-layer [288, 289]. This indicates that increased phonon scattering due to irradiation is not impacting the thermal transport in RP phases. To gain further insight into this, we measure the thermal conductivity of  $\text{Ba}_3\text{Zr}_2\text{S}_7$  along the in-plane direction (perpendicular to  $c$ -axis). The in-plane thermal conductivity is  $1.06 \pm 0.14 \text{ W m}^{-1} \text{ K}^{-1}$ ,  $\sim 2.5$  times higher compared to the cross-plane thermal conductivity. The major structural difference between the in-plane and cross-plane directions is the rock-salt layers. This suggests that the structural building blocks in the unit cell can lead to ultra-low and anisotropic thermal conductivity similar to weak bonding in van der Waals layered materials.

## 9.4 Summary

The thermal conductivity of RP phases of  $\text{BaZrS}_3$  is found to be ultra-low. We find that the rock-salt layers separating the perovskite sections of the Ruddlesden-Popper material lead to highly anisotropic thermal conductivity, with the cross-plane reaching values comparable to the amorphous solid despite comparable bonding across the full unit cell. The findings of our work can provide insight into the thermal transport of all structurally layered materials.

## Chapter 10

### Summary and future works

In this dissertation, I use SSTR to investigate the fundamental thermal transport mechanisms in different materials as well as measure the thermal properties of challenging multilayered geometries. In chapter 2, I provide an overview of the dominant energy carriers in non-metallic and metallic crystals as well as amorphous materials. In chapter 3, I discuss about the thermorefectance techniques I have used in this dissertation, namely SSTR and TDTR. Chapter 4 focuses on the influence of multilayer material systems, thin metal film transducers, and thermal boundary conductances on the thermal penetration depth of the SSTR technique. I further demonstrate the ability of SSTR to measure the thermal conductivity of sub-surface buried substrates and films in this chapter. In chapter 5, I use SSTR to measure the in-plane thermal conductivity of micrometer thick aluminum nitride thin films. Our measurements reveal that the in-plane thermal transport of these films is being driven by phonon-phonon scattering. In chapter 6, I employ SSTR to investigate the cross-plane thermal transport in organic-inorganic hybrid polymer films of nanometer length scales. Chapter 7 provides an overview of the use of SSTR for measuring the thermal properties of challenging multilayered geometries. The works presented in this chapter shed light into the interplay between internal stress, microstructure, thermal stability, and thermal conductivity of copper-tungsten nanomultilayers. In chapter 8, I extend SSTR measurements beyond ambient conditions. In chapter 9, I use SSTR to validate the heat capacity

assumptions of a perovskite chalcogenide.

Based on the works presented in this dissertation, there are multiple opportunities for future investigations such as the following:

- In chapter 4, I demonstrate the ability of SSTR to probe into sub-surface buried substrates and films. Using the same principle, SSTR can probe into buried interfaces when the interfacial resistance between the thin film and substrate is very high (e.g.,  $200 \text{ m}^2 \text{ K GW}^{-1}$  or greater). For such cases, the temperature drop at the interface is quite large allowing SSTR to become sensitive to it. Measuring such buried interfaces via SSTR can mark an important advancement in experimental metrology.
- In chapter 5, I use SSTR to measure the in-plane thermal conductivity of AlN thin films grown on sapphire substrates. Similarly, SSTR is able to measure the in-plane thermal conductivity of thin metallic films grown on insulating substrates. A future study into this can provide insight into the thermal transport mechanisms of metallic films and check the validity of Wiedemann-Franz law when the length scale is much smaller than the bulk value.
- In chapter 6, I use SSTR to measure the thermal properties of hybrid metalcone films. The thermal conductivity difference between alucone and tincone is attributed to the different atomic masses of the metals. It is of significant interest to verify this hypothesis by measuring the thermal properties of a third metalcone film. Towards that goal, we are currently working on thermal characterizations of zincone films.
- In chapter 9, I measure the thermal conductivity of perovskite chalcogenide  $\text{BaZrS}_3$  and its Ruddlesden-popper derivative  $\text{Ba}_3\text{Zr}_2\text{S}_7$  and  $\text{Ba}_4\text{Zr}_3\text{S}_{10}$ . The Ruddlesden-popper phases exhibit ultra-low thermal conductivities. We are currently working with multiple collaborators (Dr. Ashutosh Giri at the University of Rhode Island, Dr. Sokrates Pantelides at Vanderbilt University, and Dr. Tianli Feng at the University of Utah) to isolate the mechanism behind such ultra-low thermal conductivity.

## Bibliography

- [1] D. H. Olson, J. L. Braun, and P. E. Hopkins, “Spatially resolved thermoreflectance techniques for thermal conductivity measurements from the nanoscale to the mesoscale,” *Journal of Applied Physics*, vol. 126, no. 15, p. 150901, 2019.
- [2] J. Zhu, D. Tang, W. Wang, J. Liu, K. W. Holub, and R. Yang, “Ultrafast thermoreflectance techniques for measuring thermal conductivity and interface thermal conductance of thin films,” *Journal of Applied Physics*, vol. 108, no. 9, p. 094315, 2010.
- [3] M. Ruoho, K. Valset, T. Finstad, and I. Tittonen, “Measurement of thin film thermal conductivity using the laser flash method,” *Nanotechnology*, vol. 26, no. 19, p. 195706, 2015.
- [4] C. Lee, A. Yamamoto, T. Ohta, H. Takazawa, K. Ueno, C. Sekine, I. Shirovani, and T. Baba, “Development of a laser flash apparatus for thermal diffusivity measurement on small pieces thermoelectric materials,”
- [5] Y. Wang, J. Y. Park, Y. K. Koh, and D. G. Cahill, “Thermoreflectance of metal transducers for time-domain thermoreflectance,” *Journal of Applied Physics*, vol. 108, no. 4, p. 043507, 2010.
- [6] J. Yang, C. Maragliano, and A. J. Schmidt, “Thermal property microscopy with frequency domain thermoreflectance,” *Review of Scientific Instruments*, vol. 84, no. 10, p. 104904, 2013.
- [7] J. L. Braun, D. H. Olson, J. T. Gaskins, and P. E. Hopkins, “A steady-state thermoreflectance method to measure thermal conductivity,” *Review of Scientific Instruments*, vol. 90, no. 2, p. 024905, 2019.
- [8] C. Kittel, “Introduction to solid state physics. 8th edn, john willey and sons,” 2004.
- [9] D. G. Cahill, P. V. Braun, G. Chen, D. R. Clarke, S. Fan, K. E. Goodson, P. Keblinski, W. P. King, G. D. Mahan, A. Majumdar, *et al.*, “Nanoscale thermal transport. ii. 2003–2012,” *Applied physics reviews*, vol. 1, no. 1, p. 011305, 2014.
- [10] Y. Touloukian and E. Buyco, “Thermophysical properties of matter-the tprc data series. volume 5. specific heat-nonmetallic solids,” tech. rep., THERMOPHYSICAL AND ELECTRONIC PROPERTIES INFORMATION ANALYSIS CENTER . . . , 1970.

- [11] P. Klemens, "The scattering of low-frequency lattice waves by static imperfections," *Proceedings of the Physical Society. Section A*, vol. 68, no. 12, p. 1113, 1955.
- [12] J. Callaway, "Model for lattice thermal conductivity at low temperatures," *Physical Review*, vol. 113, no. 4, p. 1046, 1959.
- [13] G. Chen, *Nanoscale energy transport and conversion: a parallel treatment of electrons, molecules, phonons, and photons*. Oxford University Press, 2005.
- [14] G. A. Slack, R. A. Tanzilli, R. Pohl, and J. Vandersande, "The intrinsic thermal conductivity of aln," *J. Phys. Chem. Solids*, vol. 48, no. 7, pp. 641–647, 1987.
- [15] Z. Guo, A. Verma, X. Wu, F. Sun, A. Hickman, T. Masui, A. Kuramata, M. Higashiwaki, D. Jena, and T. Luo, "Anisotropic thermal conductivity in single crystal  $\beta$ -gallium oxide," *Applied Physics Letters*, vol. 106, no. 11, p. 111909, 2015.
- [16] Q. Zheng, C. Li, A. Rai, J. H. Leach, D. A. Broido, and D. G. Cahill, "Thermal conductivity of gan,  $^{71}$ gan, and sic from 150 k to 850 k," *Phys. Rev. Mater.*, vol. 3, no. 1, p. 014601, 2019.
- [17] D. G. Cahill, S. K. Watson, and R. O. Pohl, "Lower limit to the thermal conductivity of disordered crystals," *Physical Review B*, vol. 46, no. 10, p. 6131, 1992.
- [18] J. A. Harrington and C. T. Walker, "Phonon scattering by point defects in ca f 2, sr f 2, and ba f 2," *Physical Review B*, vol. 1, no. 2, p. 882, 1970.
- [19] M. Beekman and D. G. Cahill, "Inorganic crystals with glass-like and ultralow thermal conductivities," *Crystal Research and Technology*, vol. 52, no. 10, p. 1700114, 2017.
- [20] B. Sun, S. Niu, R. P. Hermann, J. Moon, N. Shulumba, K. Page, B. Zhao, A. S. Thind, K. Mahalingam, J. Milam-Guerrero, *et al.*, "High frequency atomic tunneling yields ultralow and glass-like thermal conductivity in chalcogenide single crystals," *Nature communications*, vol. 11, no. 1, pp. 1–9, 2020.
- [21] Y. Touloukian, R. Powell, C. Ho, and P. Klemens, "Thermophysical properties of matter-the tprc data series. volume 2. thermal conductivity-nonmetallic solids," tech. rep., Thermophysical and Electronic Properties Information Analysis Center . . . , 1971.
- [22] Y. Touloukian and E. Buyco, "Thermophysical properties of matter-the tprc data series. volume 4. specific heat-metallic elements and alloys," tech. rep., Thermophysical and Electronic Properties Information Analysis Center . . . , 1971.
- [23] P. E. Hopkins, P. M. Norris, L. M. Phinney, S. A. Policastro, and R. G. Kelly, "Thermal conductivity in nanoporous gold films during electron-phonon nonequilibrium," *Journal of Nanomaterials*, vol. 2008, 2008.

- [24] P. E. Hopkins, “Effects of electron-boundary scattering on changes in thermore-  
flectance in thin metal films undergoing intraband excitations,” *Journal of Applied  
Physics*, vol. 105, no. 9, p. 093517, 2009.
- [25] C. Y. Ho, R. W. Powell, and P. E. Liley, “Thermal conductivity of the elements,”  
*Journal of Physical and Chemical Reference Data*, vol. 1, no. 2, pp. 279–421, 1972.
- [26] P. B. Allen, J. L. Feldman, J. Fabian, and F. Wooten, “Diffusons, locons and  
propagons: Character of atomic vibrations in amorphous si,” *Philosophical Mag-  
azine B*, vol. 79, no. 11-12, pp. 1715–1731, 1999.
- [27] J. L. Braun, C. H. Baker, A. Giri, M. Elahi, K. Artyushkova, T. E. Beechem, P. M.  
Norris, Z. C. Leseman, J. T. Gaskins, and P. E. Hopkins, “Size effects on the thermal  
conductivity of amorphous silicon thin films,” *Physical Review B*, vol. 93, p. 140201,  
2016.
- [28] F. DeAngelis, M. G. Muraleedharan, J. Moon, H. R. Seyf, A. J. Minnich, A. J.  
McGaughey, and A. Henry, “Thermal transport in disordered materials,” *Nanoscale  
and Microscale Thermophysical Engineering*, vol. 23, no. 2, pp. 81–116, 2019.
- [29] H. R. Seyf and A. Henry, “A method for distinguishing between propagons, diffu-  
sions, and locons,” *Journal of Applied Physics*, vol. 120, no. 2, p. 025101, 2016.
- [30] A. Eucken, “Über die temperaturabhängigkeit der wärmeleitfähigkeit fester nicht-  
metalle,” *Annalen der Physik*, vol. 339, no. 2, pp. 185–221, 1911.
- [31] D. G. Cahill and R. O. Pohl, “Thermal conductivity of amorphous solids above the  
plateau,” *Physical review B*, vol. 35, no. 8, p. 4067, 1987.
- [32] D. G. Cahill and R. O. Pohl, “Lattice vibrations and heat transport in crystals and  
glasses,” *Annual review of physical chemistry*, vol. 39, no. 1, pp. 93–121, 1988.
- [33] C. Chiritescu, D. G. Cahill, N. Nguyen, D. Johnson, A. Bodapati, P. Keblinski, and  
P. Zschack, “Ultralow thermal conductivity in disordered, layered wse<sub>2</sub> crystals,”  
*Science*, vol. 315, no. 5810, pp. 351–353, 2007.
- [34] J. C. Duda, P. E. Hopkins, Y. Shen, and M. C. Gupta, “Exceptionally low thermal  
conductivities of films of the fullerene derivative pcbm,” *Physical review letters*,  
vol. 110, no. 1, p. 015902, 2013.
- [35] X. Wang, C. D. Liman, N. D. Treat, M. L. Chabinye, and D. G. Cahill, “Ultralow  
thermal conductivity of fullerene derivatives,” *Physical Review B*, vol. 88, no. 7,  
p. 075310, 2013.
- [36] K. Aryana, D. A. Stewart, J. T. Gaskins, J. Nag, J. C. Read, D. H. Olson, M. K. Gro-  
bis, and P. E. Hopkins, “Tuning network topology and vibrational mode localization  
to achieve ultralow thermal conductivity in amorphous chalcogenides,” *Nature com-  
munications*, vol. 12, no. 1, pp. 1–9, 2021.

- [37] M. T. Agne, R. Hanus, and G. J. Snyder, “Minimum thermal conductivity in the context of diffusion-mediated thermal transport,” *Energy & Environmental Science*, vol. 11, no. 3, pp. 609–616, 2018.
- [38] R. Rosei and D. W. Lynch, “Thermomodulation spectra of al, au, and cu,” *Physical Review B*, vol. 5, no. 10, p. 3883, 1972.
- [39] M. S. B. Hoque, Y. R. Koh, J. L. Braun, A. Mamun, Z. Liu, K. Huynh, M. E. Liao, K. Hussain, Z. Cheng, E. R. Hoglund, *et al.*, “High in-plane thermal conductivity of aluminum nitride thin films,” *ACS nano*, vol. 15, no. 6, pp. 9588–9599, 2021.
- [40] J. L. Braun and P. E. Hopkins, “Upper limit to the thermal penetration depth during modulated heating of multilayer thin films with pulsed and continuous wave lasers: A numerical study,” *J. Appl. Phys.*, vol. 121, no. 17, p. 175107, 2017.
- [41] J. L. Braun, C. J. Szwejkowski, A. Giri, and P. E. Hopkins, “On the steady-state temperature rise during laser heating of multilayer thin films in optical pump–probe techniques,” *Journal of Heat Transfer*, vol. 140, no. 5, 2018.
- [42] A. Giri, S. S. Chou, D. E. Drury, K. Q. Tomko, D. Olson, J. T. Gaskins, B. Kaehr, and P. E. Hopkins, “Molecular tail chemistry controls thermal transport in fullerene films,” *Physical Review Materials*, vol. 4, no. 6, p. 065404, 2020.
- [43] D. G. Cahill, “Analysis of heat flow in layered structures for time-domain thermoreflectance,” *Review of scientific instruments*, vol. 75, no. 12, pp. 5119–5122, 2004.
- [44] K. Kang, Y. K. Koh, C. Chiritescu, X. Zheng, and D. G. Cahill, “Two-tint pump-probe measurements using a femtosecond laser oscillator and sharp-edged optical filters,” *Review of Scientific Instruments*, vol. 79, no. 11, p. 114901, 2008.
- [45] D. H. Olson, J. T. Gaskins, J. A. Tomko, E. J. Opila, R. A. Golden, G. J. Harrington, A. L. Chamberlain, and P. E. Hopkins, “Local thermal conductivity measurements to determine the fraction of  $\alpha$ -cristobalite in thermally grown oxides for aerospace applications,” *Scripta Materialia*, vol. 177, pp. 214–217, 2020.
- [46] D. G. Cahill, K. Goodson, and A. Majumdar, “Thermometry and thermal transport in micro/nanoscale solid-state devices and structures,” *J. Heat Transfer*, vol. 124, no. 2, pp. 223–241, 2002.
- [47] A. J. Schmidt, X. Chen, and G. Chen, “Pulse accumulation, radial heat conduction, and anisotropic thermal conductivity in pump-probe transient thermoreflectance,” *Review of Scientific Instruments*, vol. 79, no. 11, p. 114902, 2008.
- [48] P. E. Hopkins, J. R. Serrano, L. M. Phinney, S. P. Kearney, T. W. Grasser, and C. T. Harris, “Criteria for cross-plane dominated thermal transport in multilayer thin film systems during modulated laser heating,” *Journal of Heat Transfer*, vol. 132, no. 8, 2010.

- [49] P. Jiang, X. Qian, and R. Yang, "Tutorial: Time-domain thermoreflectance (tdtr) for thermal property characterization of bulk and thin film materials," *J. Appl. Phys.*, vol. 124, no. 16, p. 161103, 2018.
- [50] G. T. Hohensee, W.-P. Hsieh, M. D. Losego, and D. G. Cahill, "Interpreting picosecond acoustics in the case of low interface stiffness," *Review of Scientific Instruments*, vol. 83, no. 11, p. 114902, 2012.
- [51] C. S. Gorham, J. T. Gaskins, G. N. Parsons, M. D. Losego, and P. E. Hopkins, "Density dependence of the room temperature thermal conductivity of atomic layer deposition-grown amorphous alumina ( $\text{Al}_2\text{O}_3$ )," *Applied Physics Letters*, vol. 104, no. 25, p. 253107, 2014.
- [52] J. L. Braun, S. W. King, A. Giri, J. T. Gaskins, M. Sato, T. Fujiseki, H. Fujiwara, and P. E. Hopkins, "Breaking network connectivity leads to ultralow thermal conductivities in fully dense amorphous solids," *Applied Physics Letters*, vol. 109, no. 19, p. 191905, 2016.
- [53] J. L. Braun, C. M. Rost, M. Lim, A. Giri, D. H. Olson, G. N. Kotsonis, G. Stan, D. W. Brenner, J.-P. Maria, and P. E. Hopkins, "Charge-induced disorder controls the thermal conductivity of entropy-stabilized oxides," *Advanced materials*, vol. 30, no. 51, p. 1805004, 2018.
- [54] K. Aryana, J. T. Gaskins, J. Nag, D. A. Stewart, Z. Bai, S. Mukhopadhyay, J. C. Read, D. H. Olson, E. R. Hoglund, J. M. Howe, *et al.*, "Interface controlled thermal resistances of ultra-thin chalcogenide-based phase change memory devices," *Nature Communications*, vol. 12, no. 1, pp. 1–11, 2021.
- [55] M. S. B. Hoque, Y. R. Koh, K. Aryana, E. R. Hoglund, J. L. Braun, D. H. Olson, J. T. Gaskins, H. Ahmad, M. M. M. Elahi, J. K. Hite, *et al.*, "Thermal conductivity measurements of sub-surface buried substrates by steady-state thermoreflectance," *Review of Scientific Instruments*, vol. 92, no. 6, p. 064906, 2021.
- [56] J.-S. Park, Y.-G. Mo, J.-K. Jeong, J.-H. Jeong, H.-S. Shin, and H.-J. Lee, "Thin film transistor and organic light-emitting display device having the thin film transistor," Sept. 18 2008. US Patent App. 12/076, 216.
- [57] K. Tokunaga, "Thin film transistor and method of manufacturing thin film transistor," Mar. 18 2010. US Patent App. 12/557, 212.
- [58] R. Venkatasubramanian, E. Siivola, T. Colpitts, and B. O'quinn, "Thin-film thermoelectric devices with high room-temperature figures of merit," *Nature*, vol. 413, no. 6856, pp. 597–602, 2001.
- [59] J.-Q. Xi, M. F. Schubert, J. K. Kim, E. F. Schubert, M. Chen, S.-Y. Lin, W. Liu, and J. A. Smart, "Optical thin-film materials with low refractive index for broadband elimination of fresnel reflection," *Nature photonics*, vol. 1, no. 3, pp. 176–179, 2007.

- [60] P. Peumans, A. Yakimov, and S. R. Forrest, "Small molecular weight organic thin-film photodetectors and solar cells," *Journal of Applied Physics*, vol. 93, no. 7, pp. 3693–3723, 2003.
- [61] Y. Yang, L. Ma, and J. Wu, "Organic thin-film memory," *Mrs Bulletin*, vol. 29, no. 11, pp. 833–837, 2004.
- [62] S. H. Sung and B. W. Boudouris, "Systematic control of the nanostructure of semiconducting-ferroelectric polymer composites in thin film memory devices," *ACS Macro Letters*, vol. 4, no. 3, pp. 293–297, 2015.
- [63] C. Dames, "Measuring the thermal conductivity of thin films: 3 omega and related electrothermal methods," *Annual Review of Heat Transfer*, vol. 16, 2013.
- [64] J. P. Feser, J. Liu, and D. G. Cahill, "Pump-probe measurements of the thermal conductivity tensor for materials lacking in-plane symmetry," *Rev. Sci. Instrum.*, vol. 85, no. 10, p. 104903, 2014.
- [65] A. J. Schmidt, R. Cheaito, and M. Chiesa, "A frequency-domain thermoreflectance method for the characterization of thermal properties," *Rev. Sci. Instrum.*, vol. 80, no. 9, p. 094901, 2009.
- [66] T. Borca-Tasciuc, A. Kumar, and G. Chen, "Data reduction in 3 $\omega$  method for thin-film thermal conductivity determination," *Review of scientific instruments*, vol. 72, no. 4, pp. 2139–2147, 2001.
- [67] T. Tong and A. Majumdar, "Reexamining the 3-omega technique for thin film thermal characterization," *Review of Scientific Instruments*, vol. 77, no. 10, p. 104902, 2006.
- [68] D. Zhao, X. Qian, X. Gu, S. A. Jajja, and R. Yang *J. Electron. Packag.*, vol. 138, no. 4, (2016).
- [69] P. Jiang, X. Qian, and R. Yang, "Time-domain thermoreflectance (tdtr) measurements of anisotropic thermal conductivity using a variable spot size approach," *Review of Scientific Instruments*, vol. 88, no. 7, p. 074901, 2017.
- [70] L. Tang and C. Dames, "Anisotropic thermal conductivity tensor measurements using beam-offset frequency domain thermoreflectance (bo-fdtr) for materials lacking in-plane symmetry," *International Journal of Heat and Mass Transfer*, vol. 164, p. 120600, 2021.
- [71] Y. R. Koh, Z. Cheng, A. Mamun, M. S. Bin Hoque, Z. Liu, T. Bai, K. Hussain, M. E. Liao, R. Li, J. T. Gaskins, *et al.* *ACS Appl. Mater. Interfaces*, vol. 12, no. 26, pp. 29443–29450, (2020).
- [72] B. Chatterjee, D. Shoemaker, Y. Song, T. Shi, H.-L. Huang, D. Keum, A. Krishnan, B. M. Foley, I. Jovanovic, J. Hwang, *et al.*, "Cumulative impacts of proton irradiation on the self-heating of algan/gan hemts," *ACS Applied Electronic Materials*, vol. 2, no. 4, pp. 980–991, 2020.

- [73] Y. K. Koh and D. G. Cahill, "Frequency dependence of the thermal conductivity of semiconductor alloys," *Physical Review B*, vol. 76, no. 7, p. 075207, 2007.
- [74] R. Wilson, B. A. Apgar, L. W. Martin, and D. G. Cahill, "Thermoreflectance of metal transducers for optical pump-probe studies of thermal properties," *Optics express*, vol. 20, no. 27, pp. 28829–28838, 2012.
- [75] C. M. Rost, J. Braun, K. Ferri, L. Backman, A. Giri, E. J. Opila, J.-P. Maria, and P. E. Hopkins, "Hafnium nitride films for thermoreflectance transducers at high temperatures: Potential based on heating from laser absorption," *Applied Physics Letters*, vol. 111, no. 15, p. 151902, 2017.
- [76] L. Wang, R. Cheaito, J. Braun, A. Giri, and P. Hopkins, "Thermal conductivity measurements of non-metals via combined time-and frequency-domain thermoreflectance without a metal film transducer," *Review of Scientific Instruments*, vol. 87, no. 9, p. 094902, 2016.
- [77] E. L. Radue, J. A. Tomko, A. Giri, J. L. Braun, X. Zhou, O. V. Prezhdo, E. L. Runnerstrom, J.-P. Maria, and P. E. Hopkins, "Hot electron thermoreflectance coefficient of gold during electron-phonon nonequilibrium," *Acs Photonics*, vol. 5, no. 12, pp. 4880–4887, 2018.
- [78] T. E. Beechem, A. E. McDonald, E. J. Fuller, A. A. Talin, C. M. Rost, J.-P. Maria, J. T. Gaskins, P. E. Hopkins, and A. A. Allerman, "Size dictated thermal conductivity of gan," *J. Appl. Phys.*, vol. 120, no. 9, p. 095104, 2016.
- [79] E. Ziade, J. Yang, G. Brummer, D. Nothorn, T. Moustakas, and A. J. Schmidt, "Thickness dependent thermal conductivity of gallium nitride," *Applied Physics Letters*, vol. 110, no. 3, p. 031903, 2017.
- [80] F. Mu, Z. Cheng, J. Shi, S. Shin, B. Xu, J. Shiomi, S. Graham, and T. Suga, "High thermal boundary conductance across bonded heterogeneous gan-sic interfaces," *ACS applied materials & interfaces*, vol. 11, no. 36, pp. 33428–33434, 2019.
- [81] H. Li, R. Hanus, C. A. Polanco, A. Zeidler, G. Koblmüller, Y. K. Koh, and L. Lindsay, "Gan thermal transport limited by the interplay of dislocations and size effects," *Phys. Rev. B*, vol. 102, no. 1, p. 014313, 2020.
- [82] L. Lindsay, D. Broido, and T. Reinecke, "Thermal conductivity and large isotope effect in gan from first principles," *Physical review letters*, vol. 109, no. 9, p. 095901, 2012.
- [83] L. Lindsay, D. Broido, and T. Reinecke, "Ab Initio thermal transport in compound semiconductors," *Phys. Rev. B*, vol. 87, no. 16, p. 165201, 2013.
- [84] R. Wilson and D. G. Cahill, "Limits to fourier theory in high thermal conductivity single crystals," *Appl. Phys. Lett.*, vol. 107, no. 20, p. 203112, 2015.

- [85] W. Zheng, B. Huang, and Y. K. Koh, "Ultralow thermal conductivity and thermal diffusivity of graphene/metal heterostructures through scarcity of low-energy modes in graphene," *ACS applied materials & interfaces*, vol. 12, no. 8, pp. 9572–9579, 2020.
- [86] A. Giri, A. Z. Chen, A. Mattoni, K. Aryana, D. Zhang, X. Hu, S.-H. Lee, J. J. Choi, and P. E. Hopkins, "Ultralow thermal conductivity of two-dimensional metal halide perovskites," *Nano Letters*, 2020.
- [87] Y. R. Koh, J. Shi, B. Wang, R. Hu, H. Ahmad, S. Kerdsonpanya, E. Milosevic, W. A. Doolittle, D. Gall, Z. Tian, *et al.*, "Thermal boundary conductance across epitaxial metal/sapphire interfaces," *Physical Review B*, vol. 102, no. 20, p. 205304, 2020.
- [88] W. Fulkerson, J. Moore, R. Williams, R. Graves, and D. McElroy, "Thermal conductivity, electrical resistivity, and seebeck coefficient of silicon from 100 to 1300 k," *Physical Review*, vol. 167, no. 3, p. 765, 1968.
- [89] D. Florescu, V. Asnin, F. H. Pollak, R. Molnar, and C. Wood, "High spatial resolution thermal conductivity and raman spectroscopy investigation of hydride vapor phase epitaxy grown n-gan/sapphire (0001): Doping dependence," *Journal of Applied Physics*, vol. 88, no. 6, pp. 3295–3300, 2000.
- [90] D. G. Cahill, S.-M. Lee, and T. I. Selinder, "Thermal conductivity of  $\kappa$ -al<sub>2</sub>o<sub>3</sub> and  $\alpha$ -al<sub>2</sub>o<sub>3</sub> wear-resistant coatings," *Journal of applied physics*, vol. 83, no. 11, pp. 5783–5786, 1998.
- [91] Y. Dong, B.-Y. Cao, and Z.-Y. Guo, "Ballistic–diffusive phonon transport and size induced anisotropy of thermal conductivity of silicon nanofilms," *Physica E: Low-dimensional Systems and Nanostructures*, vol. 66, pp. 1–6, 2015.
- [92] D. G. Cahill, "Thermal conductivity measurement from 30 to 750 k: the  $3\omega$  method," *Review of scientific instruments*, vol. 61, no. 2, pp. 802–808, 1990.
- [93] R. S. Prasher, J.-Y. Chang, I. Sauciuc, S. Narasimhan, D. Chau, G. Chrysler, A. Myers, S. Prstic, and C. Hu, "Nano and micro technology-based next-generation package-level cooling solutions.," *Intel Technol. J.*, vol. 9, no. 4, pp. 285–296, 2005.
- [94] V. Semenyuk, "Thermoelectrics handbook: Macro to nano," by *DM Rowe (CRC Taylor and Francis, Boca Raton, 2006)*, pp. 58–1–58–20, 2006.
- [95] E. Pop, S. Sinha, and K. E. Goodson, "Heat generation and transport in nanometer-scale transistors," *Proc. IEEE*, vol. 94, no. 8, pp. 1587–1601, 2006.
- [96] A. L. Moore and L. Shi, "Emerging challenges and materials for thermal management of electronics," *Mater. Today*, vol. 17, no. 4, pp. 163–174, 2014.

- [97] Y. Fu, J. Hansson, Y. Liu, S. Chen, A. Zehri, M. K. Samani, N. Wang, Y. Ni, Y. Zhang, Z.-B. Zhang, Q. Wang, M. Li, H. Lu, M. Sledzinska, C. M. S. Torres, S. Volz, A. A. Balandin, X. Xu, and J. Liu, “Graphene related materials for thermal management,” *2D Mater.*, vol. 7, no. 1, p. 012001, 2019.
- [98] S. K. Oh, J. S. Lundh, S. Shervin, B. Chatterjee, D. K. Lee, S. Choi, J. S. Kwak, and J.-H. Ryou, “Thermal management and characterization of high-power wide-bandgap semiconductor electronic and photonic devices in automotive applications,” *J. Electron. Packag.*, vol. 141, no. 2, p. 020801, 2019.
- [99] Z. He, Y. Yan, and Z. Zhang, “Thermal management and temperature uniformity enhancement of electronic devices by micro heat sinks: A review,” *Energy*, vol. 216, p. 119223, 2021.
- [100] R. Mahajan, C.-p. Chiu, and G. Chrysler, “Cooling a microprocessor chip,” *Proc. IEEE*, vol. 94, no. 8, pp. 1476–1486, 2006.
- [101] K. Tu, “Reliability challenges in 3d ic packaging technology,” *Microelectron. Reliab.*, vol. 51, no. 3, pp. 517–523, 2011.
- [102] I. Chowdhury, R. Prasher, K. Lofgreen, G. Chrysler, S. Narasimhan, R. Mahajan, D. Koester, R. Alley, and R. Venkatasubramanian, “On-chip cooling by superlattice-based thin-film thermoelectrics,” *Nat. Nanotechnol.*, vol. 4, no. 4, p. 235, 2009.
- [103] V. Sahu, Y. K. Joshi, and A. G. Fedorov, “Hybrid solid state/fluidic cooling for hot spot removal,” *Nanoscale Microscale Thermophys. Eng.*, vol. 13, no. 3, pp. 135–150, 2009.
- [104] A. F. Al-Neama, N. Kapur, J. Summers, and H. M. Thompson, “Thermal management of gan hemt devices using serpentine minichannel heat sinks,” *Appl. Therm. Eng.*, vol. 140, pp. 622–636, 2018.
- [105] A. Giri and P. E. Hopkins, “Achieving a better heat conductor,” *Nat. Mater.*, vol. 19, no. 5, pp. 482–484, 2020.
- [106] A. Bar-Cohen and P. Wang, “On-chip hot spot remediation with miniaturized thermoelectric coolers,” *Microgravity Sci. Technol.*, vol. 21, no. 1, pp. 351–359, 2009.
- [107] D. Choi, N. Poudel, S. B. Cronin, and L. Shi, “Effects of basal-plane thermal conductivity and interface thermal conductance on the hot spot temperature in graphene electronic devices,” *Appl. Phys. Lett.*, vol. 110, no. 7, p. 073104, 2017.
- [108] Q. Zheng, S. Li, C. Li, Y. Lv, X. Liu, P. Y. Huang, D. A. Broido, B. Lv, and D. G. Cahill, “High thermal conductivity in isotopically enriched cubic boron phosphide,” *Adv. Funct. Mater.*, vol. 28, no. 43, p. 1805116, 2018.
- [109] D. Morelli, C. Beetz, and T. Perry, “Thermal conductivity of synthetic diamond films,” *J. Appl. Phys.*, vol. 64, no. 6, pp. 3063–3066, 1988.

- [110] T. Anthony, J. Fleischer, J. Olson, and D. G. Cahill, "The thermal conductivity of isotopically enriched polycrystalline diamond films," *J. Appl. Phys.*, vol. 69, no. 12, pp. 8122–8125, 1991.
- [111] S. Li, Q. Zheng, Y. Lv, X. Liu, X. Wang, P. Y. Huang, D. G. Cahill, and B. Lv, "High thermal conductivity in cubic boron arsenide crystals," *Science*, vol. 361, no. 6402, pp. 579–581, 2018.
- [112] K. Chen, B. Song, N. K. Ravichandran, Q. Zheng, X. Chen, H. Lee, H. Sun, S. Li, G. A. G. Udalamatta Gamage, F. Tian, *et al.*, "Ultrahigh thermal conductivity in isotope-enriched cubic boron nitride," *Science*, vol. 367, no. 6477, pp. 555–559, 2020.
- [113] Z. Yan, G. Liu, J. M. Khan, and A. A. Balandin, "Graphene quilts for thermal management of high-power gan transistors," *Nat. Commun.*, vol. 3, no. 1, pp. 1–8, 2012.
- [114] G. A. Slack, "Nonmetallic crystals with high thermal conductivity," *Journal of Physics and Chemistry of Solids*, vol. 34, no. 2, pp. 321–335, 1973.
- [115] F. Miyashiro, N. Iwase, A. Tsuge, F. Ueno, M. Nakahashi, and T. Takahashi, "High thermal conductivity aluminum nitride ceramic substrates and packages," *IEEE Trans. Compon., Hybrids, Manuf. Technol.*, vol. 13, no. 2, pp. 313–319, 1990.
- [116] A. Jeżowski, B. Danilchenko, M. Boćkowski, I. Grzegory, S. Krukowski, T. Suski, and T. Paszkiewicz, "Thermal conductivity of gan crystals in 4.2–300 k range," *Solid State Commun.*, vol. 128, no. 2-3, pp. 69–73, 2003.
- [117] F. Kawamura, T. Iwahashi, M. Morishita, K. Omae, M. Yoshimura, Y. Mori, and T. Sasaki, "Growth of transparent, large size gan single crystal with low dislocations using ca-na flux system," *Jpn. J. Appl. Phys.*, vol. 42, no. 7A, p. L729, 2003.
- [118] Y. Xiong, Z. Fu, Y. Wang, and Q. Feng, "Fabrication of transparent aln ceramics," *J. Mater. Sci.*, vol. 41, no. 8, pp. 2537–2539, 2006.
- [119] M. S. Tareq, S. Zainuddin, E. Woodside, and F. Syed, "Investigation of the flexural and thermomechanical properties of nanoclay/graphene reinforced carbon fiber epoxy composites," *J. Mater. Res.*, vol. 34, no. 21, pp. 3678–3687, 2019.
- [120] P. Kuo, G. Auner, and Z. Wu, "Microstructure and thermal conductivity of epitaxial aln thin films," *Thin Solid Films*, vol. 253, no. 1-2, pp. 223–227, 1994.
- [121] Y. Zhao, C. Zhu, S. Wang, J. Tian, D. Yang, C. Chen, H. Cheng, and P. Hing, "Pulsed photothermal reflectance measurement of the thermal conductivity of sputtered aluminum nitride thin films," *J. Appl. Phys.*, vol. 96, no. 8, pp. 4563–4568, 2004.
- [122] S. R. Choi, D. Kim, S.-H. Choa, S.-H. Lee, and J.-K. Kim, "Thermal conductivity of aln and sic thin films," *Int. J. Thermophys.*, vol. 27, no. 3, pp. 896–905, 2006.

- [123] M. Kazan, S. Pereira, M. Correia, and P. Masri, "Contribution of the decay of optical phonons into acoustic phonons to the thermal conductivity of aln," *Phys. Rev. B*, vol. 77, no. 18, p. 180302, 2008.
- [124] A. AlShaikhi and G. Srivastava, "Thermal conductivity of single crystal and ceramic aln," *J. Appl. Phys.*, vol. 103, no. 8, p. 083554, 2008.
- [125] C. Duquenne, M.-P. Besland, P. Tessier, E. Gautron, Y. Scudeller, and D. Averty, "Thermal conductivity of aluminium nitride thin films prepared by reactive magnetron sputtering," *J. Phys. D: Appl. Phys.*, vol. 45, no. 1, p. 015301, 2011.
- [126] R. Rounds, B. Sarkar, A. Klump, C. Hartmann, T. Nagashima, R. Kirste, A. Franke, M. Bickermann, Y. Kumagai, Z. Sitar, and R. Collazo, "Thermal conductivity of single-crystalline aln," *Appl. Phys. Express*, vol. 11, no. 7, p. 071001, 2018.
- [127] R. L. Xu, M. Muñoz Rojo, S. Islam, A. Sood, B. Vareskic, A. Katre, N. Mingo, K. E. Goodson, H. G. Xing, D. Jena, and E. Pop, "Thermal conductivity of crystalline aln and the influence of atomic-scale defects," *J. Appl. Phys.*, vol. 126, no. 18, p. 185105, 2019.
- [128] Z. Cheng, Y. R. Koh, A. Mamun, J. Shi, T. Bai, K. Huynh, L. Yates, Z. Liu, R. Li, E. Lee, *et al.*, "Experimental observation of high intrinsic thermal conductivity of aln," *Physical Review Materials*, vol. 4, no. 4, p. 044602, 2020.
- [129] C. J. Gomes, M. Madrid, J. V. Goicochea, and C. H. Amon, "In-plane and out-of-plane thermal conductivity of silicon thin films predicted by molecular dynamics," *J. Heat Transfer*, vol. 128, no. 11, pp. 1114–1121, 2006.
- [130] C. Jeong, S. Datta, and M. Lundstrom, "Thermal conductivity of bulk and thin-film silicon: A landauer approach," *J. Appl. Phys.*, vol. 111, no. 9, p. 093708, 2012.
- [131] S. Kwon, J. Zheng, M. C. Wingert, S. Cui, and R. Chen, "Unusually high and anisotropic thermal conductivity in amorphous silicon nanostructures," *ACS nano*, vol. 11, no. 3, pp. 2470–2476, 2017.
- [132] G. Slack and T. McNelly, "Aln single crystals," *J. Cryst. Growth*, vol. 42, pp. 560–563, 1977.
- [133] P. D. Dapkus, "Metalorganic chemical vapor deposition," *Annu. Rev. Mater. Sci.*, vol. 12, no. 1, pp. 243–269, 1982.
- [134] E. Gastellóu, G. García, A. Herrera, C. Morales, R. García, G. Hirata, M. Robles, J. Rodríguez, and I. García, "A brief review of growth techniques for obtaining of iii-v semiconductor compounds," *Eur. J. Eng. Res. Sci.*, vol. 4, no. 9, pp. 17–21, 2019.
- [135] Y. Touloukian, R. Powell, C. Ho, and P. Klemens, "Thermal conductivity: Non-metallic solids volume 2 of thermophysical properties of matter eds ys touloukian," *CY Ho (New York: IFI/Plenum) pp*, pp. 182–193, (1970).

- [136] R. Wilson and D. G. Cahill, “Anisotropic failure of fourier theory in time-domain thermoreflectance experiments,” *Nat. Commun.*, vol. 5, p. 5075, 2014.
- [137] A. J. Minnich, J. Johnson, A. Schmidt, K. Esfarjani, M. Dresselhaus, K. A. Nelson, and G. Chen, “Thermal conductivity spectroscopy technique to measure phonon mean free paths,” *Phys. Rev. Lett.*, vol. 107, no. 9, p. 095901, 2011.
- [138] K. T. Regner, D. P. Sellan, Z. Su, C. H. Amon, A. J. McGaughey, and J. A. Malen, “Broadband phonon mean free path contributions to thermal conductivity measured using frequency domain thermoreflectance,” *Nat. Commun.*, vol. 4, p. 1640, 2013.
- [139] R. Wilson, J. P. Feser, G. T. Hohensee, and D. G. Cahill, “Two-channel model for nonequilibrium thermal transport in pump-probe experiments,” *Phys. Rev. B*, vol. 88, no. 14, p. 144305, 2013.
- [140] K. Regner, L. Wei, and J. Malen, “Interpretation of thermoreflectance measurements with a two-temperature model including non-surface heat deposition,” *J. Appl. Phys.*, vol. 118, no. 23, p. 235101, 2015.
- [141] L. Chen, J. L. Braun, B. F. Donovan, P. E. Hopkins, and S. J. Poon, “Ballistic transport of long wavelength phonons and thermal conductivity accumulation in nanograined silicon-germanium alloys,” *Appl. Phys. Lett.*, vol. 111, no. 13, p. 131902, 2017.
- [142] Z. Cheng, Y. R. Koh, H. Ahmad, R. Hu, J. Shi, M. E. Liao, Y. Wang, T. Bai, R. Li, E. Lee, E. A. Clinton, C. M. Matthews, Z. Engel, L. Yates, T. Luo, M. S. Goorsky, W. A. Doolittle, Z. Tian, P. E. Hopkins, and S. Graham, “Thermal conductance across harmonic-matched epitaxial al-sapphire heterointerfaces,” *Commun. Phys.*, vol. 3, no. 1, pp. 1–8, 2020.
- [143] J. Graebner, J. Mucha, L. Seibles, and G. Kammlott, “The thermal conductivity of chemical-vapor-deposited diamond films on silicon,” *J. Appl. Phys.*, vol. 71, no. 7, pp. 3143–3146, 1992.
- [144] J. Graebner, S. Jin, G. Kammlott, J. Herb, and C. Gardinier, “Unusually high thermal conductivity in diamond films,” *Appl. Phys. Lett.*, vol. 60, no. 13, pp. 1576–1578, 1992.
- [145] K. Plamann, D. Fournier, E. Anger, and A. Gicquel, “Photothermal examination of the heat diffusion inhomogeneity in diamond films of sub-micron thickness,” *Diamond Relat. Mater.*, vol. 3, no. 4-6, pp. 752–756, 1994.
- [146] H. Verhoeven, A. Flöter, H. Reiß, R. Zachai, D. Wittorf, and W. Jäger, “Influence of the microstructure on the thermal properties of thin polycrystalline diamond films,” *Appl. Phys. Lett.*, vol. 71, no. 10, pp. 1329–1331, 1997.
- [147] B. Lee, J. S. Lee, S. U. Kim, K. Kim, O. Kwon, S. Lee, J. H. Kim, and D. S. Lim, “Simultaneous measurement of thermal conductivity and interface thermal conductance

- of diamond thin film,” *J. Vac. Sci. Technol., B: Microelectron. Nanometer Struct.–Process., Meas., Phenom.*, vol. 27, no. 6, pp. 2408–2412, 2009.
- [148] S. Rossi, M. Alomari, Y. Zhang, S. Bychikhin, D. Pogany, J. Weaver, and E. Kohn, “Thermal analysis of submicron nanocrystalline diamond films,” *Diamond Relat. Mater.*, vol. 40, pp. 69–74, 2013.
- [149] J. Anaya, S. Rossi, M. Alomari, E. Kohn, L. Tóth, B. Pécz, and M. Kuball, “Thermal conductivity of ultrathin nano-crystalline diamond films determined by raman thermography assisted by silicon nanowires,” *Appl. Phys. Lett.*, vol. 106, no. 22, p. 223101, 2015.
- [150] J. Anaya, S. Rossi, M. Alomari, E. Kohn, L. Tóth, B. Pécz, K. D. Hobart, T. J. Anderson, T. I. Feygelson, B. B. Pate, and M. Kuball, “Control of the in-plane thermal conductivity of ultra-thin nanocrystalline diamond films through the grain and grain boundary properties,” *Acta Mater.*, vol. 103, pp. 141–152, 2016.
- [151] Y. Tai, C. Mastrangelo, and R. Muller, “Thermal conductivity of heavily doped low-pressure chemical vapor deposited polycrystalline silicon films,” *J. Appl. Phys.*, vol. 63, no. 5, pp. 1442–1447, 1988.
- [152] M. Asheghi, M. Touzelbaev, K. Goodson, Y. Leung, and S. Wong, “Temperature-dependent thermal conductivity of single-crystal silicon layers in soi substrates,” *J. Heat Transfer*, vol. 120, no. 1, pp. 30–36, 1998.
- [153] Y. Ju and K. Goodson, “Phonon scattering in silicon films with thickness of order 100 nm,” *Appl. Phys. Lett.*, vol. 74, no. 20, pp. 3005–3007, 1999.
- [154] W. Liu and M. Asheghi, “Phonon–boundary scattering in ultrathin single-crystal silicon layers,” *Appl. Phys. Lett.*, vol. 84, no. 19, pp. 3819–3821, 2004.
- [155] Q. Zheng, P. V. Braun, and D. G. Cahill, “Thermal conductivity of graphite thin films grown by low temperature chemical vapor deposition on ni (111),” *Adv. Mater. Interfaces*, vol. 3, no. 16, p. 1600234, 2016.
- [156] H. Zhang, X. Chen, Y.-D. Jho, and A. J. Minnich, “Temperature-dependent mean free path spectra of thermal phonons along the *c*-axis of graphite,” *Nano Lett.*, vol. 16, no. 3, pp. 1643–1649, 2016.
- [157] M. Alam, M. Bresnehan, J. A. Robinson, and M. A. Haque, “Thermal conductivity of ultra-thin chemical vapor deposited hexagonal boron nitride films,” *Appl. Phys. Lett.*, vol. 104, no. 1, p. 013113, 2014.
- [158] K. Pratik, A. Rai, T. S. Ashton, and A. L. Moore, “Apcvd hexagonal boron nitride thin films for passive near-junction thermal management of electronics,” *Nanotechnology*, vol. 28, no. 50, p. 505705, 2017.

- [159] C. Yuan, J. Li, L. Lindsay, D. Cherns, J. W. Pomeroy, S. Liu, J. H. Edgar, and M. Kuball, “Modulating the thermal conductivity in hexagonal boron nitride *via* controlled boron isotope concentration,” *Commun. Phys.*, vol. 2, no. 1, pp. 1–8, 2019.
- [160] C. L. Julian, “Theory of heat conduction in rare-gas crystals,” *Phys. Rev.*, vol. 137, no. 1A, p. A128, 1965.
- [161] E. Steigmeier and I. Kudman, “Thermal conductivity of iii-v compounds at high temperatures,” *Phys. Rev.*, vol. 132, no. 2, p. 508, 1963.
- [162] G. A. Slack, “Thermal conductivity of ii-vi compounds and phonon scattering by  $fe^{2+}$  impurities,” *Phys. Rev. B*, vol. 6, no. 10, p. 3791, 1972.
- [163] A. Inyushkin, A. Taldenkov, A. Y. Yakubovsky, A. Markov, L. Moreno-Garsia, and B. Sharonov, “Thermal conductivity of isotopically enriched  $^{71}Ga$  crystal,” *Semicond. Sci. Technol.*, vol. 18, no. 7, p. 685, 2003.
- [164] M. A. Afromowitz, “Thermal conductivity of  $ga_{1-x}al_x$  alloys,” *J. Appl. Phys.*, vol. 44, no. 3, pp. 1292–1294, 1973.
- [165] V. Ozhogin, A. Inyushkin, A. Taldenkov, A. Tikhomirov, G. Popov, E. Haller, and K. Itoh, “Isotope effect in the thermal conductivity of germanium single crystals,” *J. Exp. Theor. Phys. Lett.*, vol. 63, no. 6, pp. 490–494, 1996.
- [166] H. Shibata, Y. Waseda, H. Ohta, K. Kiyomi, K. Shimoyama, K. Fujito, H. Nagaoka, Y. Kagamitani, R. Simura, and T. Fukuda, “High thermal conductivity of gallium nitride (gan) crystals grown by hve process,” *Materials Transactions*, vol. 48, no. 10, pp. 2782–2786, 2007.
- [167] A. Inyushkin, A. Taldenkov, A. Gibin, A. Gusev, and H.-J. Pohl, “On the isotope effect in thermal conductivity of silicon,” *Phys. Status Solidi C*, vol. 1, no. 11, pp. 2995–2998, 2004.
- [168] T. Anthony, W. Banholzer, J. F. Fleischer, L. Wei, P. Kuo, R. Thomas, and R. Pryor, “Thermal diffusivity of isotopically enriched  $^{12}C$  diamond,” *Phys. Rev. B*, vol. 42, no. 2, p. 1104, 1990.
- [169] S. Nakamura, D. Miyafuji, T. Fujii, T. Matsui, and H. Fukuyama, “Low temperature transport properties of pyrolytic graphite sheet,” *Cryogenics*, vol. 86, pp. 118–122, 2017.
- [170] T. Nihira and T. Iwata, “Thermal resistivity changes in electron-irradiated pyrolytic graphite,” *Jpn. J. Appl. Phys.*, vol. 14, no. 8, p. 1099, 1975.
- [171] B. Sun, X. Gu, Q. Zeng, X. Huang, Y. Yan, Z. Liu, R. Yang, and Y. K. Koh, “Temperature dependence of anisotropic thermal-conductivity tensor of bulk black phosphorus,” *Adv. Mater.*, vol. 29, no. 3, p. 1603297, 2017.

- [172] P. Jiang, L. Lindsay, and Y. K. Koh, "Role of low-energy phonons with mean-free-paths  $> 0.8 \mu\text{m}$  in heat conduction in silicon," *J. Appl. Phys.*, vol. 119, no. 24, p. 245705, 2016.
- [173] P. Jiang, L. Lindsay, X. Huang, and Y. K. Koh, "Interfacial phonon scattering and transmission loss in  $> 1 \mu\text{m}$  thick silicon-on-insulator thin films," *Phys. Rev. B*, vol. 97, no. 19, p. 195308, 2018.
- [174] B. Yang, W. Liu, J. Liu, K. Wang, and G. Chen, "Measurements of anisotropic thermoelectric properties in superlattices," *Appl. Phys. Lett.*, vol. 81, no. 19, pp. 3588–3590, 2002.
- [175] B. Sun, G. Haunschild, C. Polanco, J. Z.-J. Ju, L. Lindsay, G. Koblmüller, and Y. K. Koh, "Dislocation-induced thermal transport anisotropy in single-crystal group-iii nitride films," *Nat. Mater.*, vol. 18, no. 2, pp. 136–140, 2019.
- [176] A. Majumdar, "Microscale heat conduction in dielectric thin films," 1993.
- [177] B. Yang and G. Chen, "Partially coherent phonon heat conduction in superlattices," *Phys. Rev. B*, vol. 67, no. 19, p. 195311, 2003.
- [178] J. Graebner, S. Jin, G. Kammlott, J. Herb, and C. Gardinier, "Large anisotropic thermal conductivity in synthetic diamond films," *Nature*, vol. 359, no. 6394, pp. 401–403, 1992.
- [179] J. Graebner, M. Reiss, L. Seibles, T. Hartnett, R. Miller, and C. Robinson, "Phonon scattering in chemical-vapor-deposited diamond," *Phys. Rev. B*, vol. 50, no. 6, p. 3702, 1994.
- [180] B. F. Donovan, D. M. Long, A. Moballeggh, N. Creange, E. C. Dickey, and P. E. Hopkins, "Impact of intrinsic point defect concentration on thermal transport in titanium dioxide," *Acta Mater.*, vol. 127, pp. 491–497, 2017.
- [181] G. Chen, "Thermal conductivity and ballistic-phonon transport in the cross-plane direction of superlattices," *Phys. Rev. B*, vol. 57, no. 23, p. 14958, 1998.
- [182] K. Aryana, J. Gaskins, J. Nag, J. Read, D. Olson, M. Grobis, and P. Hopkins, "Thermal properties of carbon nitride toward use as an electrode in phase change memory devices," *Applied Physics Letters*, vol. 116, no. 4, p. 043502, 2020.
- [183] M. E. DeCoster, K. E. Meyer, B. D. Piercy, J. T. Gaskins, B. F. Donovan, A. Giri, N. A. Strnad, D. M. Potrepka, A. A. Wilson, M. D. Losego, *et al.*, "Density and size effects on the thermal conductivity of atomic layer deposited  $\text{TiO}_2$  and  $\text{Al}_2\text{O}_3$  thin films," *Thin Solid Films*, vol. 650, pp. 71–77, 2018.
- [184] A. Dameron, D. Seghete, B. Burton, S. Davidson, A. Cavanagh, J. Bertrand, and S. George, "Molecular layer deposition of alucone polymer films using trimethylaluminum and ethylene glycol," *Chemistry of Materials*, vol. 20, no. 10, pp. 3315–3326, 2008.

- [185] J.-H. Han, T.-Y. Kim, D.-Y. Kim, H. L. Yang, and J.-S. Park, "Water vapor and hydrogen gas diffusion barrier characteristics of al<sub>2</sub>o<sub>3</sub>-alucone multi-layer structures for flexible oled display applications," *Dalton Transactions*, vol. 50, no. 43, pp. 15841–15848, 2021.
- [186] Y. Zhao, L. V. Goncharova, Q. Zhang, P. Kaghazchi, Q. Sun, A. Lushington, B. Wang, R. Li, and X. Sun, "Inorganic–organic coating via molecular layer deposition enables long life sodium metal anode," *Nano letters*, vol. 17, no. 9, pp. 5653–5659, 2017.
- [187] K. Kaliyappan, T. Or, Y.-P. Deng, Y. Hu, Z. Bai, and Z. Chen, "Constructing safe and durable high-voltage p<sub>2</sub> layered cathodes for sodium ion batteries enabled by molecular layer deposition of alucone," *Advanced Functional Materials*, vol. 30, no. 17, p. 1910251, 2020.
- [188] M. E. DeCoster, X. Chen, K. Zhang, C. M. Rost, E. R. Hoglund, J. M. Howe, T. E. Beechem, H. Baumgart, and P. E. Hopkins, "Thermal conductivity and phonon scattering processes of ald grown pbte–pbse thermoelectric thin films," *Advanced Functional Materials*, vol. 29, no. 46, p. 1904073, 2019.
- [189] X. Wang, V. Ho, R. A. Segalman, and D. G. Cahill, "Thermal conductivity of high-modulus polymer fibers," *Macromolecules*, vol. 46, no. 12, pp. 4937–4943, 2013.
- [190] X. Xie, D. Li, T.-H. Tsai, J. Liu, P. V. Braun, and D. G. Cahill, "Thermal conductivity, heat capacity, and elastic constants of water-soluble polymers and polymer blends," *Macromolecules*, vol. 49, no. 3, pp. 972–978, 2016.
- [191] X. Xie, K. Yang, D. Li, T.-H. Tsai, J. Shin, P. V. Braun, and D. G. Cahill, "High and low thermal conductivity of amorphous macromolecules," *Physical Review B*, vol. 95, no. 3, p. 035406, 2017.
- [192] G. Lorenzin, M. S. B. Hoque, D. Ariosa, L. P. Jeurgens, E. R. Hoglund, J. A. Tomko, P. E. Hopkins, and C. Cancellieri, "Tensile and compressive stresses in cu/w multilayers: Correlation with microstructure, thermal stability, and thermal conductivity," *Acta Materialia*, vol. 240, p. 118315, 2022.
- [193] C. Cancellieri, E. A. Scott, J. Braun, S. W. King, R. Oviedo, C. Jezewski, J. Richards, F. La Mattina, L. P. Jeurgens, and P. E. Hopkins, "Interface and layer periodicity effects on the thermal conductivity of copper-based nanomultilayers with tungsten, tantalum, and tantalum nitride diffusion barriers," *Journal of Applied Physics*, vol. 128, no. 19, p. 195302, 2020.
- [194] G. K. White and S. Collocott, "Heat capacity of reference materials: Cu and W," *Journal of physical and chemical reference data*, vol. 13, no. 4, pp. 1251–1257, 1984.
- [195] J. Hostetler, A. Smith, and P. Norris, "Thin-film thermal conductivity and thickness measurements using picosecond ultrasonics," *Microscale Thermophysical Engineering*, vol. 1, no. 3, pp. 237–244, 1997.

- [196] E. A. Scott, J. T. Gaskins, S. W. King, and P. E. Hopkins, “Thermal conductivity and thermal boundary resistance of atomic layer deposited high-k dielectric aluminum oxide, hafnium oxide, and titanium oxide thin films on silicon,” *APL Materials*, vol. 6, no. 5, p. 058302, 2018.
- [197] J. Salter and P. Charsley, “The effect of grain size on the lattice thermal conductivity of copper aluminium alloys,” *physica status solidi (b)*, vol. 21, no. 1, pp. 357–368, 1967.
- [198] B. Feng, Z. Li, and X. Zhang, “Effect of grain-boundary scattering on the thermal conductivity of nanocrystalline metallic films,” *Journal of Physics D: Applied Physics*, vol. 42, no. 5, p. 055311, 2009.
- [199] S. Mason, D. Wesenberg, A. Hojem, M. Manno, C. Leighton, and B. Zink, “Violation of the wiedemann-franz law through reduction of thermal conductivity in gold thin films,” *Physical Review Materials*, vol. 4, no. 6, p. 065003, 2020.
- [200] E. Alleno, L. Chen, C. Chubilleau, B. Lenoir, O. Rouleau, M. Trichet, and B. Villeroy, “Thermal conductivity reduction in CoSb<sub>3</sub>-CeO<sub>2</sub> nanocomposites,” *Journal of electronic materials*, vol. 39, no. 9, pp. 1966–1970, 2010.
- [201] T. Shuvra Basu, R. Yang, S. Joottu Thiagarajan, S. Ghosh, S. Gierlotka, and M. Ray, “Remarkable thermal conductivity reduction in metal-semiconductor nanocomposites,” *Applied Physics Letters*, vol. 103, no. 8, p. 083115, 2013.
- [202] Z.-Y. Li, J.-F. Li, W.-Y. Zhao, Q. Tan, T.-R. Wei, C.-F. Wu, and Z.-B. Xing, “PbTe-based thermoelectric nanocomposites with reduced thermal conductivity by sic nanodispersion,” *Applied Physics Letters*, vol. 104, no. 11, p. 113905, 2014.
- [203] M. S. B. Hoque, M. Milich, M. S. Akhanda, S. Shivakumar, E. R. Hoglund, D. Staicu, M. Qin, K. F. Quiambao-Tomko, J. A. Tomko, J. L. Braun, *et al.*, “Thermal and ablation properties of a high-entropy metal diboride:(hf<sub>0.2</sub>zr<sub>0.2</sub>ti<sub>0.2</sub>ta<sub>0.2</sub>nb<sub>0.2</sub>)b<sub>2</sub>,” *Journal of the European Ceramic Society*, 2023.
- [204] D. Bérardan, S. Franger, D. Dragoë, A. K. Meena, and N. Dragoë, “Colossal dielectric constant in high entropy oxides,” *physica status solidi (RRL)–Rapid Research Letters*, vol. 10, no. 4, pp. 328–333, 2016.
- [205] D. Bérardan, S. Franger, A. Meena, and N. Dragoë, “Room temperature lithium superionic conductivity in high entropy oxides,” *Journal of Materials Chemistry A*, vol. 4, no. 24, pp. 9536–9541, 2016.
- [206] M.-H. Tsai and J.-W. Yeh, “High-entropy alloys: a critical review,” *Materials Research Letters*, vol. 2, no. 3, pp. 107–123, 2014.
- [207] Y. Zhang, T. T. Zuo, Z. Tang, M. C. Gao, K. A. Dahmen, P. K. Liaw, and Z. P. Lu, “Microstructures and properties of high-entropy alloys,” *Progress in materials science*, vol. 61, pp. 1–93, 2014.

- [208] T. Jin, X. Sang, R. R. Unocic, R. T. Kinch, X. Liu, J. Hu, H. Liu, and S. Dai, “Mechanochemical-assisted synthesis of high-entropy metal nitride via a soft urea strategy,” *Advanced materials*, vol. 30, no. 23, p. 1707512, 2018.
- [209] T. Zhu, P. M. Litwin, M. G. Rosul, D. Jessup, M. S. Akhanda, F. F. Tonni, S. Krylyuk, A. V. Davydov, P. Reinke, S. J. McDonnell, and M. Zebarjadi, “Transport properties of few-layer nbse<sub>2</sub>: From electronic structure to thermoelectric properties,” *Materials Today Physics*, vol. 27, p. 100789, 2022.
- [210] M. B. Burkholder, M. M. Rahman, A. C. Reber, A. M. Gaffney, B. F. Gupton, and J. R. Monnier, “New perspectives and insights into direct epoxidation of propylene using o<sub>2</sub> and silver-based catalysts,” *Applied Catalysis A: General*, vol. 650, p. 119002, 2023.
- [211] J. Gild, Y. Zhang, T. Harrington, S. Jiang, T. Hu, M. C. Quinn, W. M. Mellor, N. Zhou, K. Vecchio, and J. Luo, “High-entropy metal diborides: a new class of high-entropy materials and a new type of ultrahigh temperature ceramics,” *Scientific reports*, vol. 6, no. 1, pp. 1–10, 2016.
- [212] J. Gild, A. Wright, K. Quiambao-Tomko, M. Qin, J. A. Tomko, M. S. bin Hoque, J. L. Braun, B. Bloomfield, D. Martinez, T. Harrington, K. Vecchio, P. E. Hopkins, and J. Luo, “Thermal conductivity and hardness of three single-phase high-entropy metal diborides fabricated by borocarbothermal reduction and spark plasma sintering,” *Ceramics International*, vol. 46, no. 5, pp. 6906–6913, 2020.
- [213] X. Yan, L. Constantin, Y. Lu, J.-F. Silvain, M. Nastasi, and B. Cui, “(hf<sub>0</sub>. 2zr<sub>0</sub>. 2ta<sub>0</sub>. 2nb<sub>0</sub>. 2ti<sub>0</sub>. 2) c high-entropy ceramics with low thermal conductivity,” *Journal of the American Ceramic Society*, vol. 101, no. 10, pp. 4486–4491, 2018.
- [214] J. Zhou, J. Zhang, F. Zhang, B. Niu, L. Lei, and W. Wang, “High-entropy carbide: A novel class of multicomponent ceramics,” *Ceramics International*, vol. 44, no. 17, pp. 22014–22018, 2018.
- [215] P. Sarker, T. Harrington, C. Toher, C. Oses, M. Samiee, J.-P. Maria, D. W. Brenner, K. S. Vecchio, and S. Curtarolo, “High-entropy high-hardness metal carbides discovered by entropy descriptors,” *Nature communications*, vol. 9, no. 1, pp. 1–10, 2018.
- [216] E. Castle, T. Csanádi, S. Grasso, J. Dusza, and M. Reece, “Processing and properties of high-entropy ultra-high temperature carbides,” *Scientific reports*, vol. 8, no. 1, pp. 1–12, 2018.
- [217] T. J. Harrington, J. Gild, P. Sarker, C. Toher, C. M. Rost, O. F. Dippo, C. McElfresh, K. Kaufmann, E. Marin, L. Borowski, P. E. . Hopkins, J. Luo, S. Curtarolo, D. W. Brenner, and K. S. Vecchio, “Phase stability and mechanical properties of novel high entropy transition metal carbides,” *Acta Materialia*, vol. 166, pp. 271–280, 2019.

- [218] M. S. Akhanda, S. E. Rezaei, K. Esfarjani, S. Krylyuk, A. V. Davydov, and M. Zebarjadi, "Thermomagnetic properties of  $\text{Bi}_2\text{Te}_3$  single crystal in the temperature range from 55 K to 380 K," *Physical review materials*, vol. 5, no. 1, p. 015403, 2021.
- [219] V. Braic, A. Vladescu, M. Balaceanu, C. Luculescu, and M. Braic, "Nanostructured multi-element (TiZrNbHfTa)N and (TiZrNbHfTa)C hard coatings," *Surface and Coatings Technology*, vol. 211, pp. 117–121, 2012.
- [220] R.-Z. Zhang, F. Gucci, H. Zhu, K. Chen, and M. J. Reece, "Data-driven design of ecofriendly thermoelectric high-entropy sulfides," *Inorganic chemistry*, vol. 57, no. 20, pp. 13027–13033, 2018.
- [221] J. Gild, J. Braun, K. Kaufmann, E. Marin, T. Harrington, P. Hopkins, K. Vecchio, and J. Luo, "A high-entropy silicide:  $(\text{Mo}_{0.2}\text{Nb}_{0.2}\text{Ta}_{0.2}\text{Ti}_{0.2}\text{W}_{0.2})\text{Si}_2$ ," *Journal of Materials*, vol. 5, no. 3, pp. 337–343, 2019.
- [222] Y. Qin, J.-X. Liu, F. Li, X. Wei, H. Wu, and G.-J. Zhang, "A high entropy silicide by reactive spark plasma sintering," *Journal of Advanced Ceramics*, vol. 8, no. 1, pp. 148–152, 2019.
- [223] J. Gild, M. Samiee, J. L. Braun, T. Harrington, H. Vega, P. E. Hopkins, K. Vecchio, and J. Luo, "High-entropy fluorite oxides," *Journal of the European Ceramic Society*, vol. 38, no. 10, pp. 3578–3584, 2018.
- [224] D. Song, M. Ryu, J. Kwon, G. Lyu, J. Kim, H.-B. Jeon, T. Song, U. Paik, B.-i. Yang, Y.-G. Jung, and Y.-S. Oh, "Blocking of radiative thermal conduction in  $\text{Zn}_2$ -incorporated high-entropy  $\text{A}_2\text{B}_2\text{O}_7$  fluorite oxides," *Ceramics International*, vol. 47, no. 23, pp. 33544–33553, 2021.
- [225] R. Djenadic, A. Sarkar, O. Clemens, C. Loho, M. Botros, V. S. Chakravadhanula, C. Kübel, S. S. Bhattacharya, A. S. Gandhi, and H. Hahn, "Multicomponent equiatomic rare earth oxides," *Materials Research Letters*, vol. 5, no. 2, pp. 102–109, 2017.
- [226] J. Dąbrowa, M. Stygar, A. Mikuła, A. Knapik, K. Mroczka, W. Tejchman, M. Danielewski, and M. Martin, "Synthesis and microstructure of the (Co, Cr, Fe, Mn, Ni) $_3\text{O}_4$  high entropy oxide characterized by spinel structure," *Materials Letters*, vol. 216, pp. 32–36, 2018.
- [227] S. Jiang, T. Hu, J. Gild, N. Zhou, J. Nie, M. Qin, T. Harrington, K. Vecchio, and J. Luo, "A new class of high-entropy perovskite oxides," *Scripta Materialia*, vol. 142, pp. 116–120, 2018.
- [228] Y. Sharma, B. L. Musico, X. Gao, C. Hua, A. F. May, A. Herklotz, A. Rastogi, D. Mandrus, J. Yan, H. N. Lee, M. F. Chisholm, V. Keppens, and T. Z. Ward, "Single-crystal high entropy perovskite oxide epitaxial films," *Physical Review Materials*, vol. 2, no. 6, p. 060404, 2018.

- [229] D. Vinnik, E. Trofimov, V. Zhivulin, O. Zaitseva, S. Gudkova, A. Y. Starikov, D. Zherebtsov, A. Kirsanova, M. Häßner, and R. Niewa, “High-entropy oxide phases with magnetoplumbite structure,” *Ceramics International*, vol. 45, no. 10, pp. 12942–12948, 2019.
- [230] E. R. Hoglund, D.-L. Bao, A. O’Hara, S. Makarem, Z. T. Piontkowski, J. R. Matson, A. K. Yadav, R. C. Haislmaier, R. Engel-Herbert, J. F. Ihlefeld, *et al.*, “Emergent interface vibrational structure of oxide superlattices,” *Nature*, vol. 601, no. 7894, pp. 556–561, 2022.
- [231] E. R. Hoglund, D.-L. Bao, A. O’Hara, T. W. Pfeifer, M. S. B. Hoque, S. Makarem, J. M. Howe, S. T. Pantelides, P. E. Hopkins, and J. A. Hachtel, “Direct visualization of localized vibrations at complex grain boundaries,” *Advanced Materials*, p. 2208920, 2023.
- [232] W. G. Fahrenholtz and G. E. Hilmas, “Ultra-high temperature ceramics: materials for extreme environments,” *Scripta materialia*, vol. 129, pp. 94–99, 2017.
- [233] D. Marshall, B. Cox, P. Kroll, G. Hilmas, W. Fahrenholtz, R. Raj, R. Ritchie, Q. Yang, and F. Zok, “National hypersonic science center for materials and structures,” tech. rep., TELEDYNE SCIENTIFIC COMPANY THOUSAND OAKS CA, 2014.
- [234] W. G. Fahrenholtz, E. J. Wuchina, W. E. Lee, and Y. Zhou, *Ultra-high temperature ceramics: materials for extreme environment applications*. John Wiley & Sons, 2014.
- [235] N. P. Padture, “Advanced structural ceramics in aerospace propulsion,” *Nature materials*, vol. 15, no. 8, pp. 804–809, 2016.
- [236] S. Akrami, P. Edalati, M. Fuji, and K. Edalati, “High-entropy ceramics: Review of principles, production and applications,” *Materials Science and Engineering: R: Reports*, vol. 146, p. 100644, 2021.
- [237] H. Xiang, Y. Xing, F.-z. Dai, H. Wang, L. Su, L. Miao, G. Zhang, Y. Wang, X. Qi, L. Yao, H. Wang, B. Zhao, J. Li, and Y. Zhou, “High-entropy ceramics: Present status, challenges, and a look forward,” *Journal of Advanced Ceramics*, vol. 10, no. 3, pp. 385–441, 2021.
- [238] W. G. Fahrenholtz, G. E. Hilmas, I. G. Talmy, and J. A. Zaykoski, “Refractory diborides of zirconium and hafnium,” *Journal of the American Ceramic Society*, vol. 90, no. 5, pp. 1347–1364, 2007.
- [239] M. Qin, J. Gild, C. Hu, H. Wang, M. S. B. Hoque, J. L. Braun, T. J. Harrington, P. E. Hopkins, K. S. Vecchio, and J. Luo, “Dual-phase high-entropy ultra-high temperature ceramics,” *Journal of the European Ceramic Society*, vol. 40, no. 15, pp. 5037–5050, 2020.

- [240] W. Parker, R. Jenkins, C. Butler, and G. Abbott, "Flash method of determining thermal diffusivity, heat capacity, and thermal conductivity," *Journal of applied physics*, vol. 32, no. 9, pp. 1679–1684, 1961.
- [241] Y. R. Koh, M. S. B. Hoque, H. Ahmad, D. H. Olson, Z. Liu, J. Shi, Y. Wang, K. Huynh, E. R. Hoglund, K. Aryana, J. M. Howe, M. S. Goorsky, S. Graham, T. Luo, and J. K. Hite, "High thermal conductivity and thermal boundary conductance of homoepitaxially grown gallium nitride (gan) thin films," *Physical Review Materials*, vol. 5, no. 10, p. 104604, 2021.
- [242] M. Gasch, S. Johnson, and J. Marschall, "Thermal conductivity characterization of hafnium diboride-based ultra-high-temperature ceramics," *J. Am. Ceram. Soc.*, vol. 91, no. 5, pp. 1423–1432, (2008).
- [243] J. Justin and A. Jankowiak, "Ultra high temperature ceramics: Densification, properties and thermal stability.," *AerospaceLab*, no. 3, pp. p–1, (2011).
- [244] J. M. Lonergan, W. G. Fahrenholtz, and G. E. Hilmas, "Zirconium diboride with high thermal conductivity," *J. Am. Ceram. Soc.*, vol. 97, no. 6, pp. 1689–1691, (2014).
- [245] R. G. Munro, "Material properties of titanium diboride," *Journal of Research of the National institute of standards and Technology*, vol. 105, no. 5, p. 709, (2000).
- [246] I. Akin, B. C. Ocak, F. Sahin, and G. Goller, "Effects of sic and sic-gnp additions on the mechanical properties and oxidation behavior of nbb<sub>2</sub>," *J. Asian Ceram. Soc.*, vol. 7, no. 2, pp. 170–182, (2019).
- [247] K. Sairam, J. Sonber, T. C. Murthy, C. Subramanian, R. Fotedar, and R. Hubli, "Reaction spark plasma sintering of niobium diboride," *International Journal of Refractory Metals and Hard Materials*, vol. 43, pp. 259–262, (2014).
- [248] G. J. Harrington and G. E. Hilmas, "Thermal conductivity of zrb<sub>2</sub> and hfb<sub>2</sub>," *Ultra-High Temperature Ceramics: Materials for Extreme Environment Applications*, pp. 197–235, (2014).
- [249] H. Xiang, J. Wang, and Y. Zhou, "Theoretical predictions on intrinsic lattice thermal conductivity of zrb<sub>2</sub>," *J. Eur. Ceram. Soc.*, vol. 39, no. 10, pp. 2982–2988, (2019).
- [250] J. W. Zimmermann, G. E. Hilmas, W. G. Fahrenholtz, R. B. Dinwiddie, W. D. Porter, and H. Wang, "Thermophysical properties of zrb<sub>2</sub> and zrb<sub>2</sub>-sic ceramics.," *J. Am. Ceram. Soc.*, vol. 91, no. 5, pp. 1405–1411, (2008).
- [251] A. D. Stanfield, G. E. Hilmas, and W. G. Fahrenholtz, "Effects of ti, y, and hf additions on the thermal properties of zrb<sub>2</sub>," *Journal of the European Ceramic Society*, vol. 40, no. 12, pp. 3824–3828, 2020.
- [252] J. M. Lonergan, D. L. McClane, W. G. Fahrenholtz, and G. E. Hilmas, "Thermal properties of hf-doped zrb<sub>2</sub> ceramics," *J. Am. Ceram. Soc.*, vol. 98, no. 9, pp. 2689–2691, (2015).

- [253] C. M. Rost, T. Borman, M. D. Hossain, M. Lim, K. F. Quiambao-Tomko, J. A. Tomko, D. W. Brenner, J.-P. Maria, and P. E. Hopkins, “Electron and phonon thermal conductivity in high entropy carbides with variable carbon content,” *Acta Mater.*, vol. 196, pp. 231–239, (2020).
- [254] E. W. Neuman, M. Thompson, W. G. Fahrenholtz, and G. E. Hilmas, “Thermal properties of zrb2-tib2 solid solutions,” *Journal of the European Ceramic Society*, vol. 41, no. 15, pp. 7434–7441, (2021).
- [255] L. Zhang, D. A. Pejaković, J. Marschall, and M. Gasch, “Thermal and electrical transport properties of spark plasma-sintered hfb2 and zrb2 ceramics,” *Journal of the American Ceramic Society*, vol. 94, no. 8, pp. 2562–2570, 2011.
- [256] T. A. Osswald and G. Menges, *Materials science of polymers for engineers*. Carl Hanser Verlag GmbH Co KG, 2012.
- [257] H.-T. Liu, J. Zou, D.-W. Ni, W.-W. Wu, Y.-M. Kan, and G.-J. Zhang, “Textured and platelet-reinforced zrb2-based ultra-high-temperature ceramics,” *Scripta Materialia*, vol. 65, no. 1, pp. 37–40, 2011.
- [258] Y. Zhang, S.-K. Sun, W.-M. Guo, W. Zhang, L. Xu, J.-H. Yuan, D.-K. Guan, D.-W. Wang, Y. You, and H.-T. Lin, “Fabrication of textured (hf0. 2zr0. 2ta0. 2cr0. 2ti0. 2) b2 high-entropy ceramics,” *Journal of the European Ceramic Society*, vol. 41, no. 1, pp. 1015–1019, 2021.
- [259] H. Kinoshita, S. Otani, S. Kamiyama, H. Amano, I. Akasaki, J. Suda, and H. Matsumami, “Zirconium diboride (0001) as an electrically conductive lattice-matched substrate for gallium nitride,” *Japanese Journal of Applied Physics*, vol. 40, no. 12A, p. L1280, 2001.
- [260] T. Gupta, D. Ghoshal, A. Yoshimura, S. Basu, P. K. Chow, A. S. Lakhnot, J. Pandey, J. M. Warrender, H. Efstathiadis, A. Soni, *et al.*, “An environmentally stable and lead-free chalcogenide perovskite,” *Advanced Functional Materials*, vol. 30, no. 23, p. 2001387, 2020.
- [261] H. Zitouni, N. Tahiri, O. El Bounagui, and H. Ez-Zahraouy, “Electronic, optical and transport properties of perovskite bazrs3 compound doped with se for photovoltaic applications,” *Chemical Physics*, vol. 538, p. 110923, 2020.
- [262] K. Ye, N. Z. Koocher, S. Filippone, S. Niu, B. Zhao, M. Yeung, S. Bone, A. J. Robinson, P. Vora, A. Schleife, *et al.*, “Low-energy electronic structure of perovskite and ruddlesden-popper semiconductors in the ba-zr-s system probed by bond-selective polarized x-ray absorption spectroscopy, infrared reflectivity, and raman scattering,” *Physical Review B*, vol. 105, no. 19, p. 195203, 2022.
- [263] S. Niu, B. Zhao, K. Ye, E. Bianco, J. Zhou, M. E. McConney, C. Settens, R. Haiges, R. Jaramillo, and J. Ravichandran, “Crystal growth and structural analysis of perovskite chalcogenide bazrs3 and ruddlesden–popper phase ba3zr2s7,” *Journal of Materials Research*, vol. 34, no. 22, pp. 3819–3826, 2019.

- [264] W.-L. Ong, E. S. O'Brien, P. S. Dougherty, D. W. Paley, C. Fred Higgs III, A. J. McGaughey, J. A. Malen, and X. Roy, "Orientational order controls crystalline and amorphous thermal transport in superatomic crystals," *Nature materials*, vol. 16, no. 1, pp. 83–88, 2017.
- [265] M. Grimsditch, E. Zouboulis, and A. Polian, "Elastic constants of boron nitride," *Journal of applied physics*, vol. 76, no. 2, pp. 832–834, 1994.
- [266] G. Lehmann, P. Hess, S. Weissmantel, G. Reisse, P. Scheible, and A. Lunk, "Young's modulus and density of nanocrystalline cubic boron nitride films determined by dispersion of surface acoustic waves," *Applied Physics A*, vol. 74, pp. 41–45, 2002.
- [267] I. Yonenaga, T. Shima, and M. H. Sluiter, "Nano-indentation hardness and elastic moduli of bulk single-crystal aln," *Japanese journal of applied physics*, vol. 41, no. 7R, p. 4620, 2002.
- [268] R. Nowak, M. Pessa, M. Sukanuma, M. Leszczynski, I. Grzegory, S. Porowski, and F. Yoshida, "Elastic and plastic properties of gan determined by nano-indentation of bulk crystal," *Applied physics letters*, vol. 75, no. 14, pp. 2070–2072, 1999.
- [269] W. Mason, "Properties of transducer materials," *American Institute of Physics Handbook*, pp. 3–118, 1972.
- [270] W. Mason, "Acoustic properties of solids," *American Institute of physics handbook*, pp. 3–98, 1972.
- [271] D. E. Gray, "American institute of physics (aip). handbook," *New York: McGraw-Hill*, 1972.
- [272] S. Berri, D. Maouche, and Y. Medkour, "Ab initio study of the structural, electronic and elastic properties of agsbte<sub>2</sub>, agsbse<sub>2</sub>, pr<sub>3</sub>alc, ce<sub>3</sub>alc, ce<sub>3</sub>aln, la<sub>3</sub>alc and la<sub>3</sub>aln compounds," *Physica B: Condensed Matter*, vol. 407, no. 17, pp. 3320–3327, 2012.
- [273] A. Miller, G. Saunders, and Y. Yogurtcu *J. Phys. C: Solid State Phys.*, vol. 14, no. 11, p. 1569, (1981).
- [274] D. Morelli, V. Jovovic, and J. Heremans, "Intrinsically minimal thermal conductivity in cubic i- v- vi<sub>2</sub> semiconductors," *Physical review letters*, vol. 101, no. 3, p. 035901, 2008.
- [275] D. Gerlich, "Elastic constants of single-crystal indium arsenide," *Journal of Applied Physics*, vol. 34, no. 9, pp. 2915–2915, 1963.
- [276] P. Maycock, "Thermal conductivity of silicon, germanium, iii–v compounds and iii–v alloys," *Solid-state electronics*, vol. 10, no. 3, pp. 161–168, 1967.
- [277] Y.-L. Pei and Y. Liu, "Electrical and thermal transport properties of pb-based chalcogenides: Pbte, pbse, and pbs," *Journal of Alloys and Compounds*, vol. 514, pp. 40–44, 2012.

- [278] Y. Xiao, C. Chang, Y. Pei, D. Wu, K. Peng, X. Zhou, S. Gong, J. He, Y. Zhang, Z. Zeng, *et al.*, “Origin of low thermal conductivity in s<sub>n</sub>se,” *Physical Review B*, vol. 94, no. 12, p. 125203, 2016.
- [279] G. A. Elbaz, W.-L. Ong, E. A. Doud, P. Kim, D. W. Paley, X. Roy, and J. A. Malen, “Phonon speed, not scattering, differentiates thermal transport in lead halide perovskites,” *Nano letters*, vol. 17, no. 9, pp. 5734–5739, 2017.
- [280] D.-H. Chung, “Elastic moduli of single crystal and polycrystalline mgo,” *Philosophical Magazine*, vol. 8, no. 89, pp. 833–841, 1963.
- [281] R. Bell and G. Rupprecht, “Elastic constants of strontium titanate,” *Physical Review*, vol. 129, no. 1, p. 90, 1963.
- [282] C. Yu, M. L. Scullin, M. Huijben, R. Ramesh, and A. Majumdar, “Thermal conductivity reduction in oxygen-deficient strontium titanates,” *Applied physics letters*, vol. 92, no. 19, p. 191911, 2008.
- [283] D.-W. Oh, J. Ravichandran, C.-W. Liang, W. Siemons, B. Jalan, C. M. Brooks, M. Huijben, D. G. Schlom, S. Stemmer, L. W. Martin, *et al.*, “Thermal conductivity as a metric for the crystalline quality of strtio 3 epitaxial layers,” *Applied physics letters*, vol. 98, no. 22, p. 221904, 2011.
- [284] R. Vassen, X. Cao, F. Tietz, D. Basu, and D. Stöver, “Zirconates as new materials for thermal barrier coatings,” *Journal of the American Ceramic Society*, vol. 83, no. 8, pp. 2023–2028, 2000.
- [285] F. Lewis and N. Saunders *J. Phys. C: Solid State Phys.*, vol. 6, no. 15, p. 2525, (1973).
- [286] W. Jifang, E. Fisher, and M. Manghnzmi, “Elastic constants of nickel oxide,” *Chinese Physics Letters*, vol. 8, no. 3, p. 153, 1991.
- [287] J. Yang, X. Qian, W. Pan, R. Yang, Z. Li, Y. Han, M. Zhao, M. Huang, and C. Wan, “Diffused lattice vibration and ultralow thermal conductivity in the binary In–nb–o oxide system,” *Advanced materials*, vol. 31, no. 24, p. 1808222, 2019.
- [288] E. A. Scott, K. Hattar, J. L. Braun, C. M. Rost, J. T. Gaskins, T. Bai, Y. Wang, C. Ganski, M. Goorsky, and P. E. Hopkins, “Orders of magnitude reduction in the thermal conductivity of polycrystalline diamond through carbon, nitrogen, and oxygen ion implantation,” *Carbon*, vol. 157, pp. 97–105, 2020.
- [289] E. A. Scott, K. Hattar, E. J. Lang, K. Aryana, J. T. Gaskins, and P. E. Hopkins, “Reductions in the thermal conductivity of irradiated silicon governed by displacement damage,” *Physical Review B*, vol. 104, no. 13, p. 134306, 2021.

# Appendix A

## Published Work

During the course of my PhD, I have made several contributions to the scientific community by publishing peer-reviewed journal articles. Thus far, these include four first author publications, three co-first author publications, and fourteen co-author publications. The journal articles I have published as part of my PhD research are as follows:

### First author publications:

1. Md Shafkat Bin Hoque, Milena Milich, Md Sabbir Akhanda, Sashank Shivakumar, Eric R. Hoglund, Dragos Staicu, Mingde Qin, Kathleen F. Quiambao-Tomko, John A. Tomko, Jeffrey L. Braun, Joshua Gild, David H. Olson, Kiumars Aryana, Yee Rui Koh, Roisul Galib, Luka Vlahovic, Davide Robba, John T. Gaskins, Mona Zebarjadi, Jian Luo, and Patrick E. Hopkins. [Thermal and ablation properties of a high-entropy metal diboride:  \$\(\text{Hf}\_{0.2}\text{Zr}\_{0.2}\text{Ti}\_{0.2}\text{Ta}\_{0.2}\text{Nb}\_{0.2}\)\text{B}\_2\$](#) . *Journal of the European Ceramic Society* **43**, 4581-4587, (2023).
2. Md Shafkat Bin Hoque, Ian Brummel, Eric R. Hoglund, Connor J. Dionne, Kiumars Aryana, John A. Tomko, John T. Gaskins, Daniel Hirt, Sean W. Smith, Thomas Beechem, James M. Howe, Ashutosh Giri, Jon F. Ihlefeld, and Patrick E. Hopkins. [Interface independent sound speed and thermal conductivity of atomic layer deposition-grown amorphous  \$\text{AlN}/\text{Al}\_2\text{O}\_3\$  multilayers with varying oxygen composition](#). *Physical Review Materials* **7**, 025401, (2023).
3. Md Shafkat Bin Hoque, Yee Rui Koh, Jeffrey L. Braun, Abdullah Mamun, Zeyu Liu, Kenny Huynh, Michael E. Liao, Kamal Hussain, Zhe Cheng, Eric R. Hoglund, David H. Olson, John A. Tomko, Kiumars Aryana, Roisul Galib, John T. Gaskins, Mirza Mohammad Mahbube Elahi, Zayd C. Leseman, James M. Howe, Tengfei Luo, Samuel Graham, Mark S. Goorsky, Asif Khan, and Patrick E. Hopkins. [High in-plane thermal conductivity of aluminum nitride thin films](#). *ACS Nano* **15**, 9588–9599, (2021).
4. Md Shafkat Bin Hoque, Yee Rui Koh, Kiumars Aryana, Eric R. Hoglund, Jeffrey L. Braun, David H. Olson, John T. Gaskins, Habib Ahmad, Mirza Mohammad Mahbube Elahi, Jennifer K. Hite, Zayd C. Leseman, W. Alan Doolittle, and Patrick E. Hopkins. [Thermal conductivity measurements of sub-surface buried substrates by steady-state thermorefectance](#). *Review of Scientific Instruments* **92**, 064906, (2021).

### Co-first author publications:

1. Boyang Zhao,\* Md Shafkat Bin Hoque,\* Gwan Yeong Jung, Hongyan Mei, Shantanu Singh, Guodong Ren, Milena Milich, Qinai Zhao, Nan Wang, Huandong Chen, Shanyuan Niu, Sang-Jun Lee, Cheng-Tai Kuo, Jun-Sik Lee, John A. Tomko, Han Wang, Mikhail A. Kats, Rohan Mishra, Patrick E. Hopkins, and Jayakanth Ravichandran. [Orientation-controlled anisotropy in single crystals of quasi-1D  \$\text{BaTiS}\_3\$](#) . *Chemistry of Materials* **34**, 5680–5689, (2022). \*Joint First Authors.

2. Giacomo Lorenzin,\* Md Shafkat Bin Hoque,\* Daniel Ariosa, Lars P.H. Jeurgens, Eric R. Hoglund, John A. Tomko, Patrick E. Hopkins, and Claudia Cancellieri. [Tensile and compressive stresses in Cu/W multilayers: correlation with microstructure, thermal stability, and thermal conductivity](#). *Acta Materialia* **240**, 118315, (2022). \*Joint First Authors.
3. Yee Rui Koh,\* Md Shafkat Bin Hoque,\* Habib Ahmad,\* David H. Olson, Zeyu Liu, Jingjing Shi, Yekan Wang, Kenny Huynh, Eric R. Hoglund, Kiumars Aryana, James M. Howe, Mark S. Goorsky, Samuel Graham, Tengfei Luo, Jennifer K. Hite, W. Alan Doolittle, and Patrick E. Hopkins. [High thermal conductivity and thermal boundary conductance of homoepitaxially grown gallium nitride \(GaN\) thin films](#). *Physical Review Materials* **5**, 104604, (2021). \*Joint First Authors.

#### Co-author publications:

1. Eric R. Hoglund, De-Liang Bao, Andrew O'Hara, Thomas W. Pfeifer, Md Shafkat Bin Hoque, Sara Makarem, James M. Howe, Sokrates T. Pantelides, Patrick E. Hopkins, and Jordan A. Hachtel. [Direct visualization of localized vibrations at complex grain boundaries](#). *Advanced Materials* **35**, 2208920, (2023).
2. Pravin Karna, Md Shafkat Bin Hoque, Sandip Thakur, Patrick E. Hopkins, and Ashutosh Giri. [Direct measurement of ballistic and diffusive electron transport in gold](#). *Nano Letters* **23**, 491–496, (2023).
3. Christina M. Rost, Daniel L. Schmuckler, Clifton Bumgardner, Md Shafkat Bin Hoque, David R. Diercks, John T. Gaskins, Jon-Paul Maria, Geoffrey L. Brennecka, Xiadong Li, and Patrick E. Hopkins. [On the thermal and mechanical properties of  \$Mg\_{0.2}Co\_{0.2}Ni\_{0.2}Cu\_{0.2}Zn\_{0.2}O\$  across the high-entropy to entropy-stabilized transition](#). *APL Materials* **10**, 121108, (2023).
4. Md. Rafiqul Islam, M. A. Zubair, Roisul H. Galib, Md Shafkat Bin Hoque, John A. Tomko, Kiumars Aryana, Animesh K. Basak, and Patrick E. Hopkins. [Vacancy induced temperature-dependent thermal and magnetic properties of holmium substituted bismuth ferrite nanoparticle compacts](#). *ACS Applied Materials & Interfaces* **14**, 25886–25897, (2022).
5. Kiumars Aryana, John A. Tomko, Ran Gao, Eric R. Hoglund, Takanori Mimura, Sara Makarem, Alejandro Salanova, Md Shafkat Bin Hoque, Thomas W. Pfeifer, David H. Olson, Jeffrey L. Braun, Joyeeta Nag, John C. Read, James M. Howe, Elizabeth J. Opila, Lane W. Martin, Jon F. Ihlefeld, and Patrick E. Hopkins. [Observation of solid-state bidirectional thermal conductivity switching in antiferroelectric lead zirconate \( \$PbZrO\_3\$ \)](#). *Nature Communications* **13**, 1573, (2022).
6. Md Golam Rasul, Alper Kiziltas, Md Shafkat Bin Hoque, Arnob Banik, Patrick E. Hopkins, Kwek-Tze Tan, Babak Arfaei, and Reza Shahbazian-Yassar. [Improvement of the thermal conductivity and tribological properties of polyethylene by incorporating functionalized boron nitride nanosheets](#). *Tribology International* **165**, 107277, (2022).
7. Kiumars Aryana, Yifei Zhang, John A. Tomko, Md Shafkat Bin Hoque, Eric R. Hoglund, David H. Olson, Joyeeta Nag, John C. Read, Carlos Ríos, Juejun Hu, and Patrick E. Hopkins. [Suppressed electronic contribution in thermal conductivity of  \$Ge\_2Sb\_2Se\_4Te\$](#) . *Nature Communications* **12**, 7187, (2021).
8. Fabian Krahl, Ashutosh Giri, Md Shafkat Bin Hoque, Linda Sederholm, Patrick E. Hopkins, and Maarit Karppinen. [Experimental control and statistical analysis of thermal conductivity in ZnO–benzene multilayer thin films](#). *The Journal of Physical Chemistry C* **124**, 24731–24739, (2020).
9. Zhidong Ding, Mackenzie Ridley, Jeroen Deijkers, Naiming Liu, Md Shafkat Bin Hoque, John Gaskins, Mona Zebarjadi, Patrick E. Hopkins, Haydn Wadley, Elizabeth Opila, and Keivan Esfarjani. [The thermal and mechanical properties of hafnium orthosilicate: experiments and first-principles calculations](#). *Materialia* **12**, 100793, (2020).

10. Yee Rui Koh, Zhe Cheng, Abdullah Mamun, Md Shafkat Bin Hoque, Zeyu Liu, Tingyu Bai, Kamal Hussain, Michael E. Liao, Ruiyang Li, John T. Gaskins, Ashutosh Giri, John Tomko, Jeffrey L. Braun, Mikhail Gaevski, Eungkyu Lee, Luke Yates, Mark S. Goorsky, Tengfei Luo, Asif Khan, Samuel Graham, and Patrick E. Hopkins. [Bulk-like intrinsic phonon thermal conductivity of micrometer-thick AlN films](#). *ACS Applied Materials & Interfaces* **12**, 29443-29450, (2020).
11. Mingde Qin, Joshua Gild, Chongze Hu, Haoren Wang, Md Shafkat Bin Hoque, Jeffrey L. Braun, Tyler J. Harrington, Patrick E. Hopkins, Kenneth S. Vecchio, and Jian Luo. [Dual-phase high-entropy ultra-high temperature ceramics](#). *Journal of the European Ceramic Society* **40**, 5037-5050, (2020).
12. Eunhwa Jang, Priyanshu Banerjee, Jiyuan Huang, Rudolph Holley, John T. Gaskins, Md Shafkat Bin Hoque, Patrick E. Hopkins, and Deepa Madan. [Thermoelectric performance enhancement of naturally occurring Bi and chitosan composite films using energy efficient method](#). *Electronics* **9**, 532, (2020).
13. Joshua Gild, Andrew Wright, Kathleen Quiambao-Tomko, Mingde Qin, John A. Tomko, Md Shafkat Bin Hoque, Jeffrey L. Braun, Blake Bloomfield, Daniel Martinez, Tyler Harrington, Kenneth Vecchio, Patrick E. Hopkins, and Jian Luo. [Thermal conductivity and hardness of three single-phase high-entropy metal diborides fabricated by borocarbothermal reduction and spark plasma sintering](#). *Ceramics International* **46**, 6906-6913, (2020).
14. Kevin Ye, Sin Cheng Siah, Peter T. Erslev, Austin Akey, Charles Settens, Md Shafkat Bin Hoque, Jeffrey Braun, Patrick Hopkins, Glenn Teeter, Tonio Buonassisi, and R. Jaramillo. [Tuning electrical, optical, and thermal properties through cation disorder in Cu<sub>2</sub>ZnSnS<sub>4</sub>](#). *Chemistry of Materials* **31**, 8402–8412, (2019).